Integrated Optical Time Lenses for Passive Optical Networks

For Generation Of On-Chip Optical Fourier Transforms

Gutt, Lars Emil

Publication date:
2023

Document Version
Publisher's PDF, also known as Version of record

DTU Electro
Department of Electrical and Photonics Engineering

Integrated Optical Time Lenses for Passive Optical Networks

For Generation Of On-Chip Optical Fourier Transforms

PhD Thesis

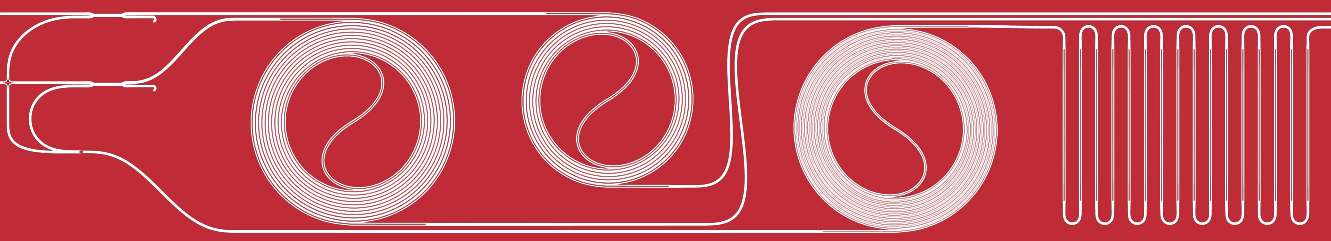

Abstract

Passive optical networks are a widely employed point to multi-point method of transmitting data to consumers in last mile networks. These networks are typically implemented with either time division or wavelength division multiplexed signal, but either implementation is inherently energy inefficient, with the inefficiency lying respectively on the receiver or transmission end. Using optical time lenses based on nonlinear optical processes, optical Fourier transforms can be carried out, which allows for the creation of a new type of passive optical network where time division multiplexed signals are transformed into wavelength division multiplexed signals using all optical signal processing. This type of network has been successfully demonstrated in fiber based systems. Due to the size of these and the low nonlinear efficiency and instability resulting from thermal effects of optical fiber, it remains in the experimental stage and has not yet been integrated in optical networks. Photonic integrated circuits offer an alternative road to successful implementation, since these are both compact and can be very efficient platforms for nonlinear optics. The subject of this PhD thesis is to investigate how a time lens based generator of an optical Fourier transform can be photonically integrated. Several important parts of this goal are achieved, including the design of photonic integrated circuits for optical Fourier transforms, demonstration of a four-wave mixing circuit with 50 dB extinction of the pump on-chip, the design of spiral Bragg gratings with a continuously varying radius of curvature, and the demonstration of circuits that allow access to light reflected from Bragg gratings with losses as low as 1 dB. These are important steps on the way and the lessons learned in this project lay the foundations for investigating heterogeneous integration in order to realize a system for fully integrated optical Fourier transforms.

Acknowledgements

Pengyu Guan, Associate Professor, DTU
For his role as principal supervisor.

Peter David Girouard, Dr., DTU
For his role as co-supervisor.

Arnan Mitchell, Professor, RMIT
For hosting me at InPAC at RMIT during my exchange.

Bill Corcoran, Dr., Monash University
For helping set up my exchange.

Contents

1 Introduction

As an ever increasing number of consumers all over the world get connected to the internet and as higher connection speeds are expected by these consumers ever larger demands are put on the physical infrastructure making up the internet, while at the same time making the energy costs of the internet skyrocket. In its annual internet report Cisco estimates that the number of internet users will reach 5.3 billion in 2023[1] and in its visual networking index it shows the monthly internet traffic is expected to be 396 Exabytes per month in 2022[2]. In these reports, they also track how these figures have changed over recent years, which is shown in figs. 1.1a and 1.1b. As clear from these figures, the increase in internet traffic outpaces the increase in users by a wide margin. From 2018 to 2022 the increase in users was 28% while the increase in traffic was 154%. This increase in traffic is driving a research effort into maximizing the amount of data that can be transferred around the world and in this research center. This includes a wide array of approaches applied to existing infrastructure like probabilistic constellation shaping[3] and applications in not yet existing platforms like using photonic micro-combs in conjunction with space multiplexing to send record breaking amounts of data over multi-core fibers[4]. Conversely the increase in traffic is also driving a large increase in the energy consumption of the Internet and Communications Technology (ICT) ecosystem (here it must be made clear that ICT refers to the networks themselves, the data centers, consumer devices and the production of the previous three). According to a forecast made in 2015, by Anders S. G. Andrae and Tomas Edler[5], ICT could account for 51% and 21% of global energy production in 2030 in a worst case and expected case scenario respectively. In the worst case scenario this could result in ICT contributing up to 23% of global greenhouse gas emissions in 2030. With the ongoing climate crisis starting to make its effects felt around the world and a reduction in internet traffic seeming highly unlikely, new approaches on to building a more sustainable internet are needed.

This thesis concerns one such approach, namely by modifying existing Passive Optical Networks (PON) and implementing so called Time-Lens Passive Optical Network (Lens-PONs) using Photonic In-

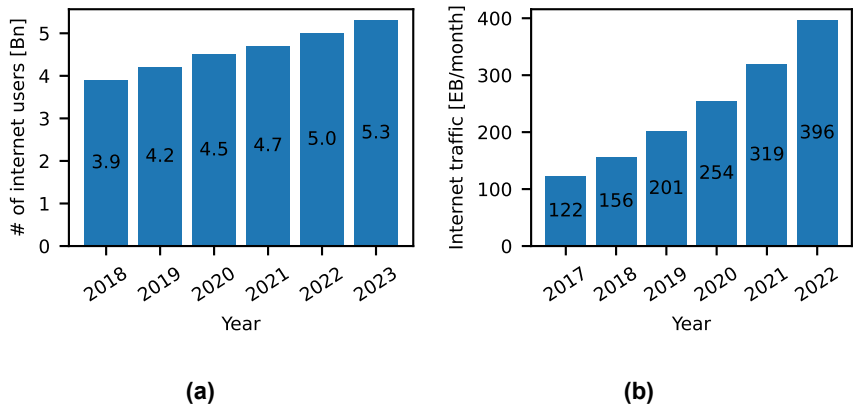

Figure 1.1: **(a)** The number of internet users per year from 2018-2023. **(b)** The amount of internet traffic in the years from 2017-2022.

tegrated Circuits (PIC). PONs are the backbone of short distance fiber data transmission where internet service providers send data on the last leg of travel, so improving the energy efficiency of these networks is a tantalizing milestone in reducing the energy usage of the internet. In this chapter, I will introduce how PONs work, what a time-lens is and how they can be utilized to improve the efficiency of PONs. Following this I will go over existing implementations of lens-PONs in bulk optical fiber and finally give an overview of my work in implementing a lens-PON on a PIC including the advantages and challenges of doing this in a photonic system.

1.1 Passive Optical Networks

PONs are often the last leg of data transmission where data is sent from a transceiver at a Central Office (CO) to many individual consumers with each their own Optical Network Unit (ONU). In this case, a consumer can both be a single home with direct fiber access and the only copper cables being inside the home itself or it could be a receiver that provides internet access for many nearby consumers using copper cables. A common implementation of a PON is using Time Division Multiplexing (TDM). With a TDM signal, the data for many consumers is coded in a single signal, with each consumer having an assigned time slot. After transmitting to each consumer, the signal repeats and sends the next bit to each consumer, usually with a short break in-between to show where one signal ends and the next one

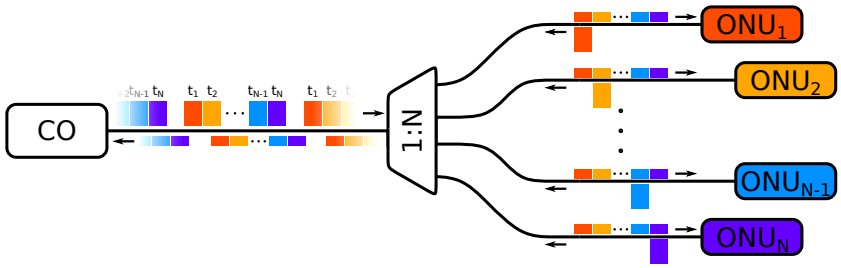

Figure 1.2: Structure of a TDM-PON. Data is transmitted downstream from the CO in repeating batches, with each ONU having an assigned assigned time slot in the batch as indicated by color. In the upstream direction, the ONUs can transmit data in their assigned time-slot. The size of the signal in a specific time slot is indicated by the size of the respective bar. As is illustrated, the splitting and combining of the signal in the up and downstream directions result in an attenuating of the signal.

begins. In the TDM-PON configuration, which is illustrated in fig. 1.2, the CO transmits a signal downstream where each ONU is assigned a time slot. The signal is passively split in up to 64 copies[6] using an optical power splitter such that each ONU receives an identical copy of the full signal. In the upstream direction, the ONU transmits data in it's assigned time slot. In principle, each ONU then has access to the data sent to all other ONUs from the same CO, but only the time-slot relevant for the individual ONU is read. As a consequence of the power splitting, the output powers of the CO and ONU needs to be many times larger than if they were directly transmitting to each other on a single line. In the downstream direction, this can also be seen in the fact that the majority of the energy the ONU receives is of no interest to it. Another disadvantage is that in order to record the signal at the correct time-slot, each ONU needs to have a detector that can record data at a rate that is much faster than the actual rate of received data. A great advantage of the TDM-PON method is that the CO needs only a single laser and high speed modulator, making the CO cheap and easy to build.

A different PON implementation uses Wavelength Division Multiplexing (WDM). With WDM data for many consumers is once again coded in a repeating signal, but in this case the data for each consumer is encoded in a specific wavelength instead of in a time slot. All wavelengths are sent at the same time as a pulse where the spectrum is a comb-like structure and repeats. In the WDM-PON, which is sketched

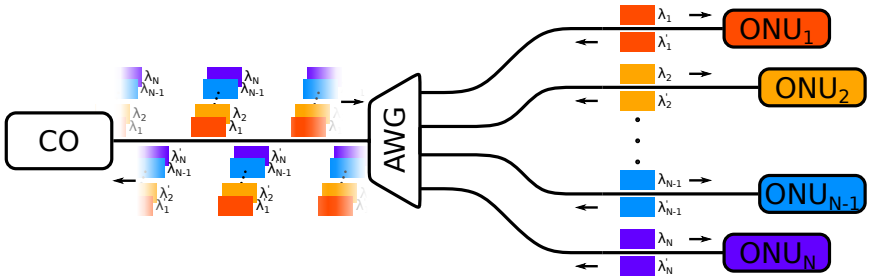

Figure 1.3: Structure of a WDM-PON. Data is transmitted downstream in repeating batches, with each ONU having an assigned receiving wavelength. The downstream signal is split losslessly using an AWG and the ONUs only receive the wavelength of interest. When ONUs transmit upstream they use an assigned wavelength, which is not necessarily the same as the input wavelength. If $\lambda_i \neq \lambda_i^{'}$, $\lambda_i^{'}$ will typically be one FSR of the AWG away from λ_i so the same AWG can be used for splitting and combining up and downstream signals.

in fig. 1.3, the CO transmits the WDM signal downstream. The signal is split into its wavelength components using an Arrayed Waveguide Grating (AWG) or equivalent wavelength selective device and the wavelength of interest, $\lambda_1 - \lambda_N$, is transmitted to ONU$_1$-ONU$_N$ respectively. The clear advantage of the WDM-PON is that each ONU only receives the part of the full signal that is of interest to that ONU, resulting in much less wasted power during transmission. The receivers also only need to be as fast as the symbol rate instead of many times faster as in the TDM case. The main disadvantage of WDM-PONs is on the upstream. Typically a laser for each WDM channels is required, with each of these lasers having high requirements on their wavelength stability and linewidth. The linewidth must be low in order to have a high spectral efficiency by keeping the WDM channels close in wavelength space and if they are closely packed, high stability is required. In short, many high quality lasers are needed to build the CO and as each laser will have an overhead during operation, the CO will be the expensive and power inefficient part of the system in this case.

As clear from the above, the standard PON implementation (TDM-PON) has a set of undesirable properties, namely low power efficiency and expensive ONU implementation, with both of these problems lying on the downstream end of the implementation. For the WDM-PON on the other hand, only the CO is expensive to imple-

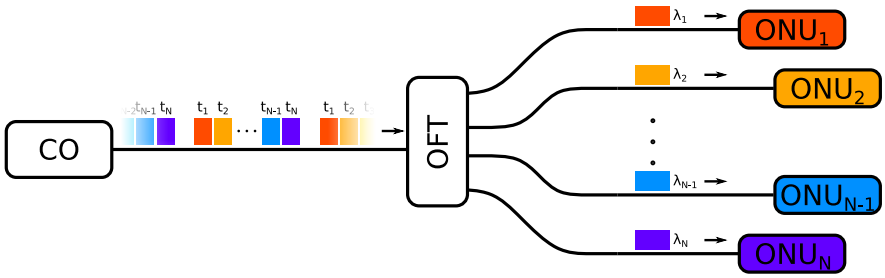

Figure 1.4: Proposed hybrid PON with an OFT taking place in the downstream direction. The version where no upstream OFT takes places so the downstream signal is initially a TDM signal and is converted into a WDM signal. On the return the signal stays an WDM signal, so an AWG is also assumed to be placed at the AWG.

ment and power hungry to run, while everything downstream of this is much more efficient than the TDM-PON. A good implementation would be something that takes the pros of each approach and discards the cons. A method that uses a TDM transceiver as the CO but converts this signal into a WDM signal before splitting and behaves as a WDM-PON downstream from the CO would be desirable. In essence what we are looking for is a device or technique that takes the waveform of a TDM signal and images this waveform onto the spectrum of the signal and vice versa. We will call this an Optical Fourier Transform (OFT) and it would allow for converting a TDM signal into a WDM signal. Using a device like this would allow us to transmit downstream using a TDM transmitter, convert this signal into a WDM signal and sidestep the issues with TDM-PONs — that is large splitting losses and fast detectors. The main issue for WDM-PON is the fact that the CO needs many lasers, but in this case no extra lasers are added as there will be one present at each ONU in any case. A hybrid PON like this is illustrated in fig. 1.4. The OFT is the center piece of this network so the final goal of this thesis will be the design of a PIC that will implement an OFT. This thesis will be divided into several parts. In this introductory part, we will explore the physics that makes the implementation of an OFT possible and explore the strengths and weaknesses of several different platforms for integrated photonics that can be used for implementation of an OFT. In chapter 2, we will explain how the different elements of a time-lens can be designed using different specialized integrated waveguides and delve into the physics of these different elements. In chapter 3,

we will further investigate how the performance of these elements can be improved by employing non-standard approaches and combining different components in novel ways. In chapter 4, we will explain the framework for simulating the different needed elements that has been created as part of this project, along with the framework used creating layouts for PICs we have created, which interacts with the simulation framework. In chapter 5, we will present and analyze the experimental results from the different photonic chips we have had fabricated. Finally, in chapter 6, we will take a look back at what has been achieved and learned over the course of this project and how both successes and failures can be used when moving forwards with this project.

Returning to the task at hand, we must first find a way to implement an OFT. They key turns out to be the so called space-time duality: the fact that, mathematically, dispersion in the time domain and diffraction in space are analogous, while at the same time quadratic phase shifts in time and space are also analogous. This set of facts makes it possible to map our knowledge of spatial optics to time domain phenomena and use this to solve problems such as the one in front of us.

1.2 Optical Fourier Transforms and Space-Time Duality

In order to see how the analog between diffraction and dispersion can be exploited, let us first take a look at how an OFT can be achieved in the spatial domain, with the underlying theory and notation briefly expanded upon in appendix A In space, a Fourier transform of an aperture can be imaged in a plane as illustrated in fig. 1.5. Here we see a monochromatic field with its wave crests illustrated as blue lines propagating to the right and meeting a rectangular aperture which is much smaller than the wavelength of the field [1]. After the aperture the light starts propagating as circular waves with their centers at the edges of the aperture. In the points where the wave crests overlap, this leads to constructive interference. Conversely, in the points between, destructive interference happens. The light is then focused by

[1] Note that the scales in this figure has been exaggerated. Both the relationship between the wavelength (the distance between the blue lines) and the aperture as well as the distance between the aperture and the lens would not lead to the exact phenomenon described here.

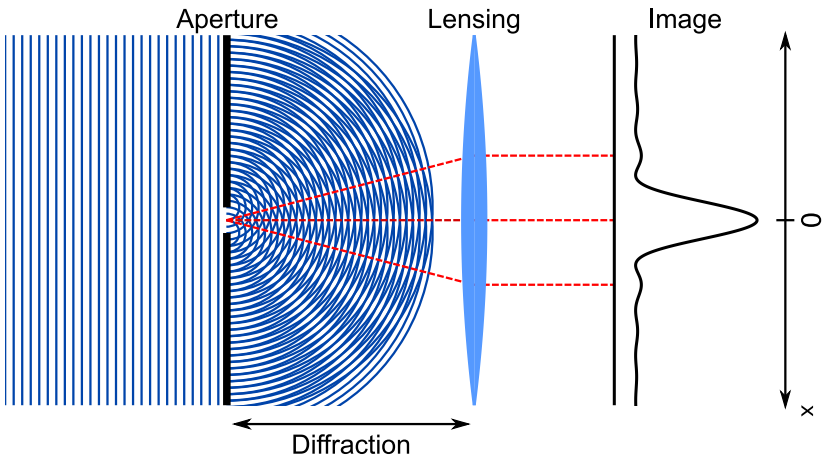

Figure 1.5: Optical Fourier transform in 2D space. A monochromatic field propagates through an aperture and undergoes diffraction. After propagating further, the field is collimated by a lens and imaged on a plane.

a lens by applying a parabolic phase shift to the wavefront, and projected onto a screen where the intensity distribution takes the form of a $\text{sinc}^2(x)$ pattern, which is the Fourier transform of a rectangle. What is happening is that the intensity of the field just as it is at the aperture is in the shape of a rectangle in the x-direction and its spatial frequencies correspond to those of the aperture. As it propagates further it is diffracted, which corresponds to the spatial frequencies or transverse wavenumbers of the field propagating at different angles. If the distance of propagation is much longer than the wavelength of the field (that is, we are applying the lens in the far field), the different transverse wavenumbers will be well separated in the x-direction and thus the intensity distribution will correspond to the Fourier transform of the aperture. Without the lens in the system we would still get a Fourier transform of the aperture after sufficiently long propagation, but as can be seen from the figure, there would still be a residual phase that depends on the distance away from $x = 0$. Only if the lens is in place and has exactly the correct strength in relation to the diffraction the field has undergone will we be able to cancel out this phase such that the phase relation between different points on the image plane is zero. Additionally, this makes it possible to go back and forth between the situation at the aperture and at the image plane by reversing the direction of propagation of the field.

What we see here is that it is possible to get the Fourier transform of a field distribution in space using diffraction and by applying a quadratic phase shift, which is much like what we want to do to a waveform in time. Luckily, the action of diffraction in space is analogous to dispersion in time and much like a quadratic phase shift is applied by a lens in space, the same can be applied to a waveform in time using a time-lens. This analogous behavior is termed the space-time duality and will be explored further in the following.

1.2.1 Space-Time Duality

In order explore the concept of space-time duality more rigorously than above, we first take a completely general electric field, $\mathbf{E}(\mathbf{r}, t)$, and apply a set of approximation relevant to the spatial and temporal cases of diffraction and dispersion respectively, following the procedure laid out by Brian H. Kolner[7]. In this case, we are interested in the behavior of an electric field propagating in vacuum. This means that no free charges are present and that the induced polarization is zero. From eq. (A.9), we have in that in this case:

$$\nabla \times \nabla \times \mathbf{E} = -\frac{1}{c^2}\frac{\partial^2 \mathbf{E}}{\partial t^2}, \tag{1.1}$$

and assume that the field is monochromatic such that the wave equation reduces to the time invariant Helmholtz equation,

$$\left(\nabla^2 + k^2\right)\mathbf{E} = 0, \tag{1.2}$$

where k is the wave number,

$$k = \frac{\omega}{c} = \frac{2\pi}{\lambda}, \tag{1.3}$$

with ω being the angular frequency and λ the wavelength of the field. In this case we want to investigate ray-like fields propagating along the z-axis, meaning that the fastest phase variation will occur along this axis, so we write the field as

$$\mathbf{E}(\mathbf{r}) = E(\mathbf{r})e^{-ikz}. \tag{1.4}$$

Here $E(\mathbf{r})$ is a slowly varying envelope that varies slowly in relation to k. We can now apply the paraxial approximation, which assumes that the curvature envelope varies much less along the axis of propagation than along the transverse profiles. In the case of ray-like fields this

makes sense as we imagine the field to be mostly localized at the axis of propagation. This approximation can be written as:

$$\left|\frac{\partial^2 E}{\partial z^2}\right| \ll \left\{\left|\frac{\partial^2 E}{\partial x^2}\right|, \left|\frac{\partial^2 E}{\partial y^2}\right|, \left|2k\frac{\partial E}{\partial z}\right|\right\}. \tag{1.5}$$

If we insert eq. (1.4) into the Helmholtz equation and apply the paraxial approximation as stated in eq. (1.5), we arrive at the paraxial wave equation:

$$\boxed{\frac{\partial E}{\partial z} = -\frac{i}{2k}\nabla_t^2 E,} \tag{1.6}$$

which describes paraxial diffraction, where:

$$\nabla_t^2 = \left[\frac{\partial^2}{\partial x^2} + \frac{\partial^2}{\partial y^2}\right]. \tag{1.7}$$

The application of the diffraction operator $-i/2k\nabla_t^2$ results in a quadratic phase shift in the Fourier domain (k-space)[8]:

$$\phi_d(k_x) = -\frac{z}{2k}k_x^2, \tag{1.8}$$

where k_x is the transverse wavenumber. This expression describes the degree to which different transverse wavenumbers are spread in the x-direction. The action of diffraction can be expressed by the impulse response[9]:

$$h_d(x) = h_{d,0}\exp\left(i\frac{k}{2d}x^2\right), \tag{1.9}$$

where $h_{d,0}$ is a constant that depends on the propagation distance. The conclusion in the end, is that diffraction corresponds to different transverse wavenumbers or equivalently receiving a spatially varying quadratic phase, which under the paraxial approximation is described by eqs. (1.8) and (1.9). A lens with focal length f on the other hand imparts a spatially varying quadratic phase shift

$$\phi_l(x) = -\frac{k}{2f}x^2, \tag{1.10}$$

with the impulse response:

$$h_l(x) = h_{l,0}\exp\left(-i\frac{k}{2f}x^2\right). \tag{1.11}$$

Comparing eqs. (1.9) and (1.11) we see that if $d = f$, using a lens with the right focal length we can cancel out the spatially varying phase that is a result of dispersion, just as we expected from the discussion of fig. 1.5. We saw that the result of this is that the spectrum of the aperture appears in the image plane, but what is not clear is that the shape of the aperture will be imaged in the spectrum of transverse wavenumbers. Instead of continuing here, let us instead turn to the action of dispersion in time domain and continue with a more rigorous derivation in this domain later.

In order to describe narrow-band dispersion of a pulse we roughly follow the derivations by Govind Agrawal[10]. We start with the wave-equation eq. (A.9) in the presence of a (linear) medium with polarization $\mathbf{P}(\mathbf{r}, t)$: We again assume a slowly varying envelope, which in this case means that the envelope varies slowly over an optical cycle, and that the field is quasi monochromatic. Being quasi monochromatic in this case is taken to mean that the spectral width of the pulse $\Delta\omega$ in relation to the central frequency ω_0 satisfies $\Delta\omega/\omega_0 \ll 1$. Using the slowly varying envelope we can separate the slowly varying part of the electric field and polarization from the rapidly varying part:

$$\mathbf{E} = E(\mathbf{r}, t)e^{-i\omega_0 t} \tag{1.12}$$

$$\mathbf{P} = P(\mathbf{r}, t)e^{-i\omega_0 t} \tag{1.13}$$

$$= \chi^{(1)}(x, y, t)\epsilon_0\mathbf{E}, \tag{1.14}$$

where $\chi^{(1)}(x, y, t)$ is assumed only to vary in the transverse directions. If we insert eqs. (1.12) and (1.14) into eq. (A.9), and take the Fourier transform, defined as:

$$\tilde{f}(\mathbf{r}, \omega) = \int_{-\infty}^{\infty} f(\mathbf{r}, t)e^{i\omega t}dt \tag{1.15}$$

$$= F\{f(\mathbf{r}, t)\}, \tag{1.16}$$

we get,

$$\nabla \times \nabla \times \tilde{\mathbf{E}} = \tilde{\epsilon}(\omega)\frac{\omega_0^2}{c^2}\tilde{\mathbf{E}}, \tag{1.17}$$

since

$$F\left\{\frac{\partial f(t)}{\partial t}\right\} = i\omega\tilde{f}(\omega). \tag{1.18}$$

In eq. (1.17):

$$\tilde{\epsilon}(x,y,\omega) = \left[1 + \tilde{\chi}^{(1)}(x,y,\omega)\right], \tag{1.19}$$

is the dielectric permittivity of the medium. We once again assume that no free charges are present (typically a good approximation for the optical media we will be working with) and use eq. (A.8) with the result that eq. (1.17) now reduces to:

$$\left[\nabla^2 + \tilde{\epsilon}(x,y,\omega)\frac{\omega_0^2}{c^2}\right]\tilde{\mathbf{E}} = 0, \tag{1.20}$$

which is the Helmholtz equation for propagation in a linear medium.

Unlike like with paraxial diffraction where the field spreads in the transverse direction as it propagates, we are now interested in the behavior confined modes of a waveguide and the evolution of its temporal envelope. Due to this we assume that the behavior of the field can be separated into some transverse field distribution and a field envelope that are independent of each other, i.e. that the electric field takes solutions of the form

$$\tilde{E}(\mathbf{r},\omega-\omega_0) = F(x,y)\tilde{A}(z,\omega-\omega_0)e^{i\beta_0 z}, \tag{1.21}$$

with $F(x,y)$ being the transverse field distribution, $\tilde{A}(z,\omega-\omega_0)$ the envelope and β_0 the propagation constant of the mode to be determined by the solution. Here we are also implicitly assuming that the vectorial nature of the electric field is unimportant, by writing the field as a scalar. This tends to be a good assumption as the modes of waveguides typically can be separated into distinct polarizations to a good approximation. Inserting eq. (1.21) into eq. (1.20) leads to an equation for $F(x,y)$ and $\tilde{A}(z,\omega-\omega_0)$ each:

$$\frac{\partial^2 F}{\partial x^2} + \frac{\partial^2 F}{\partial y^2} + \left[\epsilon(x,y,\omega)k_0^2 - \beta^2\right]F = 0, \tag{1.22}$$

$$2i\beta_0\frac{\partial \tilde{A}}{\partial z} + \left[\beta^2 - \beta_0^2\right]\tilde{A} = 0. \tag{1.23}$$

The mode profile $F(x,y)$ and the propagation constant β is found by solving the eigenvalue equation eq. (1.22). Here β can be seen as

an expression of how the mode interacts with the medium $\tilde{\epsilon}(x, y, \omega)$. Using the solution to eq. (1.22) the evolution of the envelope during propagation can be found using eq. (1.23). The electric field $\mathbf{E}(\mathbf{r}, t)$ can be expressed as

$$\mathbf{E}(\mathbf{r}, t) = F(x, y)A(z, t)e^{i(\beta_0 z - \omega_0 t)}, \tag{1.24}$$

by approximating $\beta^2 - \beta_0^2$ as $2\beta_0(\beta - \beta_0)$ The Fourier transform of $A(z, t)$, $\tilde{A}(z, \omega - \omega_0)$, satisfies equation eq. (1.23), which can be written as

$$\frac{\partial \tilde{A}}{\partial z} = i\left[\beta(\omega) - \beta_0\right]\tilde{A}. \tag{1.25}$$

In order to go back to the time domain we can take the inverse Fourier transform of this. Here we expand $\beta(\omega)$ as a Taylor series around the carrier frequency ω_0:

$$\beta(\omega) = \beta_0 + (\omega - \omega_0)\beta_1 + \frac{1}{2}(\omega - \omega_0)^2\beta_2 + \dots. \tag{1.26}$$

with

$$\beta_0 \equiv \beta(\omega_0), \tag{1.27}$$

and

$$\beta_m \equiv \left(\frac{d^m\beta}{d\omega^m}\right), \quad m = 1, 2, \dots. \tag{1.28}$$

The propagation constant is typically expressed as this Taylor series, as an analytic expression for the response of the medium to the field typically is not known. Per definition β_0 describes the phase evolution of the carrier frequency and β_1 is related to the velocity of propagation of the mode. This propagation velocity is known as the group velocity and is expressed as

$$v_g = \frac{1}{\beta_1}, \tag{1.29}$$

while β_2 is related to the dispersion of the pulse. Using the definition of $\beta(\omega)$ in eq. (1.26), we can now write eq. (1.25) to second order as:

$$\frac{\partial \tilde{A}}{\partial z} = i\left[(\omega - \omega_0)\beta_1 + \frac{1}{2}(\beta - \beta_0)^2\beta_2\right]\tilde{A}. \tag{1.30}$$

By taking the inverse Fourier transform of this and using the inverse of the result in eq. (1.18) we get:

$$\left(\frac{\partial}{\partial z}+\beta_1\frac{\partial}{\partial t}\right)A(z,t)=\frac{i\beta_2}{2}\frac{\partial^2 A}{\partial t^2}. \tag{1.31}$$

Carrying out a change of variables to a co-propagating coordinate system where:

$$\tau=(t-t_0)-\frac{z-z_0}{v_g}, \tag{1.32}$$

and

$$\zeta=z-z_0, \tag{1.33}$$

eq. (1.31) takes the form:

$$\boxed{\frac{\partial A}{\partial \zeta}=\frac{i\beta_2}{2}\frac{\partial^2 A}{\partial \tau^2},} \tag{1.34}$$

which bears a striking similarity to eq. (1.6) which described paraxial diffraction, in that a first order derivative of the envelope with respect to the coordinate in the direction of propagation is related to a second order derivative of the envelope. Of course, in this case it is a second order derivative in time, but that plays well into what what we expect these equations to describe: namely that for paraxial diffraction, we expect a change in position along the propagation axis to leads to a spreading of the spatial frequencies in the transverse direction and that for dispersion we expect to see a spreading of frequencies in time as we move along the axis of propagation. In both cases we have an operator describing this spreading. For the case of diffraction, this operator is:

$$S_s=-\frac{i}{2k}\nabla_t^2. \tag{1.35}$$

The larger this is (or the smaller k is), the more the field will spread out during propagation, so a larger wavelength should lead to more spreading, which corresponds well with what is seen in reality. In the case of dispersion, we have:

$$S_t=-\frac{i\beta_2}{2}\frac{\partial^2}{\partial \tau^2}, \tag{1.36}$$

so larger β_2 tells us how much a pulse will broaden in time per unit length. As can be seen from the definition of β_2, it has units of s^2/m.[2] β_2 is typically referred to as the Group Velocity Dispersion (GVD) since it is the derivative of the inverse group velocity. Often, we will talk about the Group Delay Dispersion (GDD), D_2, instead. This is the total dispersion of a specific waveguide and is defined as:

$$D_2 = \frac{\partial^2 \phi}{\partial \omega^2}, \tag{1.37}$$

so a direct expression of the changes of phase experienced by a frequency. If a field propagates the distance z through a medium with GVD β_2 it experiences a GDD of

$$D_2 = \beta_2 z \tag{1.38}$$

It can be useful to refer to D_2 instead of β_2 in some cases, since even if it is the case that we are discussing the GVD of some waveguide, β and in turn β_2 is a result of the interaction of the field with the material properties of the medium and the shape of the waveguide. It can be illuminating to underline that the dispersion is due to other factors than just the material properties. The phase shift due to dispersion is:

$$\phi(\omega) = \frac{D_2}{2}\omega^2, \tag{1.39}$$

which just as in the spatial case is a quadratic phase shift, which in this case depends on the GDD. In the time domain be expressed with the impulse response:

$$h_d(\tau) = h_d \exp\left(-\frac{i}{2D_2}\tau^2\right), \tag{1.40}$$

where h_d is a constant that depends on D_2. Equivalently in the frequency domain it can be expressed as the transfer function[11]:

$$H_d(\omega) = \exp\left(i\frac{D_2}{2}\omega^2\right). \tag{1.41}$$

In the spatial case we saw in eq. (1.10) how the action of a lens was a quadratic phase shift as a function of the transverse coordinate. The

[2] For more detail on the mathematics of how these second order terms on the right hand sides correspond to broadening in time and space respectively, again see Kolner[7].

reason for this quadratic phase shift is not a fact of nature such as diffraction is, but due to us specifically constructing lenses in a way that they counteract the effects of this diffraction. For a field propagating through a waveguide in the time domain, the case is not exactly the same since we have more tools at hand for engineering the dispersion, but let us still be inspired by the spatial case and assume that we can design a device that results in an equivalent phase shift. This time-lens would need to impart a phase shift of:

$$\phi_l(\tau) = \frac{\omega_0}{2f_T}\tau^2 \tag{1.42}$$

$$= \frac{C}{2}\tau^2. \tag{1.43}$$

Here f_T is the "focal time" of the lens, or how much a pulse is compressed or expanded by the action of it. This can be related to C, the chirp of the time-lens. This phase shift can also be expressed as the transfer function:

$$H_l(\omega) = \sqrt{\frac{2\pi i}{C}}\exp\left(-\frac{i}{2C}\omega^2\right) \tag{1.44}$$

The action of the time-lens can be seen as a rearrangement of the different frequencies of a pulse. For a chirped pulse, different frequencies arrive at some point with a linear offset in time. If we imagine the pulse as an audio signal instead, we can see how this linear relationship between frequency and arrival time would lead to a distinct chip sound, which is likely the origin of the term. Of course, the design of a time-lens is more involved than that of a space lens but can be carried out and will be elaborated upon in section 1.2.3.

Summing up, we have seen that under appropriate approximations, the evolution of the spatial field envelope of a paraxial beam evolves in a way that closely resembles the evolution of the temporal field envelope of a quasi monochromatic pulse. The equations describing the evolution of these fields are equivalent and show that they experience a spreading of the envelope in space and time respectively. Due to the similarity of the equations, we can also infer that applying a quadratic phase shift to the field results in lensing in space and time. The analysis of the preceding chapter leads to the conclusion that spatial lens systems such as the one illustrated in fig. 1.5, which generates a Fourier transform of the initial field envelope in the image plane, can be replicated in the time domain by exploiting these

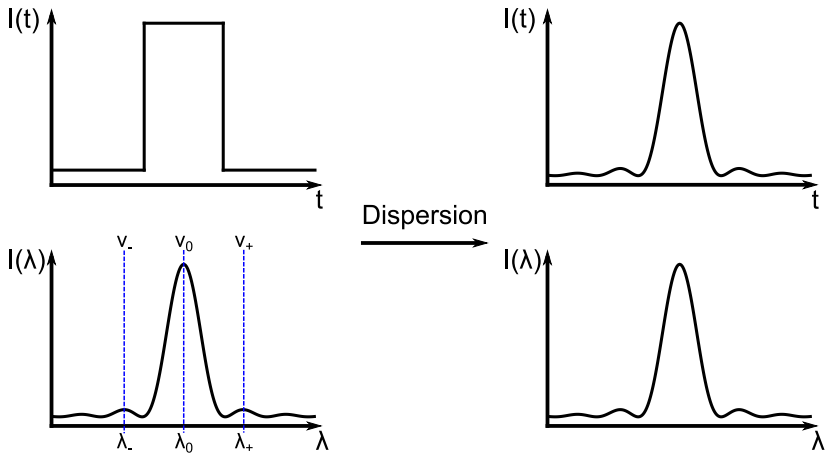

Figure 1.6: Illustration of a dispersive OFT of a square pulse. The spectrum is imaged onto the waveform due to the different propagation speeds of different spectral components as highlighted on the initial spectrum.

analogues. The following section will go into more detail about how a time-lens system like this would work.

1.2.2 Optical Fourier Transforms in the Time Domain

In order to obtain our goal of designing a system for achieving an optical Fourier transform in the time domain, let us use space-time duality and use systems from spatial optics as a basis for designing systems for the time domain . If we imagine a setup like the one shown in fig. 1.5 but without the lens present, we see that we still get the spectrum of the spatial envelope in the image plane as long as we are in the Fraunhofer or far-field regime, which is defined as[12]:

$$kd^2 \ll 2L. \tag{1.45}$$

Here k is the wave number as usual, d is the characteristic size of the aperture and L is the distance between the aperture and the image plane. Essentially this means that in order to get proper imaging, enough diffraction to properly separate each spatial frequency must have happened, as determined by the wavelength and size of the aperture. We can imagine an equivalent situation in the time domain. If we have an input pulse with a rectangular envelope we know that it will have a frequency distribution in the shape of a sinc^2 function centered on the carrier frequency, as illustrated in fig. 1.6. Through dispersion the individual frequencies will be separated in time, leading to the spectrum of the initial waveform getting imaged in the final

waveform, also illustrated in fig. 1.6. Like for the spatial case, the accumulated dispersion needs to be much larger than the time-scale of the pulse in order for each frequency to be properly resolved at the image time (as opposed to the image plane in the spatial case), a time domain equivalent of the Fraunhofer regime. This condition can be expressed as[8]:

$$\tau_w^2 \ll |D_2|, \tag{1.46}$$

where τ_w is the temporal width of the initial pulse and D_2 is the group delay dispersion of the waveguide. Of course, the method described here is in a sense the inverse of what we desired, but I find it a good place to start since the process of imaging the spectrum of a signal in the waveform through dispersion is quite intuitive. Ideally, we want a process that can be run in the reverse so we can get the desired result and this process is not reversible. This is due to the fact that the OFT that has been carried out in this example is incomplete, where a complete OFT would be one that not only images the spectrum in the waveform, but at the same time images the shape of the waveform in the spectrum. In that case, the OFT can always be carried out in reverse and we will always be able to switch back and forth from one representation of a signal to another. As might have been gathered from the preceding section it is by including a time-lens that we will be able to carry out a complete OFT and achieve our goal. We can get a sense for how this functions by looking at fig. 1.5 once more. Just before the lens in this figure the wavefront is curved with light on the symmetry axis at $x = 0$ arriving before light that is not on the symmetry axis, with the delay increasing the further away the light is from this axis. We can also see this as the phase of the wavefront relative to the center increasing symmetrically the further away from the symmetry axis we are. The action of the lens is then to cancel this phase offset at all points on the lens by delaying the light by just the right amount such that all the light arrives at the same time at the image plane or equivalently, with a constant phase across the image plane. Clearly, for any given diffraction, the lens must have a specific focal length in order to perfectly cancel out the differences in phase accumulated.

Turning now to the time domain equivalent where a waveform has been dispersed, we see that we have much the same situation: after dispersion the phase of individual frequency components will be offset relative to one another due to the different delay they all have

experienced, which is the chirp of the pulse. Due to the space-time duality let us assume that the application of a time-lens supplying the correct chirp will cancel the chirp due to dispersion by rearranging the frequency components in the right fashion and at the same time lead to a reversible OFT. From the above somewhat hand-waving analysis it is not immediately clear that this will lead to the desired modification of the spectrum, so let us get into the specifics of the problem to show that this is indeed the case by analyzing the propagation of a pulse with the initial field envelope $A_i(\tau)$, following the derivations by Palushani et al.[11].

Using the transfer function for propagation through a dispersive medium, eq. (1.41), the Fourier transform of the envelope after propagation is:

$$\tilde{A}_D(\omega) = \tilde{A}_i(\omega) H_d(\omega) \tag{1.47}$$

$$= \tilde{A}_i(\omega) \exp\left(i \frac{D_2}{2} \omega^2\right) \tag{1.48}$$

The time-lens is then applied, the action of which can be expressed as a convolution of $\tilde{A}(\omega)$, with the impulse response of the time-lens, eq. (1.44):

$$\tilde{A}_c(\omega) = \frac{1}{2\pi} \tilde{A}_D(\omega) * H_l(\omega) \tag{1.49}$$

$$= \frac{1}{2\pi} \int_{-\infty}^{\infty} \tilde{A}_D(\omega') H_l(\omega - \omega') d\omega' \tag{1.50}$$

$$= \sqrt{\frac{i}{2\pi C}} \int_{-\infty}^{\infty} \tilde{A}_i(\omega') \exp\left[i \frac{D_2}{2} \omega'^2\right] \cdot \exp\left[-i \frac{i(\omega - \omega')^2}{2C}\right] d\omega' \tag{1.51}$$

$$= b \int_{-\infty}^{\infty} \tilde{A}_i(\omega') \exp\left[i \frac{(D_2 C - 1)\omega'^2 + 2\omega\omega'}{2C}\right] d\omega' \tag{1.52}$$

where

$$b = \sqrt{\frac{i}{2\pi C}} \exp\left(-i \frac{\omega^2}{2C}\right). \tag{1.53}$$

In eq. (1.52) we see that if we choose our dispersion such that

$$C = 1/D_2 \tag{1.54}$$

we can rewrite it as:

$$\tilde{A}_c(\omega) = b \int_{-\infty}^{\infty} \tilde{A}_i(\omega') \exp\left(iD_2\omega\omega'\right) d\omega'. \tag{1.55}$$

Since we know that the time τ of the signal is related to the applied dispersion as $\tau = D_2\omega$, this can be further rewritten as

$$\tilde{A}_c(\omega) = b \int_{-\infty}^{\infty} \tilde{A}_i(\omega')|_{\tau=D_2\omega} \exp\left(i\tau\omega'\right) d\omega' \tag{1.56}$$

$$= 2\pi b A_i(\tau)|_{\tau=D_2\omega}, \tag{1.57}$$

Taking the absolute square of this we get:

$$|\tilde{A}_c(\omega)|^2 = 2\pi|D_2||A_i(\tau)|^2_{\tau=D_2\omega}, \tag{1.58}$$

with the result that the initial waveform gets imaged in the final spectrum exactly as desired. In eq. (1.52) we see that an imperfect match between the dispersion and the chirp (the strength of the time-lens) leaves a residual phase that gives us with an incomplete Fourier transform as expected from the preceding discussion. It also becomes clear from eq. (1.58) that the magnitude of the dispersion controls the scaling factor of the output spectrum. Larger dispersion will lead to a larger amount of power concentrated in a given frequency band while at the same time leading a to a more or less compressed output spectrum since $\omega = \tau/D_2$. If we imagine a TDM signal as the input a larger D_2 will lead to a narrower spacing between the resulting WDM tributaries. Intuitively, it makes sense that a large D_2 will lead to more power in a given frequency band since this also leads to a more compressed resulting spectrum.

1.2.3 Mechanisms for Dispersion Generation and Time-lensing

Now that we have show that it is possible to create an OFT using a time-lens, let us turn to an overview of how to implement time-lens systems and OFTs specifically. As we have seen, the required ingredients are dispersion and quadratic phase modulation in the time domain, which will be the case not just for OFTs but any time-lens system. Dispersion, specifically linear dispersion, can be obtained in many ways. In the paper by B. Kolner[7] he proposes using pairs of diffraction gratings that reflect light along different angles according to frequency makes it possible to make different frequencies propagate different lengths with dispersion created as a result of the frequency

dependent delay. The amount of dispersion that can be generated by this type of system will be limited by the physical size of the system the dispersion is determined by the difference in path lengths taken. Another approach is to use the natural dispersion resulting from propagation through an optical fiber or integrated waveguide. The dispersion per unit length of these will typically be quite small, so integrated waveguides are not well suited to this due to the high losses experienced in these. Optical fiber on the other hand has very low loss and many kilometers of fiber can be stored in a small volume. Unfortunately the dispersion of fiber is never exactly linear which leads to distortion of the output of a time-lens system as explored by X. Xu[13]. A good solution is the Bragg grating which is a 1D photonic crystal which reflects light at a wavelength determined by the period of the grating. By varying the period along the length of the grating, the desired dispersion can be engineered both in fiber and integrated photonics, with the design of these being an important topic later in this thesis.

As for quadratic phase modulation, several methods are mentioned by R. Salem et al.[8]. The most straightforward of these is to use an Electro-Optic Modulator (EOM)[14]. In an EOM, the refractive index of an electro-optical crystal is changed by applying and external electric field resulting in a phase modulation of an optical field propagating through the modulator. If the modulator is driven sinusoidally, the applied phase will be quadratic to a good approximation near the extrema of this sine. The magnitude of the phase that can be applied is determined by the driving voltage V_m and the voltage required in order to achieve a phase shift of π, V_π. This method is of course limited by the time window during which the phase shift is quadratic to a good approximation but also of the ratio of maximum V_m to V_π, which determines the achievable chirp, and is typically a single digit number. Since we need a long aperture for TDM to WDM conversion, and a large chirp, an EOM based time-lens is not practical in this case. For other time-lens applications on the other hand such as generation of ultra short pulses[15], where the time scales of interest are much shorter it can still be very useful. A different approach is to use Cross Phase Modulation (XPM). In Kerr nonlinear media, for high enough intensities the refractive index will depend on the intensity of the electric field. If a signal is co-propagating in time with a pump that has a parabolic intensity profile this will result in the desired chirp. An advantage of this is that any medium will have some Kerr nonlinear-

ity since this is a third order nonlinear effect. The drawback is that high pump powers are needed in order to realize XPM and the fact the this high power also leads to self phase modulation of the pump pulse which leads to distortion of the output. In this case, we would also need to create a pump pulse that exhibits the correct parabolic intensity profile over a long time scale, which is not a simple task.

The approach which will be the focus of this thesis is to use degenerate Four-Wave Mixing (FWM) which is another third order nonlinear effect (see appendix A for more detail). In this FWM process two pump photons of frequency ω_p combine with a signal photon of frequency ω_s to create an idler photon at the frequency $\omega_i = 2\omega_p - \omega_s$, resulting in an idler with the electric field:

$$E_i(\tau) = \eta E_p^2(\tau) E_s^*(\tau), \tag{1.59}$$

where η is the Conversion Efficiency (CE) of the FWM process. Since the output is just the product of the pump and signal fields, we only need to engineer the phase of the involved fields to get the desired output. The phase can be tailored by applying the appropriate dispersion through methods as the ones mentioned above instead of having to shape the intensity of the pulse as in the case of XPM based time-lensing and at the same time the magnitude of the applied chirp is only limited by the amount of dispersion that can be generated and the pump bandwidth. The time window of the time-lens also is not limited by factors such as the frequency of the driving voltage as in the case of the EOM time-lens. An important factor to note is the complex conjugate of the signal in the FWM process which is a result of the signal being ”mirrored” around the pump frequency and the squaring of the pump field. Both of these must be taken into account when designing a FWM based time-lens. In eq. (1.52), we saw that the dispersion of the waveform to undergo OFT and the chirp of the pump must have the relation $C = 1/D_2$ to properly cancel each other out. Since the phase of the pump gets doubled due to the squaring of the pump field and the sign of the signal phase gets flipped due to the conjugation of the field, the relevant term now becomes:

$$0 = -2CD_s - 1 \tag{1.60}$$

$$0 = -\frac{2}{D_p} D_s - 1 \tag{1.61}$$

where D_p and D_s is the dispersion applied to the pump and signal

respectively. As a result,

$$D_s = -\frac{D_p}{2} \tag{1.62}$$

for a FWM based time-lens.

The implementation of OFTs based on the above mechanisms has been carried out for more than a decade at the time of writing, with the FWM based time-lens implementation being the most popular due to the magnitude of the lensing action only being limited by the maximum dispersion achievable. Many uses of OFTs have been demonstrated such as the ultra fast optical oscilloscope[16], generation of flat-top pulses(although this can also be achieved using only the dispersive OFT as demonstrated in the paper)[17] and of course the conversion of TDM to WDM signals to which considerable attention has been dedicated over the last decade by our research group[11,18,19,20]. Most of this work has been done in purely fiber based systems, although some work has been done on generating OFTs with integrated waveguides as the FWM medium[21,19]. Basing an OFT system fully or partly on fiber has both advantages and disadvantages. The main advantage is the low loss exhibited by optical fiber which makes generating dispersion easier since the magnitude of dispersion that can be obtained is dominated by the loss as previously mentioned. The main disadvantages is that the FWM process is harder to carry out in optical fiber due in large part to the fact that the mode is much less confined, with the result that the intensity of the light will be much lower.

1.3 Integrated Photonics

In integrated photonics, just as with fiber optics, light is guided by waveguides created by materials with different refractive indices which leads to light being confined as propagating modes as we saw in eqs. (1.22) and (1.23). In optical fibers intended for transmission at telecommunications wavelengths around 1550 nm, the guiding of light is achieved with a cladding of SiO2 (Silica) and a core of silica with some dopant present which slightly raises the refractive index of the core, allowing the fiber to guide light. In general the advantage of PICs over fiber optics stems from the possibility for miniaturization. Integrated photonics platforms typically have a much larger contrast between core and cladding refractive indices, which leads to stronger confinement of light and allows for very small bend radii for integrated

circuits. Due to the strong confinement of light and thus smaller mode volume, for some given power contained in a laser field, the intensity of the light gets amplified relative to a fiber. Additionally, fiber based systems are vulnerable to drifts in polarization due to temperature fluctuations, which makes the CE unstable and PICs are less vulnerable to this. If one is interested in initiating a nonlinear interaction, as is the case in this project, both advantages are extremely valuable thing. Since the activation of a nonlinear process depends on some given threshold intensity, the high intensity due to the strong confinement of light helps us here. On the flip side, the main issue with integrated photonics compared to fiber photonics is the fact that the loss of an integrated waveguide tends to be much higher: typical loss in an optical fiber used for long haul transmission is 0.2 dB/km in the C-band[22] while loss in PICs tends to be on the order of single digit dB/cm, although this varies to a large degree across different platforms. Other variations between platforms include the magnitude of the nonlinear susceptibilities, ease of fabrication, waveguide birefringence and minimum bending radius of waveguides. All these parameters will carry different weight depending on what is being designed and in which context. In the following, I will go more into detail about the merits and drawbacks of some platforms for integrated photonics

1.3.1 Platforms

Several useful parameters for evaluating various photonics platforms exist. In the context of linear photonics, such as generation of delay, only various sources of loss will matter. This will mainly be determined by the linear loss and Two Photon Absorption (TPA) of of a waveguide. Here linear loss is determined in part by the intrinsic losses of the materials used for the waveguide and in part by the geometry of the waveguide. TPA is a source of loss where two photons combine to excite an electron and since two photons are required, the loss due to TPA (β_{TPA}) scales with the square of the optical intensity[23]. Since a free carrier is generated from TPA, additional losses are introduced which will depend on the lifetime of the free carrier, which will vary depending on the material. In order to evaluate the applicability of a material for nonlinear photonics, its nonlinear parameter must be compared to its β_{TPA}. In the context of third order processes dependent on the Kerr nonlinearity, n_2, the nonlinear parameter is defined as:

$$\gamma = \frac{\omega n_2}{c A_{\text{eff}}}, \tag{1.63}$$

where ω is the pump frequency and A_{eff} is the Effective Mode Area (EMA). γ is largely fixed by the choice of platform since n_2 is a material property and cannot be changed. A_{eff} is a consequence of the waveguide geometry and the index contrast of the platform, so while the waveguide geometry can be modified to some degree, other considerations will keep the geometry more or less fixed. Since β_{TPA} and not the linear loss will be the limiting factor in a nonlinear process, a figure of merit for the usefulness of a platform in the context of nonlinear photonics can be defined as, the Figure Of Merit (FOM)[24]:

$$\text{FOM}_{\text{TPA}} = \frac{n_2}{\beta_{\text{TPA}}\lambda}, \tag{1.64}$$

with λ being the pump wavelength. A larger FOM signifies a better platform for nonlinear photonics, with a value above 1 roughly corresponding to good platform. Alternatively, for platforms where no TPA is present, an alternative FOM based on the linear loss of the platform can be defined as:

$$\text{FOM}_{\text{alt}} = \frac{\gamma}{\alpha}, \tag{1.65}$$

where α is the linear loss coefficient of a given waveguide. The interpretation of this FOM is somewhat different than the first one as the linear loss of a waveguide depends on both the design and fabrication quality of the waveguide and not just on intrinsic qualities of the material. Thus, it is a measure of how good a specific waveguide is and not a direct measure of how useful a platform has potential to be for nonlinear photonics.

1.3.1.1 Silicon-on-Insulator

The Silicon-On-Insulator (SOI) platform is possibly the most widely used platform for implementing PICs and consists of crystalline silicon deposited on a layer of insulating silica. The main reason for its wide adoption is its compatibility with Complimentary Metal–Oxide–Semiconductor (CMOS) fabrication. As the name suggests, this allows for homogeneous integration of photonic and electric circuits, and more importantly nearly all electric integrated circuits are produced using CMOS technology. This means that production of SOI circuits can draw upon the experience of an already existing massive industry, which gives the platform an edge in terms of fabrication precision compared to other less developed platforms and allows for fabrication of circuits with feature sizes down to 10 nm at a comparatively low price. In SOI silica has a refractive index of $n_{\text{SiO}_2} = 1.44$ at

1550 nm and this coupled with the fact that Si has a refractive index of $n_{\text{Si}} = 3.48$ leads to a very high confinement of light. This in turns leads to it being possible to create very narrow waveguides that allow for small bending radii and in turn for very densely integrated circuits without introducing loss. This high index contrast has its downsides too. A high index contrast means that the cross sectional area of a waveguide needs to be smaller in order for it to be single moded. In this case, waveguides become much more susceptible to losses induced by sidewall roughness as can be seen from the results by D. Melati et al.[25]. SOI also has some unfortunate nonlinear losses as its TPA coefficient, is quite large[26] at 1550 nm. Silicon has an indirect band gap which means that after an electron has been excited to the valence band by TPA, it needs a change of momentum in order to decay back to the valence band and this results in a long average lifetime for free carriers, which leads to additional losses. All in all, these effects lead to a high absorption for high input powers in SOI waveguides, with $\beta_{TPA} = 1.38$ cm/GW[27]. Another result of the indirect band gap is that it is very hard to make light emitting devices or detectors in SOI. Finally, since crystalline silicon is centrosymmetric the there is no $\chi^{(2)}$, which means that there is no direct way of implementing light emitters and sensors in SOI. The third order nonlinearity on the other hand is always present in a material and silicon has the Kerr coefficient $n_2 = 4 \cdot 10^{-14}$ cm^2/W[27] which is quite large. Based on very similar results D. Moss et al.[24] find that $\text{FOM}_{\text{TPA}} = 0.3$, which is a strong indication that silicon is not the ideal platform for nonlinear photonics.

The results in the preceding discussion has been based on crystalline silicon. Alternatively amorphous silicon can be used, which has been shown to have both higher n_2 and lower β_{TPA} than that of crystalline Silicon (c-Si), with one group[28] finding $n_{2,aSi} = 2.1 \cdot 10^{-13}$ cm^2/W and $\beta_{\text{TPA}} = 0.5$ cm GW^{-1} resulting in $\text{FOM}_{\text{TPA}} = 5$. As is evident, SOI based on c-Si has a very large nonlinear coefficient but suffers from the fact that TPA is very strong in it, which strongly limits the amount of power that can be input to a nonlinear process and a nonlinear FOM of 0.3. In the end, the cheapness and ease of fabrication due to the platform being CMOS compatible has led it to being extremely widespread and useful despite the drawbacks. For a more detailed overview, see for example J. Leuthold et al.[29] or X. Chen et al.[30]. Waveguides based on a-Si overcomes some of these issues with a FOM that is an order of magnitude larger than that of c-Si, but it re-

mains to be seen if it will become a widely used platform for nonlinear photonics.

1.3.1.2 Silicon Nitride

Si_3N_4 (SiN) is another material that is used in conjunction with silica as with SOI (but unlike it, it will be referred to as SiN). This means that it shares some attributes with SOI such as it being easy to work with and having no second order susceptibility. The refractive index of SiN at 1550 nm is $n_{SiN} = 1.99$, which means that optical modes in general are less confined. This leads to significantly less linear loss but also to larger bend radii and less dense integration. SiN has a Kerr index of $n_2 = 2.6 \cdot 10^{-15}\text{cm}^2/\text{W}$. This is an order of magnitude less than that for silicon, but as it has no TPA this does not limit nonlinear effects as in silicon.

This fact has been used to show impressive results in nonlinear optics, such as the widest ever supercontinuum pulse at the time of publication by R. Halir et al.[31]. Different SiN platforms exists all optimizing for different objectives. A platform of special interest here since it was utilized in this project, is the LioniX Triplex platform that tries to strike a balance between very low losses and relatively low bending radius. This is achieved using an Asymmetric Double Stripe (ADS) platform[32], with two SiN layers of different thickness placed on top of each other. This leads to a minimum bending radius of 100 µm and propagation loss on the order of 0.01 dB/cm. Although the balance between low loss and relatively small bending radii being possible, it must be expected that A_{eff} is lower than for an equivalent box waveguide, since the mode is spread over the two layers with silica in the middle, which will lead to a lower γ which should be taken into account if nonlinear processes are desired. M. Pu et al.[33] uses data from J. S. Levy et al.[34] to find $\text{FOM}_{\text{alt}} = 0.09$. In this paper, $\alpha = 0.5$ dB/cm so it is possible that a higher FOM could be reached by using a platform like the ADS since the loss is 50 times lower. At the same time, with the reduced mode area, it is not sure that the FOM would improve.

1.3.1.3 Thin Film Lithium Niobate

Bulk Lithium Niobate (LN) has been in use for EOMs for decades owning to its large Pockels coefficient and wide optical transparency window ($0.35 \sim 5$ µm). After it became possible to fabricate high quality thin-film LN wafers and etching techniques for creating circuits were developed, Lithium Niobate On Isolator (LNOI) started to gain traction as a platform for integrated photonics. As implied by the presence of the Pockels effect, LN is a non-centrosymmetric crystalline mate-

rial. At a wavelength of 1550 nm it has ordinary and extraordinary refractive indices $n_o = 2.21$ and $n_e = 2.13$. As a result of a relatively large index contrast with respect to silica, strong confinement of light is possible in integrated LNOI waveguides, which in turn leads to the possibility of strong interactions between a propagating mode and the different nonlinearities of LN. One use of this combination of facts is the construction of highly efficient EOMs as demonstrated by M. Li et al.[35], by tuning the resonance frequency of a photonic crystal cavity by applying a voltage. Since the propagating mode is highly confined inside the core of the waveguide and as the Pockels effect is very strong an applied voltage strongly shifts the effective index the mode. As a result, they are able to demonstrate high-speed EO modulation at low switching energies. Many other essential photonic building blocks have been implemented in LNOI, as covered in great detail by D. Zhu et al.[36]. One potential issue with the LNOI platform is that although it is possible to etch LN, direct etching of LN is not perfected and leaves the waveguide walls slanted[37], which for some devices is undesirable. One way to avoid the complications related to the etching of LN is to make a rib waveguide by depositing a material with a lower index than that of LN on top of it and etching this instead. This has been demonstrated to great success with SiN, which is easily etchable and has low intrinsic material loss as previously mentioned. By constructing a waveguide in this way, the rib of SiN will lead to guiding of the mode while keeping most of the modal field concentrated in the LN, thus keeping most of the advantages of LN while still enabling etching of waveguides using a mature technology. At the time of writing research into developing a full set of building blocks for PICs is ongoing, with elements such as high speed EOMs[38], efficient gratings couplers[39] and mode and polarization (de)multiplexers[40] having been demonstrated and combined into larger scale PICs[41].

LNOI also has a Kerr nonlinearity with a nonlinear refractive index of $n_2 = 1.8 \cdot 10^{-15}$ cm^2/W, at 1550 nm[36], which is comparable to that of SiN. The FOM of SiN on LNOI cannot be estimated on the other hand, as I have found no data for β_{TPA} at 1550 nm. An interesting consequence of both strong second and third order nonlinear effects along with the presence of the electro-optic effect is the possibility of creating monolithic circuits combining many different effects, such as Kerr comb generation and line modulation, with only CW light as the input as demonstrated by C. Wang et al.[42], third order non-linear

effects are applied along with the electro-optic effect. This result is of course in pure LNOI, but due to the nature of the SiN on LNOI platform, both effects are also present in this platform.

1.3.1.4 AlGaAs

$Al_xGa_{1-x}As$ (AlGaAs) is a material that exhibits a strong third order nonlinearity[43], which is on the order of $n_2 \approx 10^{-13}$ cm^2/W, and like with lithium niobate also exhibits a strong second second order nonlinearity[44], which is interesting for some of the same reasons as with LNOI. Additionally, the refractive index of AlGaAs is $n_{AlGaAs} \approx 3.3$ which makes it possible to construct waveguides with high confinement of light. In comparison with SOI it has an even larger third order nonlinearity. Finally, by modifying the aluminum content of the material (x), the band gap can be engineered to minimize TPA at telecom wavelengths, which in combination with the large magnitude of n_2 can lead to very strong nonlinear interactions. In[45], $\beta_{TPA} = 0.05$ cm/GW is demonstrated, but smaller values are possible and many works see no TPA at the powers of interest. Using the values of n_2 and β_{TPA} reported here leads to FOM $= 129$. This FOM will of course change for different wavelengths and different $Al_xGa_{1-x}As$ compositions. In[46] several values of both n_2 and β_{TPA} are listed for different material compositions.

With these excellent nonlinear properties AlGaAs-On-Isolator (AlGaAs-OI) especially has shown some impressive results, such as using dispersion engineered waveguides to eliminate group velocity dispersion for supercontinuum generation[47]. Ultra high conversion efficiency in a FWM process has also been demonstrated in AlGaAs-OI[33], with a conversion efficiency of - 4 dB over a range of 1280-2020 nm.

1.3.1.5 Overview

The choice of platform depends largely on what one intends to do. In the case of linear photonics, as in the case of generating dispersion where very long waveguides are needed, the main parameters of interest are losses of the platform (which will in our cases includes both the linear loss and TPA since the light that is meant to undergo dispersion also will be a high powered signal) and the minimum bending radius of the platform. In this case, the best platform to use is arguably SiN since exceptionally low losses has been demonstrated here. With the 0.01 dB/cm loss, a 1 m long CBG could in principle be implemented with only 2 dB of loss for the wavelengths that propagate the maximal distance. On the other hand, strong nonlinear interac-

tions are also required in order to implement the time-lens itself. SiN can in principle be used here since the required nonlinearity exists and no TPA is present, but since the low linear losses exhibited here also depends on the waveguide geometry a highly confining waveguide where A_{eff} is small would also lead to increased losses. A clear choice for nonlinear photonics is AlGaAs with its large n_2 meaning that significant FWM can occur for relatively short waveguides. LNOI also has strong nonlinear interactions but is more suited for implementation of devices like EOMs and a complication with this platform is that the refractive index depends on the direction of propagation relative to the crystal lattice. Considering all this, the optimal way of integrating an OFT time-lens, would likely be heterogeneous, with a SiN layer to carry out the linear interactions in and a AlGaAs layer to carry out the nonlinear interactions in. In the end, the overarching concern for this project has been price and availability. Heterogeneous integration has not been possible due to the complexities associated with this type of integration. Instead most work has been done in SOI, despite the fact that it is neither the ideal passive nor nonlinear platform, due to high quality fabrication of PICs in this platform being readily available. One chip was also tested with a SiN on LNOI platform as a result of an exchange at InPAC at RMIT, where they mostly work with their own SiN on LNOI platform. One chip for testing of linear circuits such as large dispersion CBGs was also design for the LioniX ADS platform, but unfortunately, the chip was never received before the end of this PhD project.

1.4 Integrated Optical Time-Lenses for Passive Optical Networks

In this introductory chapter we have presented what a PON is and how the power splitting of the TDM signals used in it makes it a highly energy inefficient way of transmitting data to many consumers at one time. The alternative of using WDM signals also ends up begin highly energy inefficient, since this approach requires individual lasers for each CO receiving data, with each laser having a considerable overhead in energy consumption. By transforming an outgoing TDM signal to a WDM signal using an OFT, the shortcomings of each type of PON is overcome since the transformed signal can be split losslessly to each CO using an AWG. This removes the original inefficiency of the TDM based PON and also gives this new Lens-PON system the reach of a WDM-PON, potentially resulting in a considerable increase

in energy efficiency. Lens-PON systems has already been demonstrated by this research group in fiber based systems[18,19,20], but this work has been carried out in fully or partly fiber based systems. These systems are bulky and due to the efficiency of nonlinear optical processes depending on the confinement of the modes involved, they are also inefficient compared to what can potentially be achieved in an integrated system. These factors removes the system as contender in future optical communication networks. Due to this we propose integrating the main components of the time-lens: the dispersion generating waveguides and the FWM waveguides. This would reduce both the size and energy consumption of a Lens-PON and make it a viable option in an optical communication network. The rest of this thesis will concern the specifics of how a time-lens OFT can be integrated and the experimental work we have done to further this goal.

2 Elements of a Photonic Time-Lens

In this chapter we will discuss how to implement the basic components needed for an integrated OFT to work. These components consist of dispersion generating waveguides, waveguides for FWM and filters for removing the pump after FWM.

2.1 Dispersive Elements

As explained in section 1.2.2 a key ingredient in generating an OFT is dispersion. From eqs. (1.22) and (1.23), we saw that dispersion in general is a result of the shape of a waveguide along with the interaction of the field with the materials that make up the waveguide. Over a narrow enough range of wavelengths, the dispersion of a waveguide will tend to be approximately linear, so in previous demonstrations of Lens-PON systems in the group, this dispersion has been achieved by propagating the signals through either several kilometers of Single Mode Fiber (SMF)[48] with an appropriate dispersion profile or through hundreds of meters of Dispersion Compensation Fiber (DCF)[19]. Since the goal of this project is to implement an OFT system on a PIC, these length scales are not possible. This is both due to constraints on footprint (even for a very narrow waveguide, hundreds of meters of waveguide would result in an unacceptably large footprint) and that even with an ultra low loss photonic waveguide with a loss of 0.05 dB/cm[49] the accumulated loss through hundreds of meters of waveguide would be prohibitively large. Another problem with this approach was demonstrated by my colleague Xiaoyu Xu[13], when she explored the impact of Third Order Dispersion (TOD) on an OFT. Here she showed that TOD leads to distortions of the output in a TDM to WDM conversion process and in general TOD will typically be present in a waveguide. As a result of these factors, a way of generating on-chip dispersion that is both more efficient and leads to highly linear delay as a function of wavelength is needed.

One way of achieving high dispersion is by using a ring resonator as demonstrated in[50]. Near the resonance of a ring resonator, very large dispersion occurs. As shown in this paper, dispersion ranging from $12.9 \cdot 10^3$ ps/nm to $-12.3 \cdot 10^3$ ps/nm can be achieved using this

method. Unfortunately, dispersion of this magnitude is only achieved close to the resonance wavelength and the usable band is narrower than 0.1 nm. This range can be widened but at the cost of lower dispersion. In our case, we will need linear dispersion over a range of several nm, which makes this method imperfect for our use case. Another way of generating very high dispersion is by using photonic crystal waveguides. In these, light is confined and guided by a multi-dimensional periodic structure, with the periodic structure typically made up of holes in the substrate. Due to this periodicity, only light of certain wavelengths will be able to propagate through the waveguide and by properly engineering the waveguide, a substantial slowing of the propagation speed of the allowed wavelengths can be achieved[51]. Here again, the problem is that photonic crystal waveguides typically has quite high loss, limiting their utility in our case. What we will use instead chirped Bragg grating, which has long been know to be able to compensate for dispersion in optical fibers[52]. The Bragg grating utilizes periodic index modulations in the propagation medium (and can therefore be seen as a 1D photonic crystal), which in the case of integrated waveguides is achieved by modulating the effective index, to induce localized reflections at wavelengths matching the period of the index modulation. Thus, by varying the modulation period along the length of the propagation medium, different wavelengths of light will be reflected at different points along the length of the propagation medium leading to a wavelength dependent propagation delay. This means that the dispersion that can be achieved is mostly limited by how long the grating can be made and the linear losses of the waveguide the grating is based on. Importantly for our case, Bragg gratings can also be implemented in photonic systems[53], by periodically modulating the dimensions of the waveguide which changes the effective index of the mode propagating in the waveguide.

2.1.1 Bragg Gratings

As a completely general definition, a Bragg Grating (BG) is a medium where the refractive index varies periodically along some axis. In our case, it will be a fiber or photonic waveguide where the periodic index variation is in the effective index of the mode that is propagating. Due to the periodicity of the medium, it can be thought of as a 1D photonic crystal and a stop-band where no light propagates in the waveguide appears for certain frequencies of light. A simple model of a Bragg grating is shown in fig. 2.1, which will illustrate the basic principle of a Bragg grating.

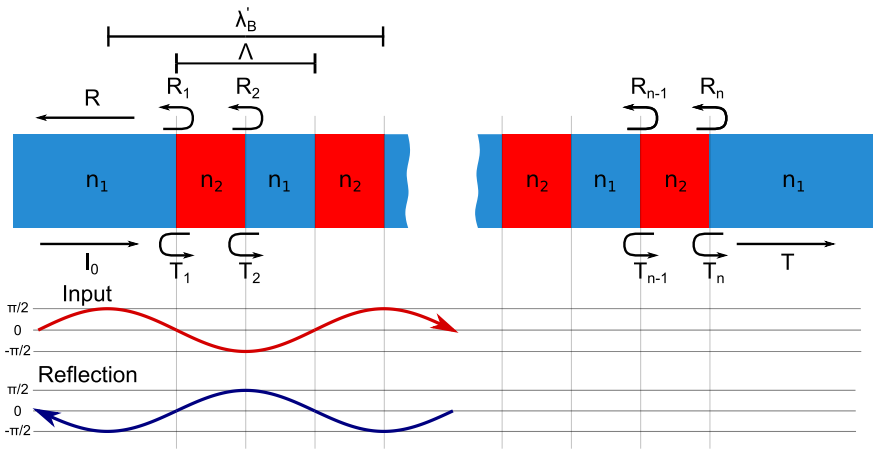

Figure 2.1: A simple Bragg grating composed of n layers of alternating materials with refractive indices of n_1 and n_2, with N interfaces between layers. Each layer is of length $\Lambda/2$, where Λ is the period of the grating. $\lambda_B^{'} = 2\Lambda$ is the wavelength in the material. The impinging electric field has an intensity of I_0, with the reflected and transmitted intensity being R and T respectively. The bottom shows the phase evolution for the input and reflected waves for the first few interfaces.

This grating is a medium which consists of n slices of material alternating between refractive indices of n_1 and n_2 (where for the purposes of this illustration $n_2 > n_1$). These slices in turn lead to $N = n - 2$ interfaces between layers of different index. Each layer has a width of $\Lambda/2$, with Λ being the period of the grating At the beginning of the waveguide on the left side an electric field with intensity I_0 is propagating towards the right. At each of the n interfaces between layers a small fraction of the light, R_n, will be reflected due to the difference in refractive index between each layer, $\Delta n = n_2 - n_1$. As we know from Fresnels law, larger $|\Delta n|$ leads to more light reflected at each interface. Additionally, this tells us that the the reflected light gains a phase of π upon reflection at an interface where we go from a low to a high index. Due to this flip of phase at every second interface, we see that the sum of all the reflected components will interfere constructively when:

$$\lambda_B = 2\bar{n}\Lambda, \tag{2.1}$$

where $\bar{n} = \frac{n_1+n_2}{2}$ is the average of the two refractive indices and λ_B resonance wavelength of the grating, called the Bragg wavelength.

In terms of the wavelength inside the material this is:

$$\lambda_B^{'} = 2\Lambda, \tag{2.2}$$

where $\lambda_B^{'}$ is the Bragg wavelength in the material. In the sketch in fig. 2.1, the change in wavelength that occurs due to the difference in refractive index is not shown. The sketch can also be seen as the case where $\Delta n \approx 0$ in which case it would hold that only λ_B would be reflected from the grating. If $\Delta n > 0$, the result is a region around λ_B where reflections can interfere constructively instead of just a single wavelength. This region will have the width $\Delta\lambda \propto \Delta n$. Since only a fraction of the incident light is reflected from each interface, the magnitude of the total reflected power will depend on both the length of the grating and the size of Δn. The amount of power reflected and the bandwidth will both depend on the coupling coefficient, κ, which expresses the reflection per unit length of a given grating. By applying Fresnels law to the above low level discussion, κ for reflection between identical modes can be found readily, but for a more rigorous approach let us turn to Coupled-Mode Theory (CMT), which will allow us to analyze how light is coupled between different modes that are not necessarily of the same order.

Coupled mode theory is explored in depth in A. Yarivs widely cited work[54], which explores how CMT can be used to calculate the magnitude of scattering between different modes in a waveguide when a perturbation is introduced. In this formalism, we are concerned with two modes, which in our case is the backward propagating mode:

$$\mathbf{E}_a(\mathbf{r}, t) = A(z)F_a(x, y)e^{i(\omega_a t + \beta_a z)} \tag{2.3}$$

and the forward propagating mode:

$$\mathbf{E}_b(\mathbf{r}, t) = B(z)F_b(x, y)e^{i(\omega_b t - \beta_b z)} \tag{2.4}$$

where $A(z, t)$ and $B(z, t)$ are the complex envelopes of the two modes. The modes are assumed to be orthogonal and normalized to:

$$\int_{-\infty}^{\infty}\int_{-\infty}^{\infty} F_i(x, y)F_j(x, y)dxdy = \frac{2\omega\mu}{\beta_i}\delta_{i,j} \tag{2.5}$$

If a periodic index perturbation is introduced, coupling of power between the two modes will become possible and the envelopes will be

depend on the z-coordinate in the following way:

$$\frac{dA}{dz} = \kappa_{ab} B e^{-i\Delta z} \tag{2.6a}$$

$$\frac{dB}{dz} = \kappa_{ba} A e^{i\Delta z}, \tag{2.6b}$$

where Δ is a phase-mismatch term and κ_{ab} and κ_{ba} are the coupling coefficients to and from the two modes, which describes how much power is exchanged between them per unit length. In the specific case of contra-directional coupling conservation of energy can be expressed as:

$$\frac{d}{dz}\left(|A|^2 - |B|^2\right) = 0, \tag{2.7}$$

which is satisfied if:

$$\kappa_{ab} = \kappa_{ba}^*. \tag{2.8}$$

Physically this can be interpreted as requiring that the rate at which one mode loses energy is matched by the rate at which the other mode gains energy. To find an expression for κ we analyze what happens to a waveguide mode propagating in an initially unperturbed waveguide, which is described by the wave equation, eq. (A.9), and explore what happens when a perturbation to the polarization of the medium, $\mathbf{P}_{pert}$, is introduced. In the perturbed case, the y-component of the electric field of a TE mode, indexed l, obeys the wave equation:

$$\nabla^2 E_y^{(l)}(\mathbf{r}, t) = \mu\epsilon \frac{\partial^2 E_y^{(l)}}{\partial t^2} + \mu \frac{\partial^2}{\partial t^2} P_{pert,y}(\mathbf{r}, t). \tag{2.9}$$

If we limit ourselves to working with the discrete, confined TE modes of the waveguide, the field of the mode can be written as:

$$E_y^{(l)}(\mathbf{r}, t) = \sum_l \frac{A_l(z)}{2} F_y^{(l)}(x, y) e^{i(\omega_l t - \beta_l z)} + \text{c.c.}. \tag{2.10}$$

Inserting eq. (2.10) into eq. (2.9) yields:

$$\begin{aligned}
\sum_l \Bigg\{ & \frac{1}{2} \frac{\partial^2 A_l(z)}{\partial z^2} F_y^{(l)}(x, y) e^{i(\omega_l t - \beta_l z)} \\
& + \frac{\partial A_l(z)}{\partial z} \left[\nabla \cdot F_y^{(l)}(x, y) e^{i(\omega_l t - \beta_l z)} - i\beta_l F_y^{(l)}(x, y) e^{i(\omega_l t - \beta_l z)} \right] \\
& + \frac{1}{2} A_l(z) \nabla^2 \left[F_y^{(l)}(x, y) e^{i(\omega_l t - \beta_l z)} \right] + \text{c.c.} \\
& = \mu\epsilon \frac{\partial^2 E_y^{(l)}(\mathbf{r}, t)}{\partial t^2} + \mu \frac{\partial^2}{\partial t^2} P_{pert,y}(\mathbf{r}, t).
\end{aligned} \tag{2.11}$$

The first term on the left side can be neglected since $\partial^2 A_l(z)/\partial z^2 \ll \beta_l \partial A_l(z)$ for a slowly varying envelope and the $\nabla \cdot F_y^{(l)}(x,y)$ term disappears since $\nabla \cdot \mathbf{E} = 0$ in the absence of free charges. Additionally, the third terms on the left side fulfills the original wave equation and cancels with the first term on the right side, leaving us with:

$$\sum_l -i\beta_l \frac{\partial A_l(z)}{\partial z} F_y^{(l)}(x,y) e^{i(\omega_l t - \beta_l z)} + \text{c.c.} \\ = \mu \frac{\partial^2}{\partial t^2} P_{pert,y}(\mathbf{r},t). \tag{2.12}$$

We can now multiply eq. (2.12) with $F_y^{(m)}(x,y)$ and integrate over the full plane, which due to the orthonormality of the modes gives us:

$$\frac{\partial A_m^{(-)}}{\partial z} e^{i(\omega_m t + \beta_m z)} - \frac{\partial A_m^{(+)}}{\partial z} e^{i(\omega_m t - \beta_m z)} + \text{c.c.} \\ = -\frac{i}{2\omega} \frac{\partial^2}{\partial t^2} \int_{-\infty}^{\infty} \int_{-\infty}^{\infty} P_{pert,y}(\mathbf{r},t) F_y^{(m)}(x,y) dx dy, \tag{2.13}$$

which is the equation that governs coupling between modes due to a perturbation of the propagation medium. Here we can see the resemblance between the earlier equations describing coupling between two modes A and B, eqs. (2.6a) and (2.6b), with the coupling coefficient κ being related to the right hand term of eq. (2.13), which contains the overlap integral of the mode in question and the dielectric perturbation. In general this perturbation can arise from many phenomena such as the electro-optic effect or the photo-elastic effect, but in the case of integrated Bragg gratings it will be as a result of waveguide corrugations, as illustrated in fig. 2.2. Here an initially uncorrugated waveguide of width w is shown, consisting of a core of refractive index n_{co} and a cladding of refractive index n_{cl}. The core height of the waveguide is assumed to be h. At $z = 0$ the waveguide is corrugated symmetrically around the center in a sinusoidal fashion which changes its width between $w - 2\delta$ and $w + 2\delta$ over a period of Λ. As:

$$\mathbf{P} = [\epsilon(\mathbf{r}) - \epsilon_0]\, \mathbf{E}, \tag{2.14}$$

so we can write the perturbation as:

$$\mathbf{P}_{pert} = \Delta\epsilon(\mathbf{r}) \mathbf{E}(\mathbf{r},t) \tag{2.15}$$

$$= \Delta n^2(\mathbf{r}) \epsilon_0 \mathbf{E}(\mathbf{r},t), \tag{2.16}$$

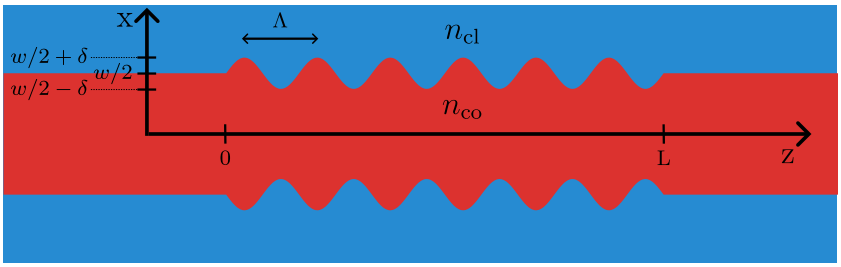

Figure 2.2: A waveguide of width w with core and cladding index of n_{co} and n_{cl} respectively. At the position $z = 0$ a symmetrical sinusoidal corrugation of amplitude 2δ and period Λ starts and continues until $z = L$ after which the waveguide is uncorrugated again.

where $\Delta\epsilon$ and Δn are the changes in permittivity and index due to the corrugation of the waveguide respectively. Let us now consider what happens when a single forwards propagating TE mode, m, is introduced. In this case the perturbation along the $y-$axis becomes:

$$P_{pert,y}(\mathbf{r},t) = \frac{\Delta n^2(\mathbf{r})\epsilon_0}{2}\left[A_m^{(+)}(z)F_y^{(m)}(x,y)e^{i(\omega_m t+\beta_m z)} + \text{c.c.}\right], \tag{2.17}$$

which we can insert into eq. (2.13). If we are interested in how coupling occurs to the backwards propagating mode with index l, we can ignore the forward propagating term and we have:

$$\begin{aligned}\frac{\partial A_l^{(-)}}{\partial z} =& \frac{i\omega\epsilon_0}{4}A_m^{(+)}(z)e^{i([\omega_m-\omega_l]t-[\beta_m+\beta_l]z)} \\ &\cdot\int_{-\infty}^{\infty}\int_{-\infty}^{\infty}\Delta n^2(\mathbf{r})F_y^{(m)}(x,y)F_y^{(l)}(x,y)dxdy.\end{aligned} \tag{2.18}$$

If we consider the case where $l = m$, this reduces to:

$$\begin{aligned}\frac{\partial A_m^{(-)}}{\partial z} =& \frac{i\omega\epsilon_0}{4}A_m^{(+)}(z)e^{-2i\beta_m z} \\ &\cdot\int_{-\infty}^{\infty}\int_{-\infty}^{\infty}\Delta n^2(\mathbf{r})\left[F_y^{(m)}(x,y)\right]^2 dxdy.\end{aligned} \tag{2.19}$$

In the situation in fig. 2.2:

$$\Delta n^2(\mathbf{r}) = \Delta n^2(x)\Delta n^2(y)\,\mathrm{sin}(\eta z), \tag{2.20}$$

where $\eta = 2\pi/\Lambda$. $\Delta n^2(x)$ is:

$$\Delta n^2(x) = \begin{cases} n_{\text{co}}^2 - n_{\text{cl}}^2 & \text{for} \quad w' - \delta \leq |x| \leq w' + \delta \\ 0 & \text{elsewhere} \end{cases}, \tag{2.21}$$

where $w' = w/2$. The fact that the index difference is $n_{\text{cl}}^2 - n_{\text{co}}^2$ half of the time is accounted for by the sin ηz term in $\Delta n^2(\mathbf{r})$. $\Delta n^2(y)$ is:

$$\Delta n^2(y) = \begin{cases} 1 & \text{for} \quad 0 \leq y \leq h \\ 0 & \text{elsewhere} \end{cases}. \tag{2.22}$$

Here $\Delta n^2(y) = 1$, since the height of the waveguide remains unchanged. We write $\Delta n^2(x)\Delta n^2(y)$ as $\Delta n^2(x, y)$ and inserting the above into eq. (2.19), we get:

$$\begin{aligned} \frac{\partial A_m^{(-)}}{\partial z} =& \frac{\omega \epsilon_0}{8} A_m^{(+)}(z) e^{i(\eta - 2\beta_m)z} \\ & \cdot \int_{-\infty}^{\infty} \int_{-\infty}^{\infty} \Delta n^2(x, y) \left[F_y^{(m)}(x, y) \right]^2 dxdy, \end{aligned} \tag{2.23}$$

which governs coupling between the forward and backward propagating TE_m mode in a waveguide with sinusoidal corrugations that are even about the center of the waveguide. We see from the phase term that unless $\eta \approx 2\beta_m$, a phase depending on z will be introduced which will lead to negligible coupling to the backward propagating mode for long enough grating length. Since $\eta = 2\pi n_{\text{eff}}/\Lambda$ and $\beta_m = 2\pi/\lambda_m$ this is more rigorous statement that reflection in a Bragg grating for a given mode occurs near the wavelength:

$$\lambda_B = 2n_{\text{eff}}\Lambda. \tag{2.24}$$

Defining $\eta - 2\beta_m = \Delta$ we can rewrite the coupling equation as:

$$\begin{aligned} \frac{\partial A_m^{(-)}}{\partial z} =& \frac{\omega \epsilon_0}{8} A_m^{(+)}(z) e^{i\Delta z} \\ & \cdot \int_{-\infty}^{\infty} \int_{-\infty}^{\infty} \Delta n^2(x, y) \left[F_y^{(m)}(x, y) \right]^2 dxdy. \end{aligned} \tag{2.25}$$

Comparing with eq. (2.6b), we can identify the coupling coefficient in this case as:

$$\kappa = \frac{\omega \epsilon_0}{8} \int_{-\infty}^{\infty} \int_{-\infty}^{\infty} \Delta n^2(x, y) \left[F_y^{(m)}(x, y) \right]^2 dxdy. \tag{2.26}$$

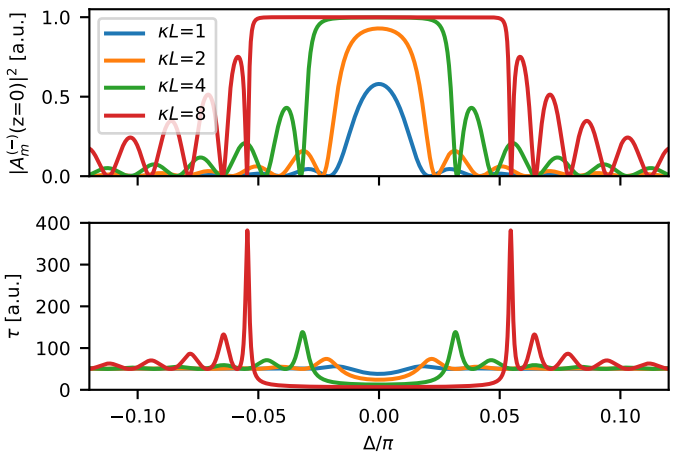

Figure 2.3: Plot of reflection and group delay versus detuning for various values of κ.

The integral is the overlap between the mode and itself modified by the perturbation to the waveguide, so we can see that the larger δ is the, the larger κ will be, which fits well with our initial low level analysis of a Bragg grating. If the $A_m^{(+)}(z=0)=1$ and $A_m^{(-)}(z=L)=0$ we have from (see appendix B) that the amplitude of the backward propagating mode as a function of z is:

$$A_m^{(-)}(z) = 2\kappa B_0 e^{-i\Delta z/2} \frac{\sinh\left[\frac{S}{2}(z-L)\right]}{i\Delta \sinh\left[\frac{SL}{2}\right] - S\cosh\left[\frac{SL}{2}\right]}, \tag{2.27}$$

where $S=\sqrt{4\kappa^2-\Delta^2}$. This result is valid for any grating or other type of periodic waveguide perturbation, while of course κ and Δ must be derived for the specific case in question. In fig. 2.3, $|A_m^{(-)}(0)|^2$ and the group delay,

$$\tau = -\frac{d}{d\omega}\arg\left[A_m^{(-)}(0)\right], \tag{2.28}$$

is plotted over a range of Δ's for different values of the total coupling strength, κL. We see that for larger values of this, the reflection at $\Delta=0$ increases until all light is reflected within a certain bandwidth. From D. Oser et al.[55], we have that this bandwidth as defined by distance between the two first zeroes in $|A_m^{(-)}(0)|$ away from $\Delta=0$

is:

$$\Delta\lambda = \frac{\lambda_B^2}{\pi n_{\text{eff}}}\sqrt{\kappa^2 + \frac{\pi^2}{L^2}}, \tag{2.29}$$

so the bandwidth increases with κ and decreases with L. The L term approaches zero for long enough grating lengths, after which $\Delta\lambda$ is only determined by κ. In the plot of the group delays, we see that τ approaches zero inside the main reflection band for large κL and then rapidly increases near the band edges, with $\tau \propto \kappa L$ in this region. This means that the field in the middle of the reflection band is essentially reflected instantly for strong coupling strengths. For lower coupling strengths the light propagates further into the grating proportionally to the length of the grating before $A_m^{(+)}$ is converted into the counter propagating mode, leading to a larger group delay. The group delay of the light in the regions near the band edges is much larger than the delay that would be generated just by traveling to the end of the grating and back again. My interpretation of the large increase in τ is that light in this region, which is not perfectly phase matched with the grating, is reflected many times back and forth between different points inside the grating and finally gets partially reflected back into the counter propagating mode, leading to a very large group delay.

Outside the main reflection band several side lobes are seen, which is characteristic for Bragg gratings. These side lobes are due to the shape of the grating with the perturbation starting sharply as we see in fig. 2.2. If the perturbation starts at zero and adiabatically increases these side lobes are removed. In this case, the situation amounts to placing an ”adiabatic” Bragg grating inside a Fabry-Perot cavity. Close to resonance, a Fabry-Perot cavity imparts a phase on the light reflected or transmitted by it and this phase compensates for the detuning relative to the resonance of the grating allowing for some light to be reflected from it. The further detuned the light is relative to the Bragg grating, the larger the phase contribution from the cavity must be. This means that the light is also further detuned relative to the cavity resonance and less light is transmitted by, which explains why the side lobes gradually decrease with $|\Delta|$. This cavity effect can be illustrated by comparing the reflection from two gratings where one is double the length of the other and this case is plotted in fig. 2.4, where the side lobes for two Bragg gratings of length L_0 and $2L_0$ is compared. The free spectral range of the cavity with the length $2L_0$ is half that of the one with a length of L_0 and thus the one with double

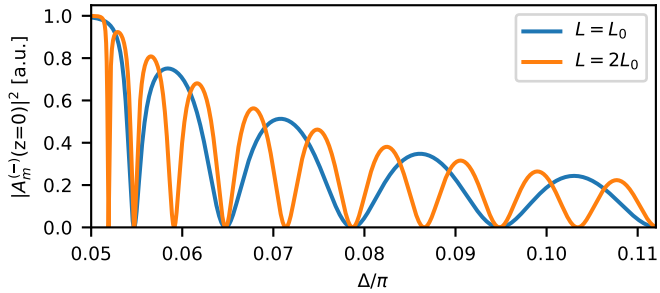

Figure 2.4: A comparison between the side lobes in the reflection of a Bragg grating for the grating lengths L_0 and $2L_0$, where it can be seen that doubling the grating length doubles the frequency of the side lobes.

the length has twice the amount of side lobes, but otherwise the decrease in the magnitude of the side lobes follows the same evolution as no other parameters of the cavity have been changed.

Returning to the group delay, we saw that this changes rapidly near the band edges of the main reflection band, and we are of course discussing Bragg gratings in the context of generating dispersion. Due to this rapid change in group delay, a large amount of linear dispersion is generated in a subset of this region. Of course, the dispersion also occurs on the edges of the reflection band, so losses would be introduced by using this as a method of dispersion generation. Of larger detrimental effect to our purposes, the bandwidth where substantial dispersion is generated is very small since a large group delay is only generated for large κL, which in turns makes the cutoff very sharp and for the type of time-lens we want to implement, we will in general require a wider bandwidth over which dispersion is generated. In order to do this, we can employ chirped Bragg gratings, where the period of the grating is changed along the length of the grating. When this is done, light is reflected from the region in the grating where the light is phase matched with the local grating period. If the Bragg condition is linearly changed such that light with wavelength λ_1 is reflected at $z = 0$ and light with wavelength λ_2 is reflected at $z = L$, this results in a linear dispersion. The magnitude of this dispersion is simply the maximal distance traveled divided by the propagation velocity in the

waveguide and chirp bandwidth, $\Delta\lambda_B = \lambda_2 - \lambda_1$:

$$D_2 = \frac{2L}{v}\frac{1}{\Delta\lambda_B} = \frac{2L}{c}\frac{n_g}{\Delta\lambda_B}, \tag{2.30}$$

which has units of ps/nm. The preceding discussion of CMT has all been based on the assumption that the grating is uniform, that is, neither κ or Λ changes. In order to generate the desired dispersion we will need to change both of these along the length of the grating and no analytic result for these nonuniform gratings with an arbitrary shape can be found and we must instead turn to numerical methods.

2.1.2 Transfer Matrix Modelling

To simulate the transmission and reflection of Bragg grating with an arbitrary shape, we turn to Transfer Matrix Modelling (TMM). TMMs are used to describe how the amplitude of two modes with input amplitudes A_{in} and B_{in} and output amplitudes A_{out} and B_{out} are related if they are transmitted through and optical component described by the transfer matrix $\overline{\mathbf{T}}$. The relationship is:

$$\begin{bmatrix} A_{in} \\ B_{in} \end{bmatrix} = \overline{\mathbf{T}} \begin{bmatrix} A_{out} \\ B_{out} \end{bmatrix}. \tag{2.31}$$

This type of model can be used to describe a variety of systems if $\overline{\mathbf{T}}$ is known. In the case an arbitrary (symmetric) Bragg grating, we can model it as a layered dielectric medium and construct a transfer matrix for any grating based on this[56]. In this model, we treat the grating as a large number of thin slices that are each described by their refractive index and slice length. The transmission and reflection coefficients of each slice, t_i and r_i, can be found using Fresnels law and the phase accumulated in each slice can be calculated based on its optical path length as illustrated in fig. 2.5. If A is the forward propagating and B is the backward propagating mode of a grating, the changes in amplitude resulting from reflection and transmission at the i^{th} interface between slices is described by:

$$\begin{bmatrix} A_i \\ B_i \end{bmatrix} = \frac{1}{t_i}\begin{bmatrix} 1 & r_i \\ r_i & 1 \end{bmatrix}\begin{bmatrix} A_{i+1} \\ B_{i+1} \end{bmatrix} = \overline{\mathbf{T}}_{r,i}\begin{bmatrix} A_{i+1} \\ B_{i+1} \end{bmatrix} \tag{2.32}$$

The reflectivity and transmittance in the above can be expressed as:

$$r_i = \frac{n_i - n_{i+1}}{n_i + n_{i+1}} \tag{2.33}$$

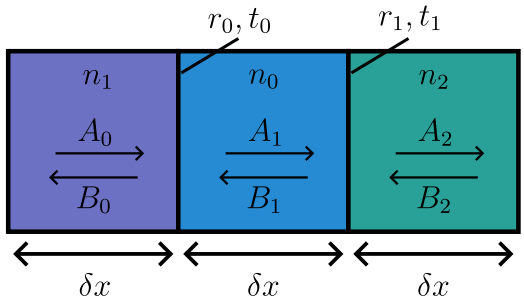

Figure 2.5: Some waveguide sliced into three thin layers, each of length δx. Each layer has a refractive index, n_i, a forward propagating field, u_i and a backwards propagating field, v_i associated with it. The interface between each layer also has a reflectivity, r_i, and transmittance, t_i, associated with it.

and

$$t_i = \frac{2n_i}{n_i + n_{i+1}}. \tag{2.34}$$

Likewise, the phase shift the modes experience due to propagation through the i^{th} layer can be expressed as:

$$\begin{bmatrix} A_i \\ B_i \end{bmatrix} = \begin{bmatrix} A^{i\phi_i} & e^{i\phi_i} \\ B^{-i\phi_i} & e^{-i\phi_i} \end{bmatrix} \begin{bmatrix} A_{i+1} \\ B_{i+1} \end{bmatrix} = \overline{\mathbf{T}}_{\phi,i} \begin{bmatrix} A_{i+1} \\ B_{i+1} \end{bmatrix}, \tag{2.35}$$

with the phase shift, ϕ_i, being:

$$\phi_i = \frac{2\pi n_i \delta x}{\lambda}, \tag{2.36}$$

where λ is the wavelength of the light. The total transfer matrix for each slice and interface is then:

$$\overline{\mathbf{T}}_i = \overline{\mathbf{T}}_{r,i} \overline{\mathbf{T}}_{\phi,i}, \tag{2.37}$$

with the total transfer matrix for the structure then being the product of all the transfer matrices for the individual slices:

$$\overline{\mathbf{T}} = \prod_{i=0}^{N} \overline{\mathbf{T}}_i = \begin{bmatrix} T_{11} & T_{12} \\ T_{21} & T_{22} \end{bmatrix}. \tag{2.38}$$

If we assume that the input amplitude of the forward propagating mode is $A_{in} = 1$ and that the output amplitude of the backward propagating mode is $B_{out} = 0$, we have:

$$\begin{bmatrix} 1 \\ B_{in} \end{bmatrix} = \begin{bmatrix} T_{11} & T_{12} \\ T_{21} & T_{22} \end{bmatrix} \begin{bmatrix} A_{out} \\ 0 \end{bmatrix} \tag{2.39}$$

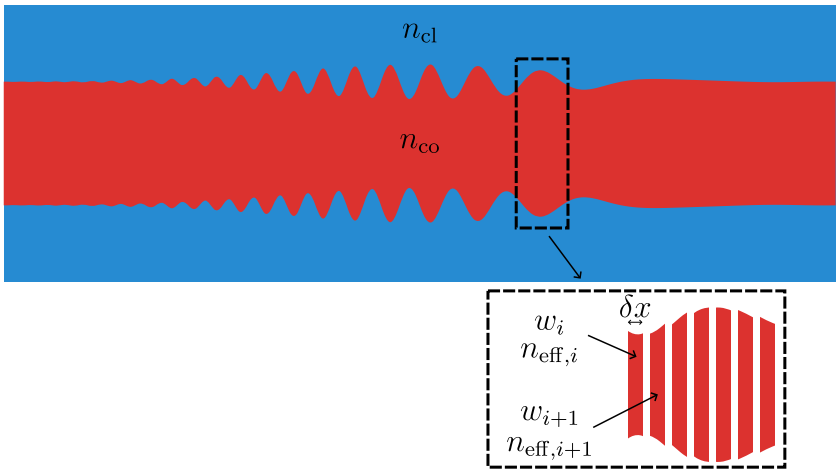

Figure 2.6: An illustration of a Bragg grating where both Λ and κ changes along the length of the grating the transfer matrix method is applied to calculate its reflection and transmission. The grating is a waveguide of initial core width, w, with a core refractive index of n_1 and a cladding refractive index of n_2, $n_1 > n_2$. The width of the core is modulated up to a maximum change in width of Δw. In the cutout the application of the transfer matrix method is illustrated. The waveguide is cut into layers of length δx and the width of the layer, w_i is taken as the width of the waveguide on the left side of the section. From the width, the effective index of the layer, $n_{\mathrm{eff},i}$ is calculated.

From this we can see that the transmittance of the grating, the amplitude of A_{out} is:

$$t = \frac{1}{T_{22}} \tag{2.40}$$

and that the reflectivity of the grating, the amplitude of B_{in}, is:

$$r = \frac{T_{21}}{T_{11}}. \tag{2.41}$$

Using this, we can simulate any Bragg grating as long as the length of each layer, δx, is sufficiently small compared to the wavelength of the light and the period of the grating. How this method is applied for Bragg grating is illustrated in fig. 2.6. The grating is a waveguide with a core refractive index of n_1 and a cladding refractive index of n_2. At either end of the waveguide the core width is w which is then modulated periodically up to a maximum width change of Δw. The waveguide is the split up into sections of length δx, which have some

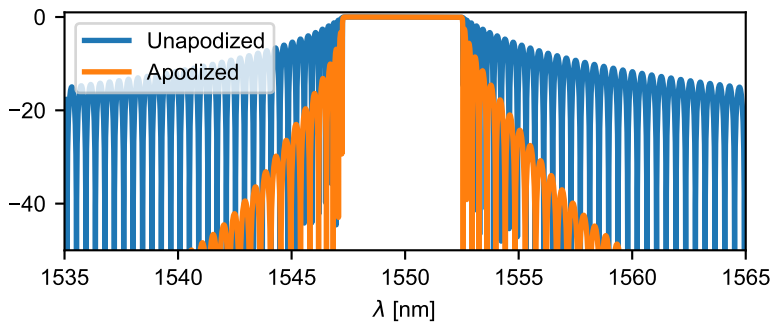

Figure 2.7: Simulation results for the reflection of an apodized and an unapodized Bragg grating. Both grating have $h_{\text{Si}} = 250$ nm, $w = 800$ nm, $\Delta w = 50$ nm, $L = 1000$ µm and $\lambda_B = 1550$ nm.

width w_i. From this width, the effective index of the section, $n_{\text{eff},i}$, can be simulated and the transfer matrix method can be applied.

Using my own implementation of the TMM, I will look at how Bragg gratings with different parameters perform. The implementation is explained in more detail in section 4.1. First let us take a look at how an unchirped grating behaves. In figurefig. 2.7, the difference in behavior between an unapodized and an apodized Bragg grating is shown. In the simulations $h_{Si} = 250$ nm, the gratings have a base width of 800 nm and a corrugation depth of of 50 nm. Immediately it is clear that the apodization massively reduces the side lobes of the reflection spectrum, which can be useful if one desires to create a filter with a sharp roll-off. Here the apodization profile is based on a hyperbolic tangent as is defined as:

$$A(z) = \frac{1}{2} + \frac{1}{2}\tanh\left[\beta\left(1 - 4\frac{z - \frac{L}{2}}{\frac{L}{2}}\right)^{2\alpha}, \right] \tag{2.42}$$

where α and β can be used to control how sharply the profile rises. Additionally, the profile is normalized relative to its maximum value after calculation. In figure fig. 2.8, eq. (2.42) is plotted for several different combinations of α and β. As can be seen here, α controls how far along the length of the grating that the waveguide corrugation is turned on, while β controls how sharply the corrugation is turned on. This is of course only broadly speaking as the interplay between the two factors is more complex than that, but it gives a good general

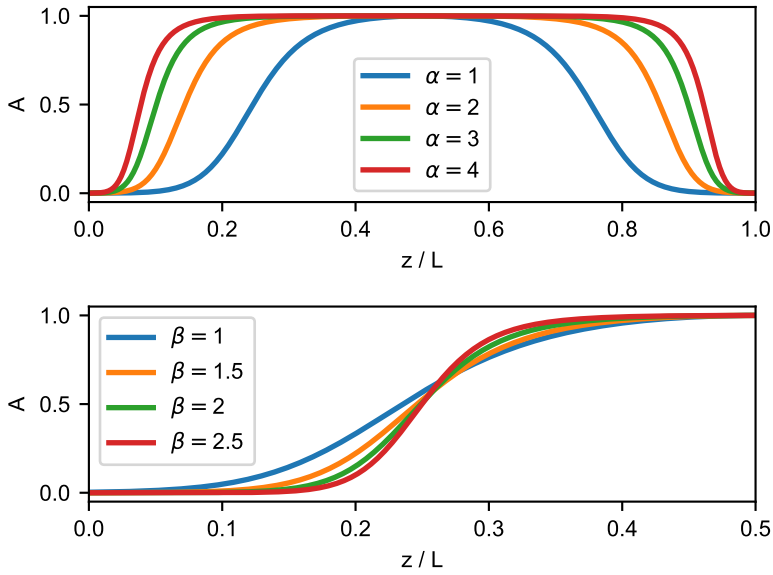

Figure 2.8: Plots of $A(z)$ for different values of α and β along the length of a grating of length L. In the upper plot $\beta = 1.5$ and in the lower plot $\alpha = 1$.

view of how the function behaves. In fig. 2.7, $\alpha = 3$ and $\beta = 1.5$. Naturally other profiles can be used, such as Gaussian or sine profiles, as described in[57]. This type of tanh profile is practical since it strikes a good balance between leaving most of the grating unchanged such that the magnitude of the reflection is mostly unchanged, while still smoothly changing at either end of the grating in a way that effectively reduces the previously mentioned cavity effect that is present in unapodized Bragg gratings. Of course, this also depends on the length of the grating. If the grating is very short since the change in amplitude will still be very sudden depending on the choice of α and β and side lobes will not be suppressed efficiently. Therefore, these parameters should be chosen according to need and extra care must be taken for short gratings.

Let us now turn to the behavior of a Chirped Bragg Grating (CBG). In fig. 2.9, the reflection from two chirped Bragg gratings is shown. They both have a chirping bandwidth of $\Delta\lambda = 10$ nm, but are otherwise identical to the gratings shown in fig. 2.7. In the unapodized case we see that large ripples are present in the group delay, as a result of

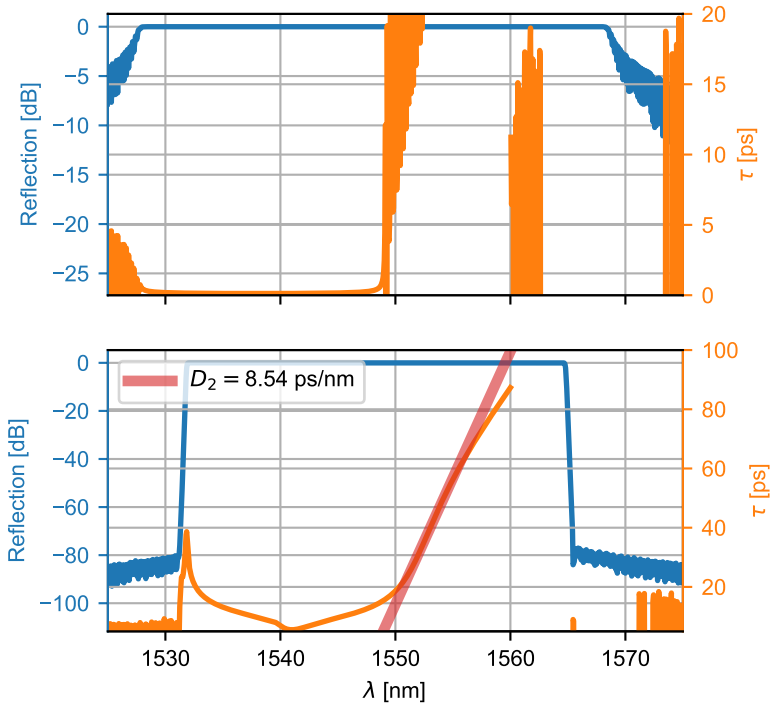

Figure 2.9: Simulation results for the reflection of an unapodized (upper) and unapodized (upper) chirped Bragg grating. Both grating have $h_{\mathrm{Si}} = 250$ nm, $w = 800$ nm, $\Delta w = 100$ nm, $L = 5000$ µm, $\lambda_B = 1550$ nm and $\Delta\lambda_B = 10$ nm. The reflected power is shown in blue on the right and the group delay is shown on the right in orange. The linear part of the dispersion for the apodized grating is marked and is $D_2 = 8.54$ ps/nm.

the interaction between the Bragg grating and the cavity effect. In the apodized case the ripples are removed and leads to an area of linear dispersion. λ_B is swept linearly from 1550−1560 nm in this case.

As a conclusion to this section, we have seen that Bragg gratings with an arbitrary shape can be simulated by modelling the grating as a layered dielectric medium and then using TMM. Using this, we have demonstrated that in order to use a CBG to generate linear dispersion, it must be apodized with an apodization profile that is appropriate for the grating in question. In the paper by X. Xu's et al.[20] a time-lens based on dispersive fiber CBGs with the CBG with the larger dispersion having $D_2 = 494$ ps/nm is used to to map a 4 GBit/s

TDM signal to a WDM signal with a 100 GHz frequency grid. In order to implement this in an SOI CBG with $\Delta\lambda = 10$ nm, a CBG length of approximately 30 cm would be needed. With a linear loss of 1 dB/cm, this would not be possible to achieve. Using a TripleX ADS waveguide with a linear loss of 0.05 dB/cm on the other hand, and a length on the same order of magnitude,it would be feasible.

2.1.3 Asymmetric Bragg Gratings

As we saw in the previous section coupling between forward and backward propagating modes of the same order will occur in a symmetrically corrugated waveguide, with the coupling coefficient for the specific case analyzed there shown in eq. (2.26). Let us now turn to the case where the index perturbation is not symmetrical around the center, which we will term an Asymmetric Bragg Grating (ABG), in which case light can be reflected from the fundamental mode of a waveguide into a higher order mode[58,59]. In order to understand this, let us analyze this case. We start again from eq. (2.18) but instead in the case where $l \neq m$. We start by assuming that the corrugation of the waveguide is sinusoidal again:

$$\Delta n^2(z) = \sin(\eta z), \tag{2.43}$$

and that the angular frequencies of the two modes are the same, $\omega_m = \omega_l$, in which case we have:

$$\begin{aligned}\frac{\partial A_m^{(-)}}{\partial z} =& \frac{\omega\epsilon_0}{8} A_l^{(+)} e^{i\Delta z} \\ &\cdot \int_{-\infty}^{\infty}\int_{-\infty}^{\infty} \Delta n^2(x,y) F_y^{(l)}(x,y) F_y^{(m)}(x,y)\,dx\,dy,\end{aligned} \tag{2.44}$$

where $\Delta = \eta - \beta_m - \beta_l$, and the coupling coefficient is:

$$\kappa_{lm} = \frac{\omega\epsilon_0}{8} \int_{-\infty}^{\infty}\int_{-\infty}^{\infty} \Delta n^2(x,y) F_y^{(l)}(x,y) F_y^{(m)}(x,y)\,dx\,dy \tag{2.45}$$

From the phase mismatch, Δ, we can see directly that for significant coupling between modes to occur we need the wavelength to be:

$$\lambda \approx \left(n_{\mathrm{eff},l} + n_{\mathrm{eff},m}\right) \Lambda. \tag{2.46}$$

Still, no coupling between modes is guaranteed to occur since the overlap between modes where $l \neq m$ is zero due to the orthonormality

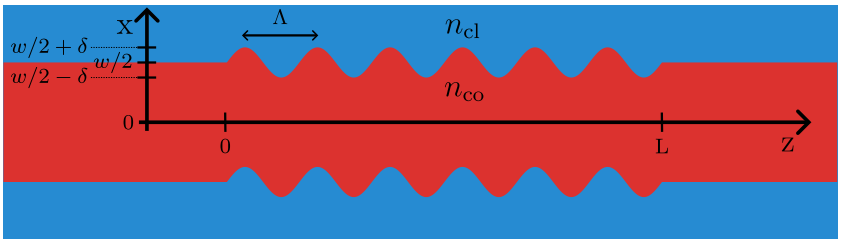

Figure 2.10: An asymmetrically corrugated waveguide. The core and cladding indices of the waveguide are n_{co} and n_{cl} while the period of the corrugation is Λ. The waveguide has a width of w, and a corrugation amplitude of δ.

of the modes. If we take the case where $m = l+1$, one mode is even and the other is uneven around the x axis, so the overlap integral

$$\int_{-\infty}^{\infty}\int_{-\infty}^{\infty} F_y^{(l)}(x,y)F_y^{(m)}(x,y)dxdy = 0 \tag{2.47}$$

simply due to symmetry of the modes. This overlap integral is modified by $\Delta n^2(x,y)$ in the expression for κ, but for a symmetric corrugation profile the situation is unchanged. However, if the corrugation profile is uneven around the x-axis, coupling between modes that fulfill $m = l+1$ becomes possible, such as coupling between the forward propagating TE_0 and backward propagating TE_1 modes of a waveguide. A sinusoidally corrugated waveguide where the corrugations are asymmetric around the z-axis, which would reflect from the TE_0 to the TE_1 mode is shown in fig. 2.10. As can be seen here, instead of changing the width of the waveguide, the corrugation of the waveguide leads to a shift of the center of the waveguide with respect to the $x-$axis by $\pm\delta$ depending on the phase of the corrugation profile. If the height of the waveguide is h, $\Delta n^2(y)$ remains as in eq. (2.22). $\Delta n^2(x)$ on the other hand becomes:

$$\Delta n^2(x) = \begin{cases} n_{\mathrm{co}}^2 - n_{\mathrm{cl}}^2 & \text{for} \quad w' \leq x \leq w'+\delta \\ n_{\mathrm{cl}}^2 - n_{\mathrm{cl}}^2 & \text{for} \quad -w' \leq x \leq -w'+\delta \\ 0 & \text{elsewhere} \end{cases} \tag{2.48}$$

As we saw in eq. (2.29), we can get the bandwidth of a Bragg grating once we know its coupling coefficient and its length, which can be used in the design of ABGs. From eq. (2.45), we can see that if we obtain the mode profile of a waveguide of a given width, κ can be

simulated and the bandwidth of a grating can be obtained. For a symmetric Bragg grating with the index profile

$$n(z) = n_{\text{eff}} + \Delta n \sin(\eta z) \tag{2.49}$$

we have that[60]:

$$\kappa = \frac{\pi \Delta n}{\lambda_B}. \tag{2.50}$$

This can be used as a benchmark to test simulations of κ using CMT. In fig. 2.11, results obtained using equation eq. (2.29) are compared

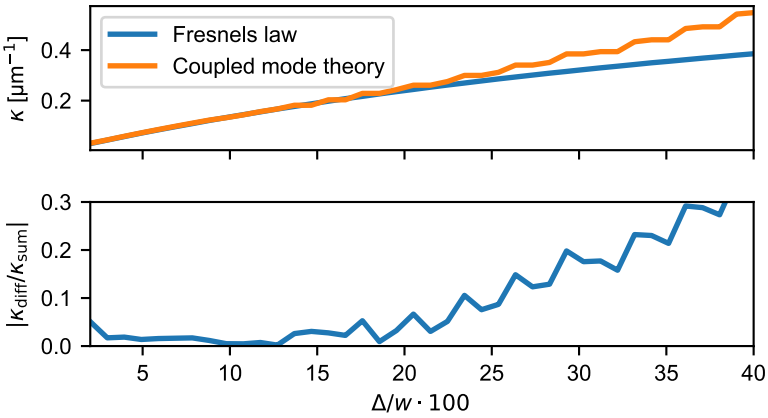

Figure 2.11: κ of a Bragg grating as calculated using eq. (2.29) and eq. (2.45). In this simulation $h_{Si} = 250$ nm, $w = 500$ nm and Δw ranging from 10−200 nm.

with results obtained using eq. (2.45) for a symmetric Bragg grating. As can be seen the results align closely for the two methods for small Δw, but as the Δw exceeds 15% of the waveguide width the results start to diverge and two results relative to each other exceeds 10%. This is a result of the underlying assumption in CMT that the perturbation to the effective index can be treated as just that: a perturbation. In any case, the fact that the two results align so well is good. This is mostly since it confirms that we can calculate κ correctly for the symmetric case where we have a direct comparison available and increases our trust in results gained from calculations of κ for asymmetric gratings where no direct comparison is available. We now move on to simulating κ for an asymmetric Bragg grating. In fig. 2.12, κ for

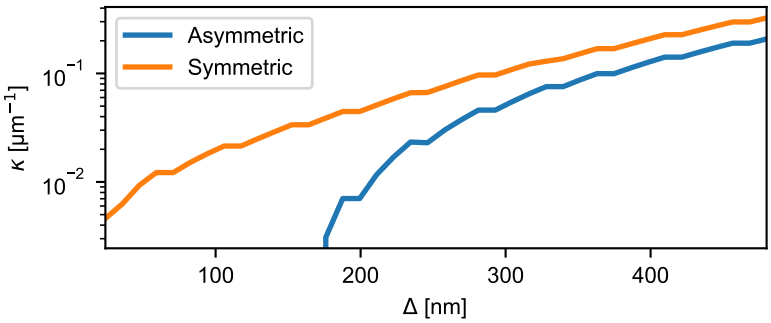

Figure 2.12: Comparison of κ as a function of Δw for a symmetric and an asymmetric Bragg grating based on a waveguide with $w = 1.2$ µm, $h_{Si} =$ 250 nm a

a BG and an ABG based on the same waveguide of width $w = 1.2$ µm is shown as a function of Δw. As can be seen here, the coupling coefficient for the asymmetric grating is significantly smaller, especially for small waveguide corrugations relative to the waveguide width. This is of course due to the low overlap between the TE0 and TE1 mode for the asymmetric Bragg grating and significant coupling only occurs after a certain threshold has been reached. The fact that the coupling disappears completely in these simulation results are an artifact of the simulation and not representative of the physics involved as a small coupling coefficient should always remain as long as a perturbation is present. Just like with a symmetric BG, an ABG can be chirped (creating a Chirped Asymmetric Bragg Grating (CABG)) and be used as a generator of dispersion. The fact that light is reflected into the TE_1 mode, can have its advantages if properly exploited, which we will explore later in section section 3.2.

2.2 Band Stop Filters

After the FWM process, the pump used in the process needs to be filtered out. The important characteristics of the filter for this are the width, the sharpness and the rejection ratio of the filter. That is, how wide is the region where the filter rejects light, how sudden is the transition between the region where light is allowed to pass through and what the ratio is between the powers in the transmission and rejection bands. We need to be able to generate a Band Stop Filter (BSF), which is wide enough cover the spectral width of the pump, which will

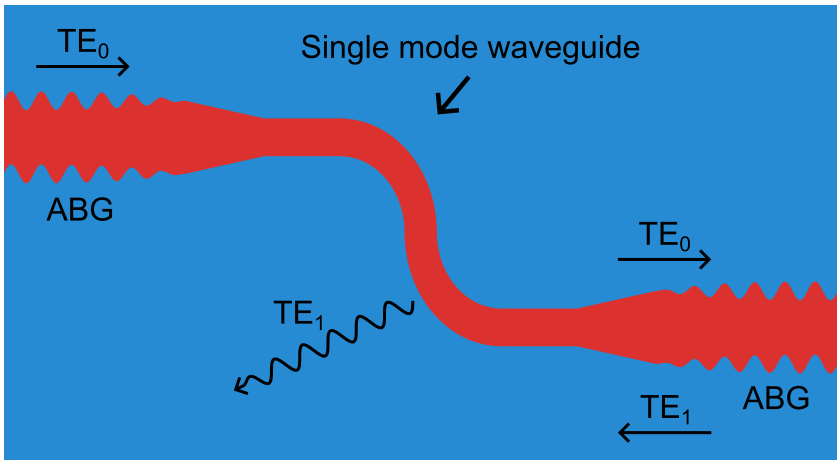

Figure 2.13: Illustration of a CBBG, which consists of two or more ABGs connected by a single moded waveguide s-bend which radiates reflected TE_1 light away.

be up to 10 nm wide. The cutoff of the filter bandwidth should also be sharp in order to allow for the generated idler to have a small detuning relative to the pump, without filtering away parts of the idler. Finally, it should have a large rejection ratio in order to efficiently remove the pump after FWM. One candidate for a filter is a BG as the rejection ratio can get as high as desired given a long enough grating. BGs also have the advantage of offering good control of the width of the pass band through changing the modulation depth of the grating. Unfortunately it is hard to get a rejection ratio that is larger than 30 dB with a photonic Bragg grating implemented as described in section 2.1.1, since small fabrication errors lead to phase fluctuations. These phase fluctuations destroy the coherency over the full length of the grating, and complete coherence is needed in order to achieve an arbitrarily large rejection ratio. An alternative way of implementing an optical filter on chip is by using micro-ring resonators, which can lead to high rejection ratios (40 dB or more) with a relatively compact structure as demonstrated by F. Xia et al.[61]. The problem with this structure is that the filter bandwidth is limited and the rings need to be very small in order to get a large FSR, which is needed such that the filter only overlaps with the pump. A promising concept is based on ABGs. By stacking several ABGs after each other with single mode waveguides where only the fundamental mode can propagate in between, the light reflected from each individual ABG can be radiated

away, thus eliminating the coherency between the individual ABGs as illustrated in fig. 2.13. With this Coherency Broken Bragg Grating (CBBG), there is no coherency between each individual grating and rejection ratios larger than 50 dB can be achieved as demonstrated by D. Oser et al.[55]. Due to the general behavior of BGs, the bandwidth of the rejection band can also be engineered by changing the corrugation depth of the ABG. These two facts: that a large rejection ratio can be achieved and that the size of the rejection band can be engineered, makes this a very attractive power filter in our case.

2.3 Four-Wave Mixing Waveguides

The FWM waveguides in this project are in many ways the simplest part, since the only things under consideration is the CE and phase matching of the process. As discussed in section 1.3.1, the CE is largely determined by the platform, since it depends on the nonlinearity of the material and the EMA of the waveguide, through γ. This means that depending on the choice of platform, γ can only be improved by optimizing the waveguide width such that it results in the smallest possible EMA. The range over which the signal, idler and pump fields stay phase matched in accordance with eq. (A.24), determines the bandwidth of the FWM process. As explained by Kyo Inoue[62], if the pump wavelength is at the zero dispersion wavelength of a waveguide in degenerate FWM, then the process will always be phase matched in the region where the dispersion slope is linear. Walk-off in the FWM process is also determined by the dispersion. This effect is the simple fact that if the different wavelengths involved in the process are experiencing different dispersion, they will start to drift apart spatially as the different wavelengths propagate through the waveguide at different velocities. This of course means that if the walk-off is great enough, the FWM process ends. The effect of this is that for larger dispersion slopes results in a short effective length of a FWM waveguide which can also limit the CE. In the best case then, we have a waveguide where the zero dispersion wavelength and the minimal EMA coincide while the dispersion slope stays linear (and small in relative to the length of the FWM waveguide) over a wide bandwidth. It will not always be possible to achieve all of these at the same time, which means that a trade-off must be made, depending on whether bandwidth or CE is most important in the case at hand.

3 Innovations in Design

In the previous chapter, we presented how to construct the basic elements needed in order to implement an integrated OFT. Here we will present how some of these already existing methods can be improved upon by implementing novel techniques for reducing the loss experienced in the circuits.

3.1 Silicon Circuits Optimized for Low Loss

Losses in integrated photonic are a combination of the inherent material losses of the individual materials that comprise the platform along with the scattering losses that are experienced by a mode propagating in a waveguide. Since the material loss is an intrinsic quality of the material we cannot modify this, but will be a factor under consideration in the choice of platform for a circuit of a given application. Scattering losses on the other hand depend on the geometry of a waveguide along with the tolerances of the fabrication process. The scattering losses of a given waveguide depend on the roughness of the waveguide walls, since any change in the dimensions of the waveguide will result in a change in the effective refractive index of a propagating mode which in turn will lead to scattering of light that can couple either to a backwards propagating mode of the waveguide or to radiative modes, with scattering to the radiative modes typically being the main source of extrinsic loss. Due to the top and bottom of a waveguide typically being polished and therefore having a low roughness, most of the radiative loss is a consequence of the sidewall roughness. Intuitively, one can expect platforms with a high index contrast to have higher losses for a single moded waveguide. Since the mode is more tightly confined and the waveguide having smaller dimension, a given change in the waveguide width due to sidewall roughness will result in a larger change in effective index compared to the same change in waveguide width for a wider waveguide. Following this intuition, one should also be able to reduce the scattering losses in a waveguide by reducing its height, which will allow for a wider waveguide and thus smaller impact of the sidewall roughness while keeping the waveguide single moded. To investigate this idea in a more systematic fashion, we turn to the excellent paper by D. Melati[25], that derives a way to model the losses due to backscatter-

ing and scattering to radiative modes using simulation (although we will keep the discussion to radiative losses here). In the paper, the loss due to radiative scattering, α_r, for a rectangular waveguide of width w and height h is found to be approximated by:

$$\alpha_r \approx A' \frac{\partial n_{\text{eff}}}{\partial w} + A'' \frac{\partial n_{\text{eff}}}{\partial h}, \tag{3.1}$$

where A' and A'' are parameters that describe the shape of the mode and its interaction with the roughness of the vertical and horizontal surfaces respectively, with the surface roughness being described by the standard deviation, σ, and correlation length, L_c, of the roughness. Roughly speaking σ corresponds to the overall magnitude of the surface roughness while L_c describes the length scale over which the roughness is correlated with itself along the surface. Due to the flatness of the horizontal surfaces, scattering due to sidewall roughness will dominate the radiative loss and eq. (3.1) reduces to:

$$\alpha_r \approx A \frac{\partial n_{\text{eff}}}{\partial w}. \tag{3.2}$$

As can be seen, eq. (3.2) fits well with our intuition since $\partial n_{\text{eff}}/\partial w$ will be smaller for less confined modes or wider waveguides.

The task now is to calculate A, which is also detailed in[25]. The method depends on Lacey-Payne model[63] which describes radiative scattering from a 2D planar waveguide. We of course want to describe loss in 3D waveguides and this can be achieved exactly by including the derivative of the refractive index with respect to width as shown in eq. (3.2). The factor A depends on the waveguide parameters in the following way:

$$A = \frac{\sigma^2 L_c k_0^3 (n_{co}^2 - n_{cl}^2)\sqrt{2}}{n_{cl}} n_{\text{eff}} \tilde{f}, \tag{3.3}$$

where n_{co} and n_{cl} are the core and cladding indices of the waveguide and f is:

$$\tilde{f}(x,\gamma) = \frac{\sqrt{[(1+x^2)^2 + 2x^2\gamma^2]^{1/2} + 1 - x^2}}{\sqrt{(1+x^2)^2 + 2x^2\gamma^2}}. \tag{3.4}$$

Here x and γ depend on the terms:

$$\Delta = \frac{n_{co}^2 - n_{cl}^2}{2n_{co}^2}, \tag{3.5}$$

$$W = \frac{w}{2}\sqrt{\beta^2 - n_{cl}^2 k_0^2} \quad \text{and:} \tag{3.6}$$

$$V = wk_0\sqrt{n_{co}^2 - n_{cl}^2} \tag{3.7}$$

as:

$$x = W\frac{2L_c}{w} \quad \text{and:} \tag{3.8}$$

$$\gamma = \frac{n_{cl}V}{n_{co}W\sqrt{\Delta}}, \tag{3.9}$$

with the result that the radiative loss for a rectangular 3D waveguide can be calculated simply by simulating the effective indices of it at different widths and inputting the roughness parameters.

Since low loss in the CBGs is imperative for an integrated time lens, we were interested in investigating how the loss of a SOI waveguide varies with height and width and how much loss can be avoided by changing the aspect ratio of a waveguide while still keeping it single moded. A standard Si height for SOI circuits is 220 nm, while we wanted to attempt creating circuits in a wafer with a Si height of 100 nm. Simulations of the effective indices of waveguide at different widths can be run and the waveguide losses can be calculated using the above results. The results of this for $h = 220$ nm and $h = 100$ nm is shown in fig. 3.1. Some noise is present in the simulation results, which we believe is a result of the way the domain is meshed and does not accurately reflect the true situation. Due to this, the simulation results are shown along with a smoothed version of the data. These results have been calculated using $\sigma = 1$ nm and $L_c = 50$ nm. The figures used for σ and L_c are assumed to be typical for the fabrication facilities available to us as we unfortunately have no direct way of measuring these. This of course prevents us from getting an accurate estimate for the loss we might expect for a given height, but it is still useful for comparing two different Si heights. The simulation results are quite clear, that the maximal loss experienced by a 220 nm tall waveguide is ~ 3 times larger than the maximal loss experienced by a 100 nm tall waveguide. We also see that the cut-off for the TE_1 mode happens at a significantly higher width for $h =$

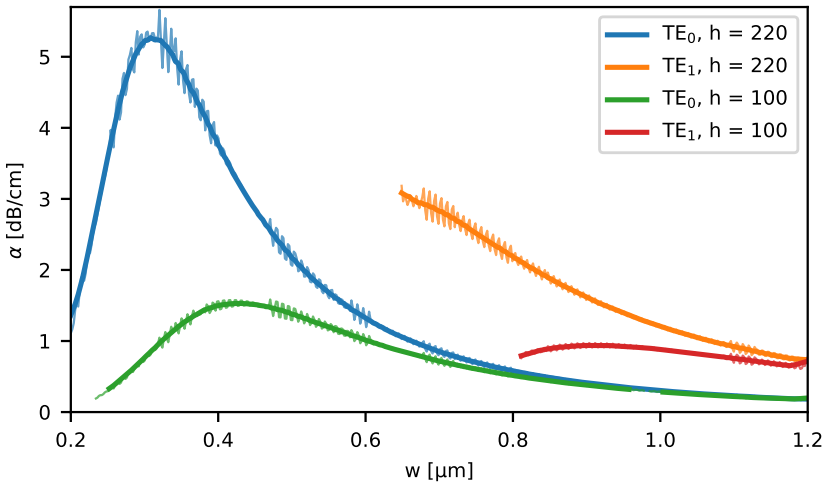

Figure 3.1: Simulated α_r for the TE0 and TE1 modes at varying widths for waveguides with 220 nm and 100 nm Si heights. In these plots $\sigma = 1$ nm and $L_c = 50$ nm. The bold and dark lines show a smoothed version of the faint and narrow lines of the same color.

100 nm. In this case the cutoff happens at 800 nm, while it happens at 450 nm for $h = 220$ nm. This is important because it means that we can make single moded waveguides in 100 nm tall Si that are 800 nm wide and experience a loss of $\alpha = 0.5$ dB/cm. The maximal width of a single mode waveguide in 220 nm tall waveguide is 500 nm, where $\alpha = 2.2$ dB/cm, which means that the loss can be reduced by a factor of 4.4 for a single mode waveguide by switching to 100 nm tall Si. This was an enticing prospect for us, so a chip layout was designed for production on a Si wafer that had been polished to a target Si height of 100 nm. Further elaboration on the design of and experimental results from this chip can be found in chapter 4 and chapter 5.

Another way to make use of these results is to simply make the waveguides so wide that they become multi moded, without going to a thin Si platform. In this case, it becomes possible for the TE_0 mode to back scatter to higher order modes as a result of sidewall roughness but if the sidewall roughness is low, this will not be a large source of loss and as outlined in[25], loss due to back scattering is orders of magnitude lower than the radiative loss. In this case we can design

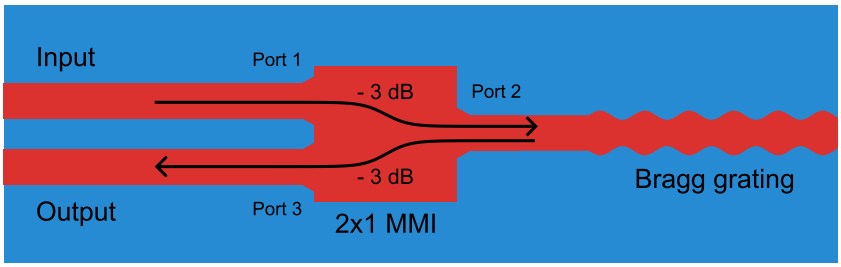

Figure 3.2: Illustration of how a 2x1 MMI can be used to collect the light reflected from a Bragg grating. In the optimal case, 3 dB loss is incurred in each pass through the MMI, leading to 6 dB total loss.

BGs that couple between the forward and backward propagating TE_0 modes and should see lower losses even though the waveguide is multi moded, which is another method of loss reduction that we will investigate.

3.2 Low Loss Access to Dispersed Light

One major issue when using integrated CBGs for dispersion is that the dispersed light is reflected and not transmitted by the device. When using fiber optics this is not an issue as optical circulators can be easily be implemented in this case, which allows for selecting the light that has been reflected from any device with low losses. Unfortunately the function of non-reciprocal devices like this depend on magneto-optically active materials to function and are typically made with bulk optical materials that have proven challenging to heterogeneously integrate with silicon photonics due to the large difference in material properties between the magneto-optic material and silicon. In integrated photonics the issue then is that light reflected from a BG can only be collected in inherently lossy ways. The basic challenge is illustrated in fig. 3.2. In this example, a 2 by 1 Multi-Mode Interferometer (MMI) is employed to couple light to and from the BG. As the input light is coupled from port 1 to port 2 to reach the BG, 3 dB of the input light is lost and as the light reflected from the BG is coupled from port 2 to port 3, 3 dB of light is lost again, leading to a loss of 6 dB relative to the input, even in the case of an otherwise lossless MMI. Due to the reciprocality of non-magneto-optic processes, this will be the case no matter what device is used to couple light to and from the BG, no matter if that is a Y-branch, a Mach-Zender interferometer or any other device. Work has been done in the realization

of non-reciprocal integrated photonics by direct bonding of magneto-optic materials to SOI circuits[64]. That the approach requires access to this type of technology makes it an unfeasible approach for this project. Additionally, although working integrated circulators for SOI have been demonstrated by Y. Shoji et al.[65,66], the insertion loss of the devices remain high with an excess loss of 11.5 dB at 1550 nm in[65] and 11 dB in[66], which in the end makes the implementation of a true optical circulator a moot point in this context.

Since implementation of integrated devices that couple light selectively depending on the directionality are neither feasible nor practical at the time of writing let us instead turn to approaches to solving this problem based on other mechanisms. Several such methods exist such as a method based on an asymmetric Y-branches[67], which unfortunately introduces some unwanted losses. Another approach is based on 2x2 MMIs where the two output ports each are followed by a BG[68]. This method has very low losses, but introduces complexity and a large increase in circuit footprint due to the presence of two BGs. A method based on ABGs and a Multi-Mode Coupler (MMC) exist[69] and caught our attention. Here the problem of filtering light based on its directionality is sidestepped. As we saw in section 2.1.3, we can design ABGs that reflect light from the TE_0 mode to the TE_1 mode by asymmetrically corrugating a waveguide. Dispersion can be generated by a CABG with the dispersed light then reflected into the TE_1 mode. In this case, the directionality of the light will be encoded in the modality of the light, so by designing a device that allows light in the TE_0 mode to pass while coupling all light in the TE_1 mode to the TE_0 mode of another waveguide, we would have a system that carries out the role of a circulator for this specific case, the design of which we will now turn to.

3.2.1 Multi Moded Couplers

Directional couplers in general function by placing two waveguides in the near vicinity of each other. If the evanescent field of the mode in one waveguide overlaps with the evanescent field of the other waveguide, this allows for coupling of power between the waveguides[70]. As light propagates through this coupling section, all power will be transferred from one waveguide after a certain length is traversed and after double this length is traversed, all the power will be back in the original waveguide. In order to gain some intuition about this scenario, the first two TE modes of a system of two identical waveguides, wg_1 and

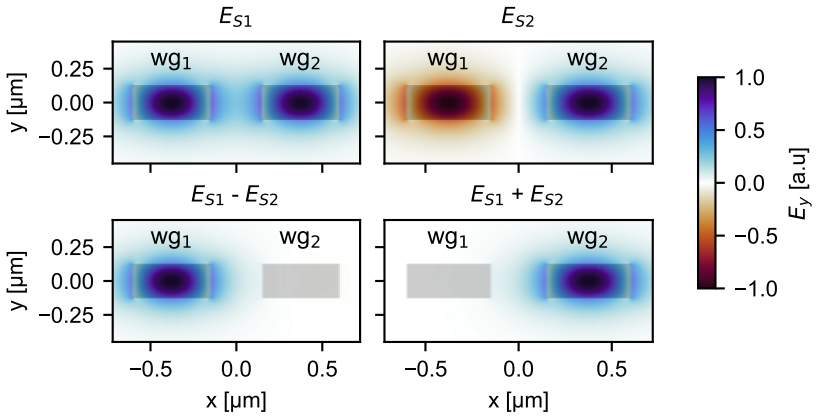

Figure 3.3: The supermodes of a system of waveguides made up of two SOI waveguides with $w = 450$ nm, $h = 250$ nm and a gap width of $w_{\text{gap}} = 300$ nm. As illustrated, the sum and difference of the supermodes closely resemble the TE_0 modes of the waveguides in an uncoupled system.

wg_2, separated by a gap has been illustrated in fig. 3.3. As we see, these modes — the supermodes of the system — add and subtract in a way such that they closely resemble the TE_0 mode of each waveguide by itself. When light in the TE_0 mode enters wg_1 of the coupled system, the light exists as the superposition $E_{S1} - E_{S2}$. Since these supermodes have different effective indices, $n_{\text{eff},S1}$ and $n_{\text{eff},S2}$, they will propagate at different speeds through the waveguide system. By changing the length of the coupling region we can then control the relative phases of these two modes and control how much power ends up in the TE_0 mode of either waveguide after a given length. If the index difference between the two supermodes is:

$$\Delta n = n_{\text{eff},S1} - n_{\text{eff},S2}, \tag{3.10}$$

and there is a power of P_1 in wg_1 at the outset, then the power in wg_2 for a coupling length of L will be:

$$P_2 = P_1 \sin^2\left(\frac{\pi L \Delta n}{\lambda}\right), \tag{3.11}$$

where λ is the wavelength of the light. Using this power integrated power splitters with any desired splitting ratio can be implemented using this type of system.

This can of course also be applied in the context of this section where the goal is low loss access to the light reflected by an ABG. As shown

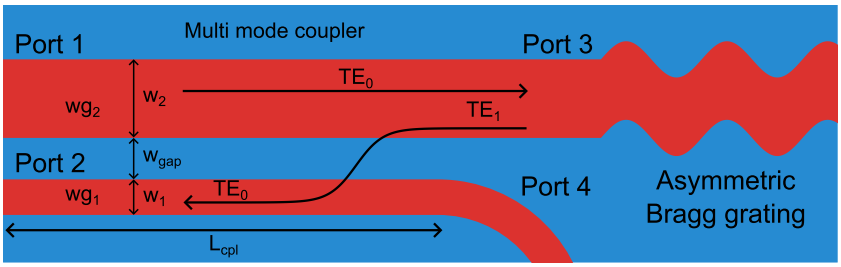

Figure 3.4: Illustration of how a MMC can be used to collect the light from an ABG. In the MMC wg_1 has a width of w_1 and wg_2 has a width of w_2, the gap between the waveguides is w_{gap} and the length of the coupling section is L_{cpl}. Light enters in the TE_0 mode at port 1 and propagates unaffected to port 2, where it encounters an ABG. Here light is reflected into the TE_1 mode and is now coupled from wg_2 to wg_1 and converted back to the TE_0 mode.

by R. Xiao et al.[69], by making one of the waveguides in a directional coupler multi moded and phase matching it with a single moded waveguide, light in the TE_1 mode of the multi moded waveguide can be coupled to the TE_0 mode of the single moded waveguide and vice versa, creating a MMC. How this functions in combination with an ABG is illustrated in fig. 3.4 The MMC comprises two waveguides wg_1 and wg_2 of widths w_1 and w_2, separated by a gap of width w_{gap}. In this case, we want to couple light in the TE_1 mode of wg_2 to the TE_0 mode of wg_2, so these modes need to be phase matched, which means that:

$$n_{\text{eff},0}(w_1) = n_{\text{eff},1}(w_2), \tag{3.12}$$

where $n_{\text{eff},0}$ and $n_{\text{eff},1}$ are the effective indices of the TE_0 and TE_1 modes respectively. Like with the single moded coupler, the sum and difference of the fields of the appropriate supermodes of the waveguide system must closely resemble the modes of the uncoupled system that we want to couple between. It seems that this resemblance is best when phase matching is observed, which is a useful way of graphically verifying results obtained from simulation. An example of the supermodes of the coupled system is shown along with the modes of the uncoupled system is shown in fig. 3.5a, when phase matching is observed. In our case, we want all the power to end up in the TE_0 mode of wg_1, which means that $P_1(L) = 1$ and $P_2(L) = 0$. If we insert this into eq. (3.11) and isolate for L, we find the optimal length for the

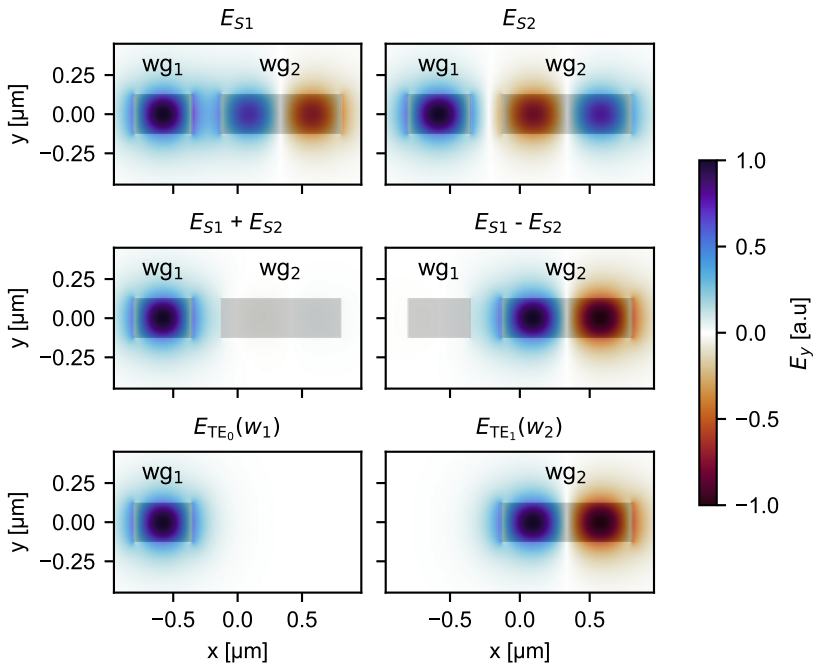

(a)

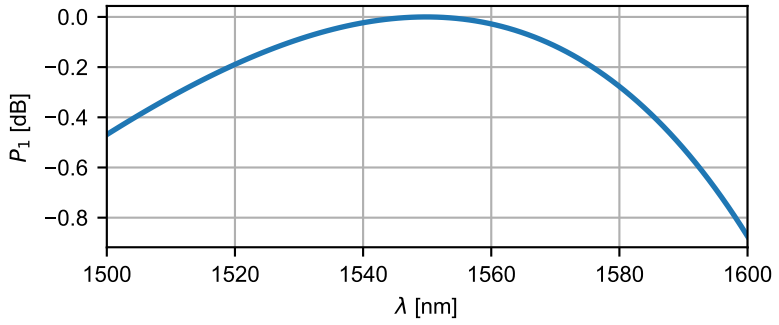

(b)

Figure 3.5: **(a)** The supermodes and the sum and difference of these for a waveguide system comprised of a waveguide with width $w_1 = 450$ nm and $w_2 = 931$ nm. The gap between the waveguides is $w_{\text{gap}} = 220$ nm and the waveguide height is $h = 250$ nm. For comparison, the TE_0 mode of wg_1 and the TE_1 mode of wg_2 is also shown. **(b)** The power coupled to wg_1 for a coupler length of $L = 48.4$ µm with the parameters in **(a)**.

coupler L_{opt}:

$$L_{\text{opt}} = \frac{\lambda}{\pi \Delta n} \tag{3.13}$$

With the parameters from the example in fig. 3.5a, this leads to a coupling length of $L_{\text{opt}} = 48.4$ µm. Using this length we can now calculate the coupled power over a range of wavelengths by simulating the effective indices of the supermodes for these wavelengths. A plot of P_1 in this example is shown in fig. 3.5b. As we see, the coupled power varies by less than 1 dB over a range of 100 nm for this quite realistic example. For a directional coupler with a different splitting ratio than the one in this case, the coupled power is highly wavelength dependent. The reason the coupled power varies so little in this case is that we are sitting at a maximum of the coupling curve. We can think of the coupled power as function of λ, Δn and L and since we are at a maximum, if we change any of these parameters, the coupling will be first order invariant to these changes, with the result that coupling is largely unaffected. This should also mean that the MMC is resistant to small fabrication errors that lead to a change in the waveguide dimensions and thus effective indices, since small changes should lead to negligible change in the coupling. This is of course good for us since it means more room for unintended shifts in wavelength of for instance the Bragg wavelength of any ABG that is implemented in a circuit along with the MMC.

During the study of MMCs we also became interested in how to achieve broad band coupling for splitting ratios different from 1. In single moded couplers, this can be achieved by including a phase control section in the coupler. Here the waveguides have a different width and coupling between the waveguides cannot occur. By choosing an appropriate length for this phase control section, the phase mismatch that leads to a narrow coupling bandwidth can be balanced as explained by Z. Lu et al.[71]. This concept can easily be extended to MMCs, since the only difference the modes that are phase matched. A Broadband Multi-Mode Coupler (BMMC) like this is illustrated in fig. 3.6. It consists of two coupling sections of length L_1, a phase control section of length L_2 and tapers to and from the phase control section of length L_{tp}. In the coupling sections the waveguides wg_1 and wg_2 have the width w_1 and w_2 and are phase matched according to eq. (3.12). In the first tapering section, the width of wg_1 is changed to $w_1 - \Delta w$ and the width of wg_2 is changed to $w_2 + \Delta w$ and in the

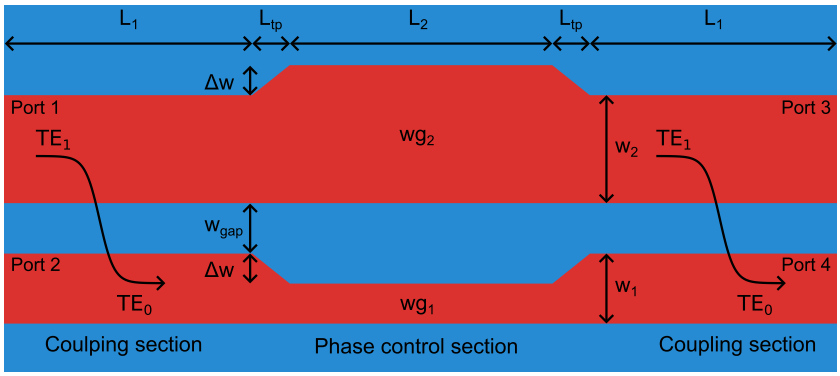

Figure 3.6: A BMMC consisting of the waveguides wg_1 and wg_2. It comprises two coupling sections of length L_1 where the waveguides have the widths w_1 and w_2 respectively and a phase control section of length L_2 where the waveguide widths are changed by $-\Delta w$ and Δw for wg_1 and wg_2 respectively. Going two and from the phase control sections are two tapers of length L_{tp}.

second tapering section the widths are changed back to their original values. The challenge now becomes to select L_1 and L_2 such that broadband coupling is achieved, which can be done by analyzing how coupling changes as the different lengths are varied. Following the work by Z. Lu et al., this can be done by expressing how the fields at the input ports 1 and 2 is related to the output ports 3 and 4 is related through a transfer matrix.

The overall transfer matrix is:

$$\begin{bmatrix} E_3 \\ E_4 \end{bmatrix} = T_c \cdot P_t \cdot P \cdot P_t^{-1} \cdot T_c \cdot \begin{bmatrix} E_1 \\ E_2 \end{bmatrix}. \tag{3.14}$$

Here E_1 and E_2 are the input fields, E_3 and E_4 are the output field, T_c is the transfer matrix for the coupling sections, P is the transfer matrix for the phase control section and P_t is the transfer matrix for the tapers. The transfer matrix for the coupling section is given by:

$$T_c = \begin{bmatrix} t & -ik \\ -ik & t \end{bmatrix} e^{-i\frac{\pi L_1}{\lambda}\left[n_{\mathrm{eff},s1}(\lambda)+n_{\mathrm{eff},s2}(\lambda)\right]}, \tag{3.15}$$

where λ is the wavelength of the field, t is coefficient for passing directly through either waveguide and k is the cross coupling coefficient.

t and k are:

$$t(L_1) = \cos\left(\frac{\pi \Delta n}{\lambda} L_1\right), \tag{3.16a}$$

$$k(L_1) = \sin\left(\frac{\pi \Delta n}{\lambda} L_1\right). \tag{3.16b}$$

The transfer matrix for the phase control section is given by:

$$P = \begin{bmatrix} e^{-i\phi_1(L_2)} & 0 \\ 0 & e^{-i\phi_2(L_2)} \end{bmatrix}, \tag{3.17}$$

where

$$\phi_1(L_2, \lambda) = \frac{2\pi L_2}{\lambda} n_{\text{eff},0} \left(w_1 - \Delta w\right), \tag{3.18a}$$

$$\phi_2(L_2, \lambda) = \frac{2\pi L_2}{\lambda} n_{\text{eff},1} \left(w_2 + \Delta w\right). \tag{3.18b}$$

Finally, the transfer matrix for the taper sections is given by:

$$P_t = \begin{bmatrix} e^{-i\theta_{t1}(L_{\text{tp}})} & 0 \\ 0 & e^{-i\theta_{t2}(L_{\text{tp}})} \end{bmatrix}, \tag{3.19}$$

where θ_{t1} and θ_{t2} are the phase shifts experienced in the tapers of waveguide 1 and waveguide 2 respectively. In the original work,[71], the waveguide loss was also included in the transfer matrices. We have not done this as the total loss over the lengths under consideration should be very small. Since linear loss does not modify the phase of the modes, the loss is of no great importance in these calculations. which is the important part here. The effective indices and phase shifts needed to calculate the transfer matrix can be obtained from simulation and the power coupled from port 1 to port 4 can be calculated by evaluating:

$$T_{14} = \frac{|E_4|^2}{|E_3|^2 + |E_4|^2}. \tag{3.20}$$

If the initial fields are a TE_1 mode with amplitude 1 at port 1 and a TE_0 mode at port 2, this will be the power coupled to the TE_0 mode at port 4. By sweeping L_1 and L_2 at the center wavelength λ_0 and calculating T_{14} a map of the power transferred to port 4, $T_{14}^{(\lambda_0)}$, can be created. In order to optimize the lengths such that the coupled power is a flat as possible over a given bandwidth $\Delta\lambda$, the maximal difference in

coupling over this bandwidth, $\Delta T_{14}^{(\Delta\lambda)}$, is also calculated for each point (L_1, L_2). Based on $T_{14}^{(\lambda_0)}$, $\Delta_{14}^{(\Delta\lambda)}$ and the desired Splitting Ratio (SR), a figure of merit for finding the optimal section lengths can be devised:

$$\text{FOM} = \left[1 - \left|T_{14}^{(\lambda_0)} - \text{SR}\right|\right]\left[1 - \Delta T_{14}^{(\Delta\lambda)}\right] \tag{3.21}$$

In the best case scenario $T_{14}^{(\lambda_0)} = \text{SR}$ and $\Delta T_{14}^{(\Delta\lambda)} = 0$ since this means that exactly the desired amount of power is transferred to port 4 at λ_0 while the coupling is flat over the range $\Delta\lambda$ in which case $\text{FOM} = 1$.

How this can be applied to optimize a 3 dB coupler (where $\text{SR} = 0.5$) is shown in fig. 3.7. This example uses the same waveguide parameters used in fig. 3.5 along with $\Delta w = 50$ nm, $L_{\text{tp}} = 1$ µm, $\lambda_0 = 1550$ nm and $\Delta\lambda = 50$ nm. As seen in fig. 3.7a, $\text{SR} = 0.5$ for a set of (L_1, L_2) values that describe an ellipse around a central set of (L_1, L_2) values. In fig. 3.7b, we see that there are few places where the broadband power variation is low and $\text{SR} = 0.5$ at the same time. The plot of the FOM in fig. 3.7c shows all the information we need to pick a set of L_1 and L_2 values, which is just chosen as the values that maximizes the FOM, for the lengths considered here is $L_{1,b} = 25.7$ µm and $L_{2,b} = 5.70$ µm. In this case, it leads to a splitting ratio of $SR = 0.5$ at λ_0, a power variation of 0.21 dB over $\Delta\lambda$ and $FOM = 0.97$. In fig. 3.8, T_{14} is plotted over the considered wavelength range as calculated using the TMM explained here. Also include are simulation results obtained using Lumerical EME[72], which provides a more accurate model of the physics involved in the situation. More detail on how these simulations are carried out will be given in chapter 4. Along with the curves describing $T_{14}(\lambda)$ the mean of T_{14} over the wavelength range is shown along with the difference between the minimum and maximum values. As we see in the figure, the power variation is slightly higher at 0.4 dB in the more accurate EME simulation, but for both the TMM case and the EME case, the power stays very close to the desired 3 dB.

Admittedly, these BMMCs with an arbitrary splitting ratio remain somewhat tangentially related to this project due to the fact that it is straightforward to design BMMCs when optimizing for $\text{SR} = 1$ with relatively standard parameters for SOI waveguides, as no phase control sections are needed in this case. Nonetheless we spent considerable time on investigating these types of MMCs and the results might prove interesting to others that have other use cases in mind.

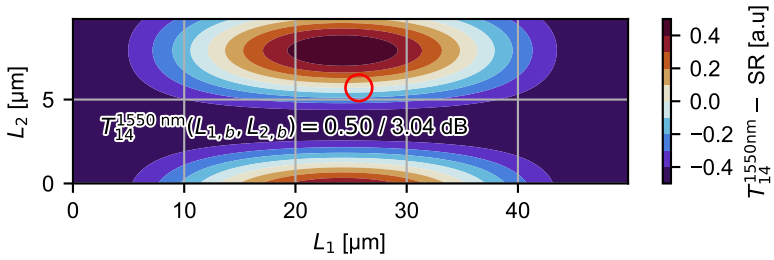

(a)

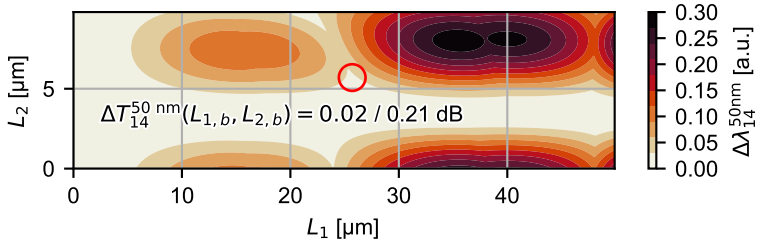

(b)

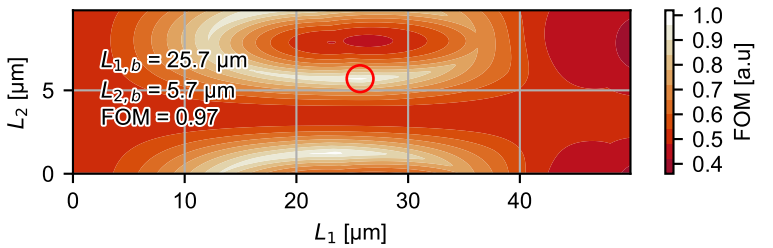

(c)

Figure 3.7: Plots of the various parameters used for choosing the best L_1 and L_2 values. for a BMMC with the same parameters as the example in fig. 3.5 and Δw =50 nm, $L_{\text{tp}} = 1$ µm and SR $= 0.5$. In all plots lighter color values signify that the parameters in question is closer to the deign goal. **(a)** Contour plot of $T_{14}^{1550\text{ nm}} -$ SR. **(b)** Contour plot of $\Delta T_{14}^{50\text{ nm}}$. **(c)** Contour plot of the FOM. The values of L_1 and L_2 that maximizes the FOM, $L_{1,b}$ and $L_{2,b}$, are shown with a red circle, here and on **(a)** and **(b)**.

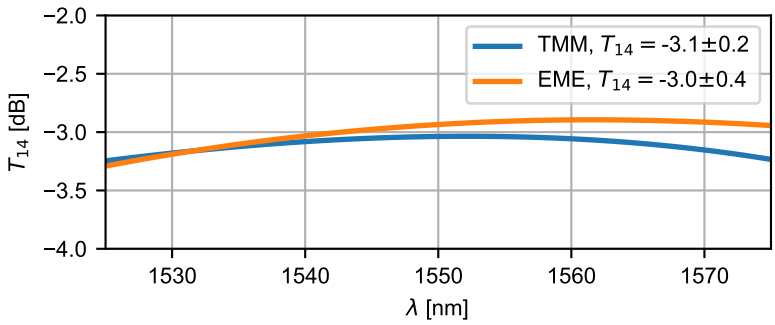

Figure 3.8: T_{14} as calculated using TMM and as simulated with EME.

4 Simulation and Design

In the following chapter I will go into detail about the methods that have been employed to simulate and design the circuits of this project. As the goal of this project has been to create complicated circuits with many elements interacting and testing out different circuit building blocks in different material platforms with varying architectures, a considerable effort has been devoted to creating a framework for simulating these devices in a way that makes switching between different platforms as simple as possible. The result of the simulations are used to design devices and get an understanding of how the device will behave in an ideal case. The simulation framework has been created as a python module which can the be accessed by an library of elements that can be used to make GDS files, which is the industry standard for defining layouts for fabrication of photonic chips. In this process, these GDS files have mostly been created using the open source python platform Nazca Design[73].

4.1 Simulation Framework

The simulation framework that has been created and which has the general structure illustrated in fig. 4.2 is based on the photonics simulation software suite provided by Ansys[72]. Mostly Ansys MODE has been employed, which provides both a Finite Difference Eigenmode (FDE) solver and an Eigenmode Expansion Method (EME) solver. In most cases, the eigenmodes of a waveguide cannot be solved for analytically and numerical methods must be applied to get important parameters such as the effective index and group index of a mode, which is what the FDE solver is employed for. FDE solvers are widely used as they are fast and converge well with known experimental and analytical results. The EME solver is a beam propagator that can be used to gain knowlegde of how modes behave as they propagate through some photonic structure. The solver functions by slicing a structure into many slices and calculating the eigenmodes of each slice. A mode can the be launched at one end of the structure and scattering matrices between each slice can be calculated. Using this, results that reach a high degree of accuracy can be obtained[74] without simulating the full dynamics of the system, which would require significantly more time and computing power. Some care does need

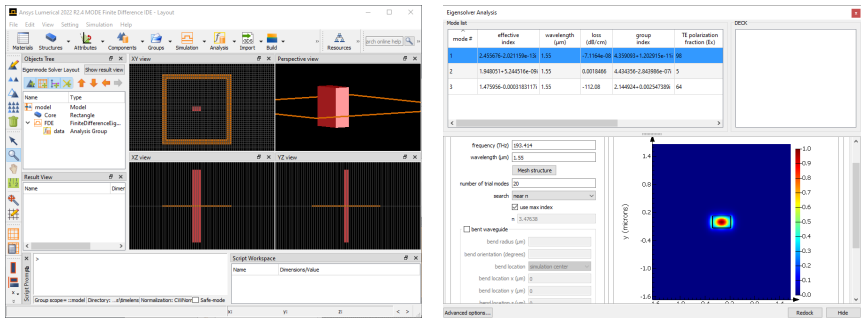

(a) (b)

Figure 4.1: **(a)** The main window of the MODE software. This is used for setting up the simulation by adding structures such as a waveguide and the type of simulation that is needed. **(b)** The FDE solver window. Here a simulation of the waveguide in **(a)** can be initialized and the properties of the found modes will be listed in the list on top.

to be taken though: in general, this method does not allow for the simulation of bent waveguide with varying radii of curvature. Ansys also supplies a Finite Difference Time Domain (FDTD) solver which does allow for simulation of the full dynamics of a system. This method relies on discretizing the Maxwell equations in time and launching some field into a system. By stepping the simulation forwards in time, the behavior of a field in a system can be simulated with no specific assumptions made except for the initial discretization of the fields[75]. This method can be extremely powerful, but it is very intensive in its requirements of RAM and CPU time. This makes it very time consuming to simulate large structures and make sure that the simulation is properly converged. Due to this, the use of FDTD simulations has been largely avoided and FDE and EME simulations have been prioritized along with other simulations based on the results of FDE simulations. For now, let us turn to how I have structured my interfacing between python and the Ansys API in order to facilitate a simple way of simulating the behavior of different devices in different platforms.

The default way of interacting with Ansys MODE/FDTD is through their respective GUIs, with an example for the MODE GUI shown in fig. 4.1a. Here geometries for simulation can be set up either by adding objects manually and changing their properties or by adding them through the scripting language that is supported by the software. In the example shown, a FDE solver region has been added

along with a Si waveguide core. The background material is set to be SiO_2, so a waveguide cladding does not have to be explicitly added to the simulation. In fig. 4.1b, the mode analysis window is shown. Here the actual simulation of the modes of the waveguide is carried out and the results are shown in the list at the top of the window along with a plot of the selected mode to the right. The most important results in our case will mostly be the effective index, the group index, the TE polarization fraction and in some cases the field distribution of the mode itself. When running EME simulations, the same GUI is used but other analysis windows are used. Here only the MODE interface is shown as the FDTD interface behaves in much the same way. I have to a large extent avoided using the GUI and instead relied on the python API, `lumapi`, to make automating the running of simulations and saving of results easier. The Ansys scripting language can be used to automate simulation to a certain degree, but setting up simulations through python offers many advantages, such as making integration with my other programming work which has been done in python much simpler and python programming being more flexible than the somewhat scripting language provided by Ansys. The python API, `lumapi`, functions by allowing the user to launch an instance of MODE in python (or other Ansys products, but from here on out I will keep the discussion to MODE since this is what has been mainly used) and storing it in an object, thus keeping the instance of MODE open as long as the python script is running. Once the solver instance has been opened, different objects can be added to the instance. If we want to find the modes of a waveguide or a system of waveguides, a FDE solver will be added to the instance and the background material in the simulation can be set as an instance variable of the FDE solver. After this one or more waveguides can be added as objects in the simulation, with the dimensions and materials of the waveguide(s) again being instance variables of the corresponding objects. Once a simulation has been set up, simulations can be run to find the parameters shown in the GUI and more. Circuit designs are then based on the results obtained from simulation or the initial results are used as the basis for further simulations. In the case of Bragg gratings for instance, the effective index of a waveguide is obtained and from the desired Bragg wavelength, the corresponding grating period is calculated. Additionally, effective index data can be used to run transfer matrix simulations of the Bragg grating. For MMCs, the effective indices of the supermodes of a waveguide system is used to calculate

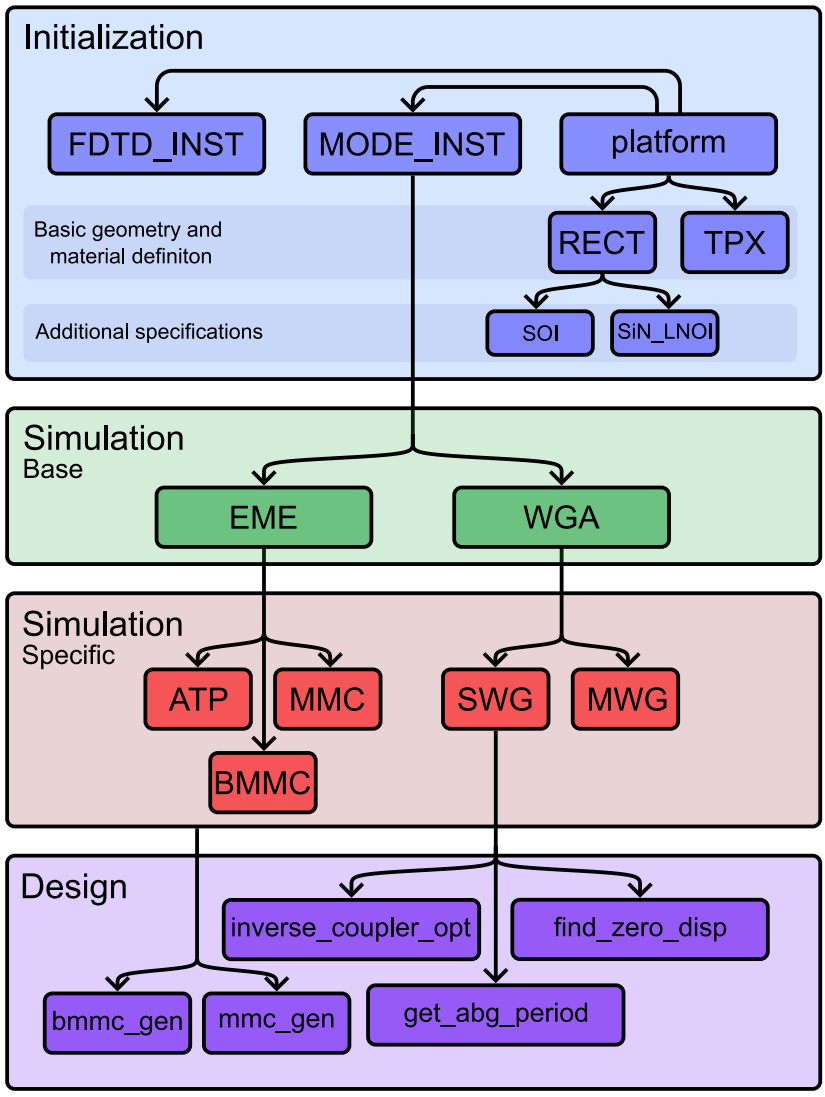

Figure 4.2: Overview of the module and class structure of the simulation framework. Classes are in upper case and functions and modules are in lower case. The direction of the arrows indicate how the classes inherit from each other. The design level is a set of functions, so strictly speaking these are not inheriting but instead using the above classes.

the coupling length and based on this, EME simulations of the system can be run to verify that the MMC exhibits the desired behavior.

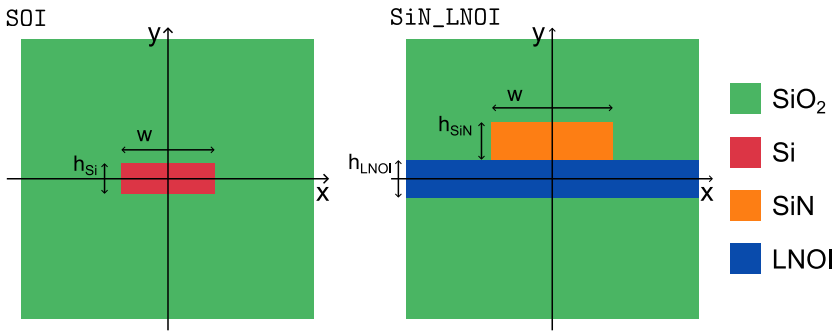

Figure 4.3: The types of waveguides added by the SOI and SiN_LNOI classes respectively.

4.1.1 Class Structure

My approach to creating a flexible framework for running otherwise identical simulations of waveguides based on different platforms is based on python modules with classes that inherit from each other in several layers as illustrated in fig. 4.2. At the top level are the classes `FDTD_INST` and `MODE_INST` that are used to launch an instance of either FDTD or MODE. These classes depend on on the module `platform`. `platform` contains the classes that allow for easily adding different photonic platforms and running simulations. As an example, let us take a look at the `RECT` class. The class contains a series of methods that adds both 2D and 3D waveguides to a simulation geometry, which will then later be used in the lower levels of the framework to set up both FDE and EME simulations. For instance the method `add_wg_2d` exists, which adds a waveguide of width w at the position x, y. The behavior of this class can then additionally be modified by subclasses. In the case of `RECT`, the subclasses `SOI` and `SiN_LNOI` exist for simulation of SOI waveguides and SiN on LNOI waveguides. Both of these platforms use a rectangular waveguide geometries, so the methods for setting up waveguides can be shared between them. If `SOI` is used, a simulation with SiO_2 as the background material is set up and waveguides will by default be added as a rectangle of Si to the center of the simulation. If `SiN_LNOI` is used instead, an additional layer of LNOI is added to the simulation where the direction of the crystal axes can be specified. When a waveguide is added, `add_wg_2d` is modified such that it is added as a rectangle of SiN sitting on top of the LNOI layer. These two waveguide geometries and how they are added to a simulation is showed in fig. 4.3

At the time of writing the RECT class along with its subclasses and TPX has been introduced. TPX is used for LioniX Triplex waveguides with the default values describing their standard asymmetric double stripe geometry, but other double stripe waveguides can be simulated by changing these values. In addition to specifying how waveguides should be added in 2D/3D, methods for manually adding regions with higher simulation resolution are also implemented, along with methods for adding asymmetric tapers and polygonal waveguide with an arbitrary shape. Finally these classes specify default values for the size of the simulation region, the overall simulation resolution and the height of the different material layers. The default size and resolution is determined by convergence sweeps of these parameters and must be determined individually for each platform.

Once a platform has been defined, an instance of MODE_INST can be created, which takes the required arguments base_dims and platform. If the platform is SOI, base_dims, the base dimensions, will be the height of the Si layer. For SiN_LNOI these will be both the height of the SiN and LNOI layers. For TPX, base_dims are the height of the individual layers of SiN, the internal distance between the two layers and the etching angle of the SiN. Upon creation of an instance, the methods mentioned in the above are inherited by MODE_INST based on the choice of platform along with defining the overall simulation parameters. A folder for saving data with a name corresponding to the platform and the base dimensions is also created. As the name indicates, MODE_INST first and foremost contains a method for launching an instance of MODE. If an instance of MODE is launched, the first step taken is to define the materials that will be used in the simulation. MODE has a list of materials with effective index data for a range of wavelengths. Using this data, polynomial fits can be carried out which allows for accurate wavelength dependent modeling of the behavior of light over a range of wavelengths. For the materials where this data is available, these fits are carried out (by default over the range of 1.4-1.7 μm) and these material fits are saved. If LNOI is used, a new material is added and the effective index along the individual crystal axes are specified. MODE_INST also contains the method general_setup which launches the MODE instance and adds a FDE or EME solver based on what is required. The created solver will have the dimensions specified by the chosen platform. For FDE solvers, the boundaries are set as PML. This results in a slight increase of runtime for the simulations but has the benefit of removing

spurious modes when finding modes. If metal boundaries are chosen, spurious, non-propagating modes are often found when solving due to interaction with the boundaries and these can be tricky to exclude without direct inspection of the results. For EME where only specific desired modes are launched into the simulation region, the boundaries are kept as metal, which means that care has to be taken to make sure that the simulation region is large enough to avoid boundary reflections (although care also has to be taken if PML boundaries are used as these absorb energy from the propagating mode if the evanescent field overlaps with the boundary).

In the next level of the framework we have `EME` and `WGA` which are used for running EME and FDE simulations (WGA for waveguide analysis). The `WGA` and its subclasses allows for easy simulations of the modes of a waveguide by specifying the dimensions of the waveguide using the `SWG` class, or the modes of a system of two waveguides by specifying the waveguide dimensions and the gap between the waveguides using the `MWG` class, with any type of waveguide being easy to simulate as long as the corresponding `platform` class has been properly defined. An array of methods have been defined for these classes that makes it easy to find for instance the dispersion of a waveguide as a function of waveguide width, the effective mode area of a mode in a waveguide, the period of an ABG based on the desired Bragg wavelength or the mode overlap between an integrated waveguide and a free space Gaussian mode. The `EME` class allows for simulation of the propagating through a waveguide. This is used for the design of BMMCs where the phase shift due to propagating through an asymmetric taper can be calculated. It is also used to simulate MMCs and BMMCs to check if the simulated coupling aligns with that found from TMM and can be used to simulate unchirped, unapodized ABGs.

4.1.2 Transfer Matrix Simulations

As described in section 2.1.2, a TMM model is a valuable tool to simulate BGs, as it can be used to simulate BGs with an arbitrary apodization and chirp profile, with the examples shown in that section created using the implementation of a TMM model which will be outlined here. This implementation finds the effective of the TE_0 mode at different waveguide widths, using the methods supplied by the `SWG` method. As an example, let us consider a grating in 250 nm tall SOI with a $L = 5$ µm, $w = 800$ nm, $\Delta w = 100$ nm and $\lambda_B = 1550$ nm and a tanh

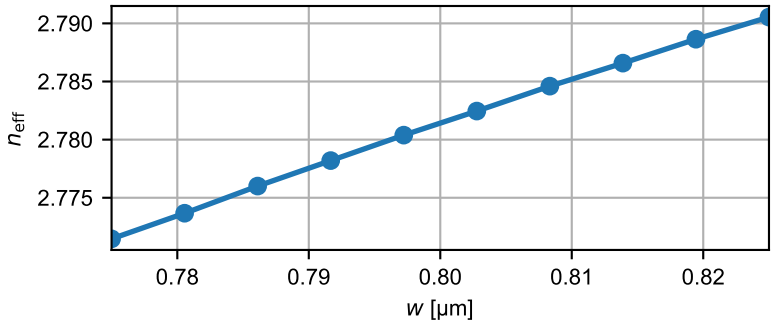

Figure 4.4: Effective index as a function of width of a 250 nm tall waveguide.

apodization profile with $\alpha = 3$ and $\beta = 1.5$. In this case, the effective indices as a function of width are displayed in fig. 4.4 Based on the effective index at w, the grating period is found to be $\Lambda = 278$ nm. In this case for an unchirped grating, the waveguide width is:

$$w(x) = w + A(x)\frac{\Delta w}{2}\sin\left(\frac{2\pi x}{\Lambda}\right), \tag{4.1}$$

where A is the apodization profile. This is for the case where the corrugations evenly change the width around the w. Alternatively, simulations can be run with corrugations that only increase the waveguide width relative to w, in which case the waveguide width is:

$$w(x) = w + A(x)\Delta w\left[\frac{1}{2} + \frac{1}{2}\sin\left(\frac{2\pi x}{\Lambda}\right)\right] \tag{4.2}$$

In the case of even corrugations, the waveguide width is shown in fig. 4.5. The geometry shown here is calculated using a step size Δx that fulfills $\Delta x \ll \Lambda$, such that the grating shape is properly resolved. In order to simulate the response of gratings fabricated with different fabrication resolutions the TMM has been implemented such that the grating shape is first calculated using the step size Δx and then long pass filtered with the corner frequency Δx_{geom}. If δx_{geom} is 200 nm, which is on the same order of magnitude as Λ, this results in the two gratings shapes shown in fig. 4.6. The resulting shape is not necessarily the shape that would result from a large fabrication resolution, but we believe that it is useful to some degree in investigating the effects that would result from this. One aspect that is captured to some degree by this, is that Δw is lowered if the period is smaller

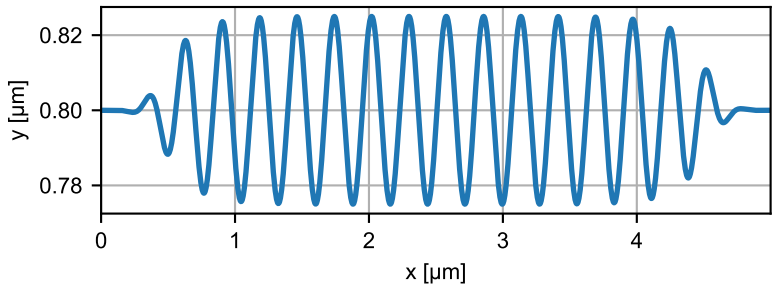

Figure 4.5: Width of a BG along the length of the grating.

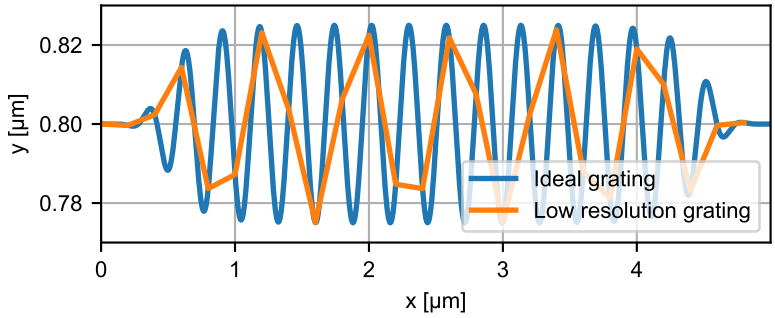

Figure 4.6: Comparison between an ideal grating and one corresponding to a fabrication resolution of 200 nm.

than the fabrication resolution, which is a realistic consequence. In this plot, only a few periods are shown, but for a long grating one would expect Δw to be reduced on average. One thing that is not captured by this is that change in height of the throughs and peaks of the waveguide corrugation might not be impacted in the same way. In the throughs of the corrugation, the waveguide walls are very close to each other, which might be under-etched compared to the peaks where the waveguide walls are further apart. This would also lead to an average change in waveguide width which this framework does not capture. The shape after long pass filtering is the one that is used to run the simulation, but if δx_{geom} is small, this is the same as the original shape. When used in simulation, the shape is linearly interpolated and sampled at the resolution δx_{sim} and the width of each simulation point is mapped to an effective index using the data for the effective

index as a function of the width. The transfer matrix of the system can then be calculated using eqs. (2.32) to (2.38), where $\delta x = \delta x_{\text{sim}}$. A simulation of the transfer matrix as a function of wavelength can at this point be launched, with the transfer matrix calculated within a desired wavelength range with the desired resolution in wavelength.

In the case of chirped gratings, the procedure is slightly different in the initial calculation of the waveguide width. In order for the generated dispersion to be linear, the phase of the grating should be parabolic in such a way that the derivative of it results in the desired chirp. This is achieved by calculating the two spatial frequencies

$$f_{\text{i}} = \frac{1}{\Lambda_0} \qquad \text{and} \tag{4.3}$$

$$f_{\text{f}} = \frac{1}{\Lambda_0 + \Delta\Lambda}, \tag{4.4}$$

where Λ_0 is the initial grating period and $\Delta\Lambda$ is the change in grating period over the length of the grating. The grating phase is then:

$$\phi(x) = 2\pi \frac{\Delta f}{2L} x^2 + 2\pi f_{\text{i}} x, \tag{4.5}$$

where $\Delta f = f_{\text{f}} - f_{\text{i}}$ and the waveguide width is:

$$w(x) = w + A(x) \frac{\Delta w}{2} \sin\left[\phi(x)\right], \tag{4.6}$$

which as in the unchirped case can be modified to allow for a positive instead of an even corrugation profile. In the case of chirped BGs where part of the goal of the simulation often will be to investigate how the phase, and thus the group delay, inside the reflection band evolves, the spacing of wavelength points in this region is parabolically distributed, with the spacing decreasing in the direction of the chirp. If the difference in phase between two consecutive points is more than 2π, it cannot be properly unwrapped leading to discontinuities. This means that if we were using an even spacing of, the spacing must be much finer in order to avoid phase discontinuities than if using parabolically spaced points.

4.2 Layout Design

The design of photonic chips on different platforms has been done using Nazca design[73], which is a python library for defining chip layouts and exporting them to the widely used GDSII format, which is

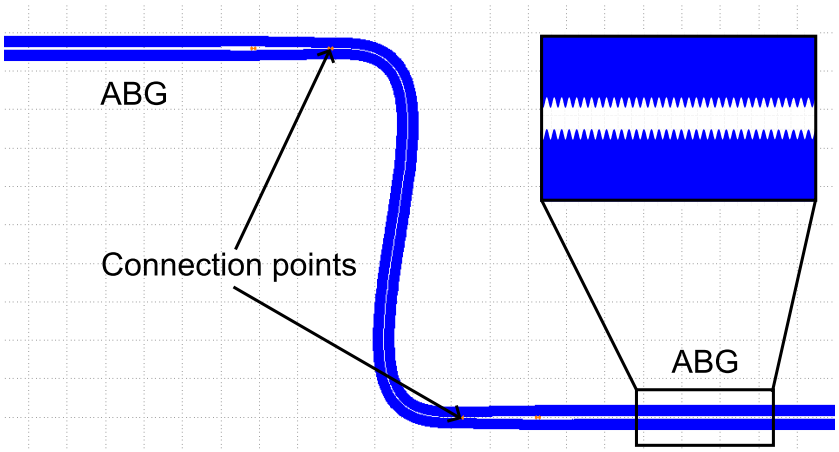

Figure 4.7: Image of a section of a CBBG shown in a program for viewing GDS files.

used in fabrication of photonic chips. Nazca design allows one to create cells which have defined input and output points, which can then be connected automatically with different types of waveguides. This can for instance be a straight waveguide, but also be something more complex. A very useful tool in our case has been connections that have a continuously changing radius of curvature, that snap to specified input and output points. These types of waveguides helps avoid reflections from waveguide bends by having no discontinuities in their effective index, which is useful in circuits such as CBBGs. As an example of how this framework functions, a section of a CBBG is shown in fig. 4.7. The way this (part of a) circuit is created is by defining an ABG based on the desired physical parameters. A polygon that describes the waveguide can be defined as a cell in Nazca design and several instances of this cell can be placed in the layout. Tapered waveguides are then appended to these ABGs to take the waveguide width from the multi mode width to the single mode width and the bent interconnects are added to connect each individual ABG with the next. This method of placing and connecting elements in a layout makes it simple to create relatively complex circuits.

In order to facilitate the design of circuits in different platforms, we have developed a python library for creating a host of different circuit elements. This module interacts with the simulation framework described in section 4.1 in the way sketched in fig. 4.8. This shows how

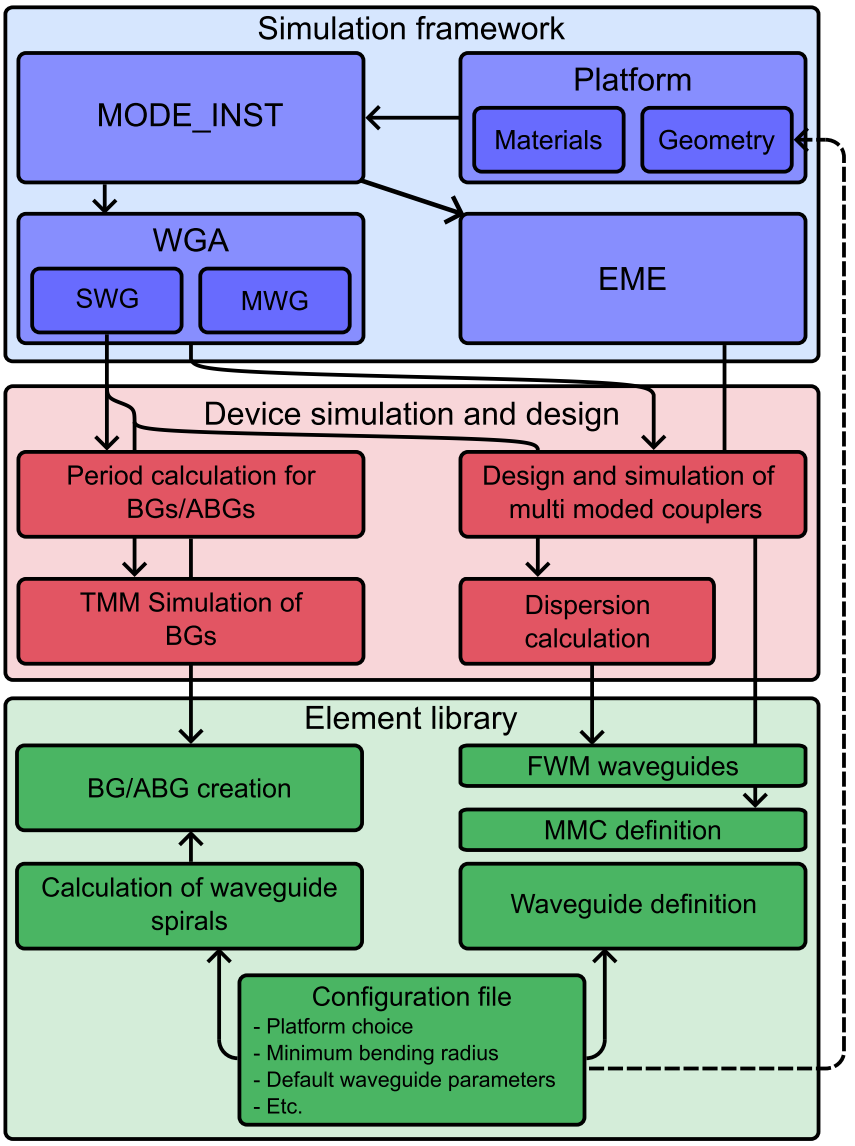

Figure 4.8: Schematic overview of interaction between the tools that have been created for simulating devices and creating layouts for photonic chips.

the simulation framework is used to simulate different different physical parameters that are used in the design of a element, such as the effective indices for a BG or an ABG and how it can also be used to run simulations of the elements that are being implemented, such as running a TMM simulation of a BG, which is the first and second level

in the figure. In the lower level data obtained from the simulations are used to generate the layout using the python library of different elements, which calculates the shape of it and connects it to different elements. The element library needs a configuration file for each project it is used with. This configuration file defines many different parameters such as the default waveguide width, the minimum acceptable bending radius for a bent waveguide, the cladding width of waveguides and more. Importantly, it also specifies the platform used for the chip in question such that all simulations are run for the correct type of waveguide, which makes it easy to use any created element on different platforms.

The main components that exist in this library are MMCs, BMMCs, linear BGs and ABGs, inverse taper couplers, routines for designing FWM waveguides and waveguide spirals with a continuously varying radius of curvature. The design of the first four of these should be clear from chapter 2, but we will devote some space to discussing the design and utility of the others here.

4.2.1 Inverse Taper Couplers

Inverse taper couplers are a very efficient way of coupling light to and from a PIC when using edge coupling. With edge coupling, lensed optical fibers are brought very close to the edge of a chip and using the lens, the output of the fiber can be brought to its focal point just at the interface between the air and a PIC on the chip. In order to efficiently couple to a waveguide on the chip, the mode profile of this mode must overlap as well as possible with the mode of the light from the lensed fiber. Even using a lens, this will in general be much larger than the waveguide mode, but by tapering the waveguide down to a very narrow width, the two modes can reach a very large overlap. This is due to the fact that if a waveguide becomes narrow enough, the TE_0 mode of the waveguide stops being tightly confined inside the waveguide, with most of the field instead existing in the cladding of the waveguide. The overlap with a fiber mode with a rotationally symmetric profile will of course never be complete, but good coupling can be achieved. In fig. 4.9a, the power coupling from a waveguide mode of a waveguide with varying widths and a height of 250 nm to a Gaussian mode with mode field diameter (MFD) of 3.6 µm is shown. The best coupling occurs at a waveguide width of 156 nm where the power coupling is $P_c = 0.88$ or -0.53 dB in logarithmic units. In this simulations, a MFD 3.6 µm was chosen since this is

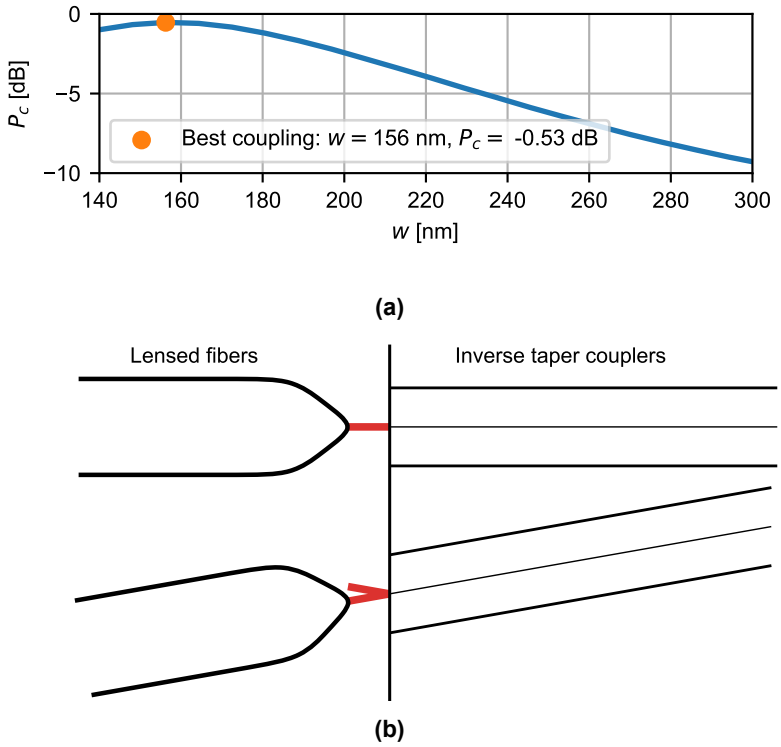

Figure 4.9: **(a)** The power coupling from a Gaussian mode with a MFD of 3.6 µm and a waveguide mode for varying waveguide widths and a height of 250 nm. The best overlap is at a width of 156 nm, where the coupling is -0.5 dB. **(b)** Illustration of how light can couple back into the lensed fiber if the inverse taper coupler is not angled.

the MFD at the focal point of the lensed fibers we typically employ in our laboratory. This can of course be changed if desired. The results shown here are for a 250 nm tall waveguide in SOI and we see that the best coupling is achieved with a waveguide width of 158 nm, where the power coupling is 89%. The rest of this power will either couple into the cladding or be reflected back towards the lensed fiber. To avoid that this light which is reflected directly from the edge of the chip couples back into the lensed fiber, the the coupler can be angled as illustrated in fig. 4.9b. When using the element library the first time for a platform, this simulation is automatically run and the results saved.

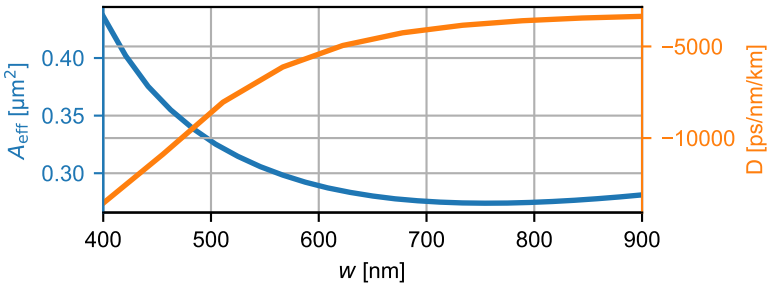

Figure 4.10: A_{eff} and dispersion for a waveguide in a 100 nm SOI waveguide at 1500 nm. A_{eff} is shown on the left axis and in blue while the dispersion is shown on the right in orange.

4.2.2 Optimization of FWM Waveguides

Since a FWM waveguide in principle can be based on any waveguide geometry, there is no dedicated tool for design of these, but as we saw in section 2.3, two important aspects of a FWM process is the CE and the bandwidth. The CE depends on both the strength of the nonlinearity of the material and A_{eff} of the waveguide mode in the process, while the bandwidth depends on the dispersion of the waveguide. With simple rectangular waveguides, the only way we can control A_{eff} and dispersion is through changing the waveguide dimensions. Typically, the waveguide height will be predetermined so all we have left is the waveguide width. Functions for finding both A_{eff} and the dispersion of a waveguide as a function of width for a given height is included, which aids in the choice of width for a FWM waveguide. As an example see fig. 4.10 where A_{eff} and the dispersion of a 100 nm tall SOI waveguide is shown for a range of widths. As we see, we cannot achieve zero dispersion for this waveguide height which would be optimal for FWM. Under these conditions we would instead choose the waveguide width based on minimizing A_{eff} which will lead to a large CE, which means choosing a waveguide width of 750 nm. This is also acceptable in terms of dispersion since this is at least on the lower end on the magnitude of dispersion that can be achieved with this waveguide height.

4.2.3 Spiral Design

Since BGs need to be quite long in order to achieve any meaningful dispersion, they need to be folded in some way such that they can fit on a chip first of all. For e-beam fabrication where etching takes

place inside different write fields that in our case are 500x500 µm, a long waveguide has the tighter constraint that it needs to be folded in an efficient way that fits inside this area. For a BG, it is important that this is done in a way that does not lead to any sudden jumps in the refractive index, for instance due to a change in the radius of curvature of the waveguide. Due to this, the CBGs that we have implemented, along with our FWM waveguides have been based on a spiral design. The original design is by A. D. Simard et al.[76], with spirals where the center of the spiral shape is shifted in a way that leads to a continually changing radius of curvature while changing the direction of rotation. This leads to no sudden changes in effective refractive index, which could lead to cavities inside the grating that generate spikes in the reflection and dispersion of the signal. In their work the spiral is defined by the function:

$$S(\rho) = R(\rho)e^{i|\rho|} - \Delta x(\rho), \tag{4.7}$$

where

$$R(\rho) = R_0\,\mathrm{sgn}(\rho) + \Delta R\rho/\pi, \tag{4.8}$$

$$\Delta x(\rho) = R_0\,\mathrm{sgn}(\rho)e^{-|\rho|/\alpha}. \tag{4.9}$$

In this parametrization the real and imaginary part of S corresponds to the x and y-values of the spiral. R_0 controls the minimum radius of curvature of the spiral, α controls how fast the shift in center of rotation happens and ΔR is the distance between points a full rotation apart. One complication is that the value of α influences the both the actual minimum radius of curvature, R_{min}, and the distance between points a full rotation apart close to the center of the spiral as illustrated in fig. 4.11. Reducing α makes the shift in center of rotation take place more suddenly which in turn reduces R_{min}. This is important, since we do not want to go below certain threshold R_{min}'s when design PICs. For $R_0/\Delta R = 1$, this is not a great issue as α can be increased without leading to other issues. As $R_0/\Delta R$ becomes larger than 1, choosing α and R_0 can become more challenging as a value of α that leads to an acceptable R_{min} can lead to the spiral overlapping with itself, which is also unacceptable. Generally we want ΔR to be as small as possible (with the limiting factor being the minimum waveguide distance) as this leads to a smaller device footprint. This means that R_0 and α need to be chosen on a case by case basis in order to ensure that parts of the spiral does not get too close to itself

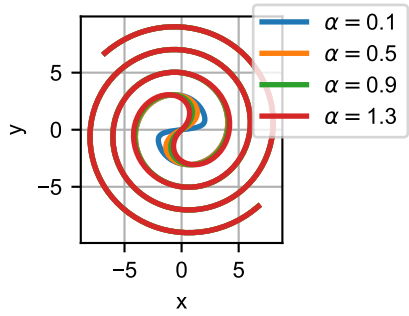

(a)

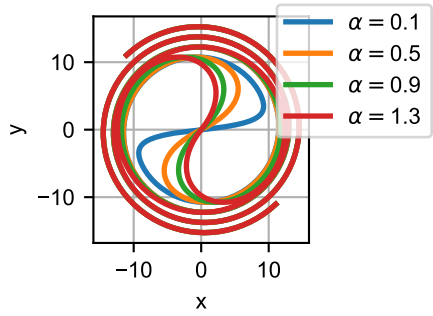

(b)

Figure 4.11: Spirals for varying values of α. In **(a)** R_0 =2 and ΔR =2. In **(b)** R_0 =15 and ΔR =1.5.

while also keeping R_{min} above a threshold value. This is generally harder for lower index contrast platforms since the acceptable radius of curvature is higher here than for high index platforms leading to larger $R_0/\Delta R$. This means that a larger R_0 must be chosen, which leads to a larger footprint, but it must be noted that the longer the waveguide is, the smaller the relative impact of this is.

In order to couple light from the waveguide using this design, a straight waveguide must be appended to the outer ends of the spiral. This means that a jump in the effective index will happen here, since a change in the radius of curvature of the waveguide takes place here. To circumvent this, we modified the spiral design based on the follow-

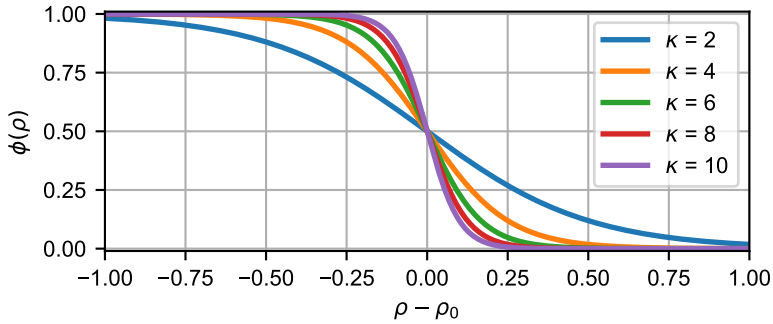

Figure 4.12: Example of the activation function $f(\rho)$ for different values of κ

ing. If we write the x and y-coordinates of the spiral as:

$$\begin{bmatrix} x(\rho) \\ y(\rho) \end{bmatrix} = \begin{bmatrix} \mathfrak{Re}\{S(\rho)\} \\ \mathfrak{Im}\{S(\phi)\} \end{bmatrix} \tag{4.10}$$

$$\Rightarrow \begin{bmatrix} x(\rho) \\ y(\rho) \end{bmatrix} = \begin{bmatrix} R(\rho)\cos(\rho) - \Delta x(\rho) \\ R(\rho)\sin(\rho) \end{bmatrix}, \tag{4.11}$$

and introduce a coordinate transform for the y-coordinate that makes sure that this value stops changing after a certain ρ value, we get a waveguide spirals out and then becomes horizontal. We will call this new coordinate $\phi(\rho)$. In order for it to stop changing after a certain value, we can require that its derivative with respect to ρ is a hyperbolic tangent:

$$\frac{d\phi}{d\rho} = \frac{1}{2} - \frac{1}{2}\tanh[\kappa(\rho - \rho_0)], \tag{4.12}$$

where κ controls how fast the derivative goes to zero and ρ_0 is the threshold value. This function is plotted in fig. 4.12, to illustrate how κ changes the speed of the change. From eq. (4.12), we can find ϕ as:

$$\phi(\rho) = \int_0^{\rho} \left\{ \frac{1}{2} - \frac{1}{2}\tanh[\kappa(\rho - \rho_0)]d\rho' \right\} \tag{4.13}$$

$$= \frac{1}{2}\rho - \frac{1}{2\kappa}\ln\left(\cosh[\kappa(\rho - \rho_0)]\right) + \frac{1}{2\kappa}\ln\left(\cosh[\kappa\rho_0]\right), \tag{4.14}$$

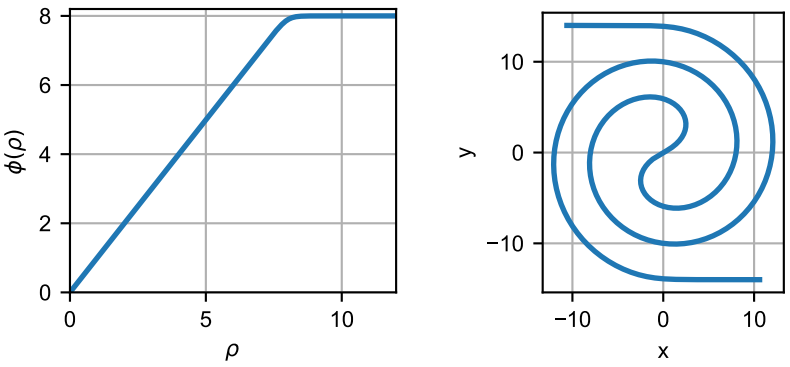

(a) **(b)**

Figure 4.13: **(a)** $\phi(\rho)$ for $\rho_0 = 8$ and $\kappa = 3$. **(b)** A spiral with a continuously changing radius of curvature calculated using the coordinate transform.

and we can rewrite the spiral coordinates as:

$$\begin{bmatrix} x(\rho) \\ y(\rho) \end{bmatrix} = \begin{bmatrix} R(\rho)\cos(\rho) - \Delta x(\rho) \\ R(\phi[\rho])\sin(\phi[\rho]) \end{bmatrix}. \tag{4.15}$$

In fig. 4.13a, $\phi(\rho)$ for $\rho_0 = 8$ and $\kappa = 3$ is shown and we see that is has exactly the intended behavior. A spiral created using this ϕ is shown in fig. 4.13b and again we see that the spiral arms stop spiraling and go horizontal after a few rotations.

With this, we have a way of implementing a spiral where the radius of curvature is always continuously changing. In order to utilize this, we need to be able to define a waveguide using the base spiral shape. This can be done by calculating the unit normal vector, $\hat{\mathbf{N}}(\rho)$, for each point on the spiral. This is just a 90° degree rotation of the unit tangent, $\hat{\mathbf{T}}(\rho)$, which is defined as:

$$\hat{\mathbf{T}}(\rho) = \frac{d\mathbf{S}/d\rho}{|d\mathbf{S}/d\rho|} \tag{4.16}$$

$$= \frac{\frac{dx}{d\rho}\hat{\mathbf{x}} + \frac{dy}{d\rho}\hat{\mathbf{y}}}{\sqrt{\left(\frac{dx}{d\rho}\right)^2 + \left(\frac{dy}{d\rho}\right)^2}} \tag{4.17}$$

where **S** is the vector defining the spiral:

$$\mathbf{S}(\rho) = \begin{bmatrix} x(\rho) \\ y(\phi[\rho]). \end{bmatrix} \tag{4.18}$$

In order to calculate the tangent, we find $dx/d\rho$ and $dy/d\rho$. Starting with the x-term gives us:

$$\begin{aligned} \frac{dx}{d\rho} &= \frac{d}{d\rho}\left[R(\rho)\cos(\rho) - \Delta x(\rho)\right] \\ &= \frac{dR}{d\rho}\cos(\rho) - R(\rho)\sin(\rho) - \frac{d\Delta x}{d\rho}. \end{aligned} \tag{4.19}$$

Using the definitions of R and Δx in eqs. (4.8) and (4.9) and, we find:

$$\frac{dx}{d\rho} = \frac{\Delta R}{\pi}\cos(\rho) - R(\rho)\sin(\rho) + \frac{\Delta x(\rho)}{\alpha}. \tag{4.20}$$

Likewise, for the y-term we find:

$$\begin{aligned} \frac{dy}{d\rho} &= \frac{dR}{d\phi}\frac{d\phi}{d\rho}\sin(\phi) + R(\phi)\frac{d}{d\rho}\sin(\phi) \\ &= \frac{\Delta R}{\pi}\frac{d\phi}{d\rho}\sin(\phi) + R(\phi)\cos(\phi)\frac{d\phi}{d\rho}. \end{aligned} \tag{4.21}$$

Since we defined $d\phi/d\rho$ in eq. (4.12), this is easily found and from this $\hat{\mathbf{T}}(\rho)$. Finally, from this we have the unit tangent:

$$\hat{\mathbf{N}}(\rho) = \begin{pmatrix} -T_y \\ T_x \end{pmatrix}. \tag{4.22}$$

Creating a waveguide of width w is then simple, since the unit normal always is perpendicular to the spiral. Due to this the waveguide walls can simply be calculated as:

$$\mathbf{S}_{wg,\pm}(\rho) = \mathbf{S}(\rho) \pm \frac{w}{2}\hat{\mathbf{N}}(\rho). \tag{4.23}$$

In fig. 4.14a a plot of $\mathbf{S}(\rho)$ and the corresponding $\mathbf{N}(\rho)$ is shown, and the waveguide walls of a waveguide created using these is shown in fig. 4.14b. Equivalently, a Spiral Bragg Grating (SBG) or a Spiral Chirped Bragg Grating (SCBG) can be created by calculating the waveguide walls of a linear BG, y_{gt}, and then mapping these to the spiral using:

$$\mathbf{S}_{bg,\pm}(\rho) = \mathbf{S}(\rho) \pm y_{\text{gt}}(\rho)\hat{\mathbf{N}}(\rho). \tag{4.24}$$

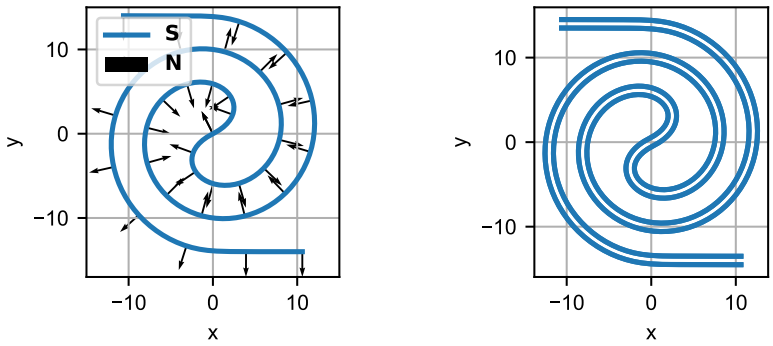

Figure 4.14: (a) $\mathbf{S}(\rho)$ and corresponding $\mathbf{N}(\rho)$. **(b)** The waveguide walls of a spiral waveguide created using the results illustrated in **(a).**

This can also be used to create a Spiral Asymmetric Bragg Grating (SABG) or a Spiral Chirped Asymmetric Bragg Grating (SCABG). In this case the upper and lower waveguide walls should be defined separately, such that the relative phase of the waveguide walls is correct.

A sticking point here is that we must find some mapping from that takes us from $y_{\text{gt}}(x)$ to $y_{\text{gt}}(\rho)$. In practice this means that mapping either a waveguide or a BG to a spiral is a more complex process than just calculating the spiral shape, since we typically desire for all the points of the waveguide walls to have a uniform distance between them. That is, we want the waveguide to be defined with a specific resolution, δx. Our approach to this is to calculate a linear BG, defined by a set of coordinates x_{gt}, y_{gt}, with a uniform step size, Δx, in linear space. When calculating a spiral based on the angle ρ, the distance between individual points increase with ρ. If a grating is mapped to a spiral without this in mind, the grating period will be stretched and compressed in different points of the spiral, destroying the grating design. Due to this a set of ρ's that leads to a spiral where

$$\Delta s = \Delta s_i(\rho_i) = \sqrt{(x_i - x_{i-1})^2 + (y_i - y_{i-1})^2} \tag{4.25}$$

$$= \Delta x, \tag{4.26}$$

is needed. That is, the distance between each consecutive spiral coordinate needs to be a constant, Δs, which is equal to Δx. Possibly, this can be done using some clever conformal mapping, but we are

not experts in this. Instead this is done numerically with an algorithm which calculates a spiral of length L, where the desired Δs and a precision, p, is set. The points of the spiral are then calculated consecutively from the center of the spiral to the end of the spiral using a simple gradient descent algorithm that varies ρ, until a value of ρ is found ensures that the distance each consecutive point on the spiral is:

$$\Delta s_{act} = \Delta s \pm \frac{\Delta s \cdot p}{2} \tag{4.27}$$

Additionally, this algorithm ensures that the desired length of the spiral at each step, L_i, also falls within the same bounds:

$$L_{i,\text{act}} = L_i \pm \frac{\Delta s \cdot p}{2}. \tag{4.28}$$

Using this, a grating or waveguide can be mapped directly to a spiral now that the values of ρ and x correspond to the same step distance. Typically $\Delta s = 1$ nm and $p = 10^{-5}$, but that can of course be varied based on the particular needs of the design.

As noted above, the value of α influences R_{min}. If a the radius of curvature of a waveguide gets too small, this leads to large waveguide losses. It also changes the effective index of the mode, which will lead to shifts in λ_B for a BG, so in order to be sure that the created spiral waveguides stay above some threshold radius of curvature, the radius of curvature of the spiral, R_c, must be calculated. This can be expressed as a combination of different derivatives of the coordinates:

$$R_c = \frac{\left[\left(\frac{dx}{d\rho}\right)^2 + \left(\frac{dy}{d\rho}\right)^2\right]^{\frac{3}{2}}}{\frac{dx}{d\rho}\frac{d^2y}{d\rho^2} - \frac{dy}{d\rho}\frac{d^2x}{d\rho^2}}. \tag{4.29}$$

The first order derivatives were found above in eqs. (4.20) and (4.21), so only the second order derivatives need to be found. Starting with the x-derivative we have

$$\frac{d^2x}{d\rho^2} = -\frac{2\Delta x}{\pi}\sin(\rho) - R(\rho)\cos(\rho) - \frac{\Delta x(\rho)}{\alpha^2}. \tag{4.30}$$

For the y derivative we have:

$$\begin{aligned}\frac{d^2y}{d\rho^2} = \frac{\Delta R}{\pi}\left[\frac{d^2\phi}{d\rho^2}\sin(\phi) + 2\left(\frac{d\phi}{d\rho}\right)^2\cos(\phi)\right] \\ + R(\phi)\left[\frac{d^2\phi}{d\rho^2}\cos(\phi) - \left(\frac{d\phi}{d\rho}\right)^2\sin(\phi)\right],\end{aligned} \tag{4.31}$$

where

$$\frac{d^2\phi}{d\rho^2} = -\frac{1}{2}\kappa\,\mathrm{sech}^2\left[\kappa(\rho-\rho_0)\right]. \tag{4.32}$$

Plots of the radius of curvature of spirals for the same parameters as used in fig. 4.11 are shown in fig. 4.15. R_0 is shown in the plot, clearly illustrating that the actual radius of curvature goes below R_0, with smaller α and larger R_0 leading to a larger undershot, demonstrating in a more rigorous way that this is something to be aware of when designing these spiral waveguides. Not clear from the figure is that $R_c(0) = \infty$ for all values of α, but this should make sense intuitively. Importantly, this shows that the radius of curvature is continuous for all values of ρ. When using this in the element library, a minimum allowed radius of curvature for spirals is defined and the user will be warned if the spiral curvature goes below this value.

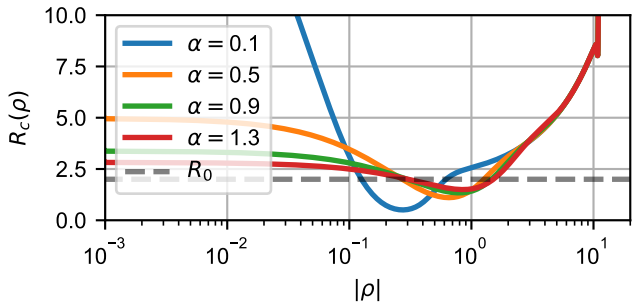

(a)

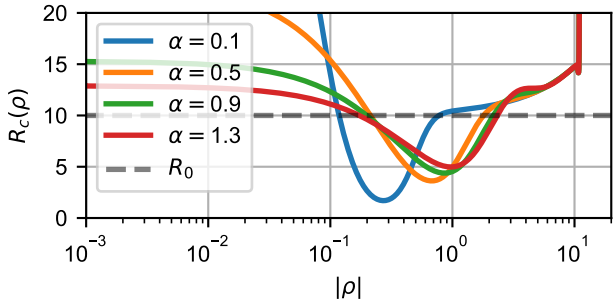

(b)

Figure 4.15: R_c for the spirals shown in fig. 4.11 which had varying values of α. Here $\kappa = 6$. In **(a)** $R_0 = 2$ and $\Delta R = 2$ and in **(b)** $R_0 = 15$ and $\Delta R = 1.5$

5 Experimental Demonstrations

This chapter concerns the circuits that have been implemented over the course of this PhD, the design of which was discussed in chapter 4. The chapter is divided into sections concerning the different chips that were fabricated. The first section concerns a chip that was fabricated using the thin silicon platform discussed in section 5.1 both as a test of this general idea and more generally as a way to learn about spiral BGs and CBBGs. The second section concerns the testing of circuits for low loss access to the reflection from ABGs using MMCs, discussed in section 3.2, which was implemented in a SiN on LNOI platform. The final section concerns the implementation of larger circuits combining dispersion generating SBGs, FWM waveguides and CBBGs in a more standard SOI platform with 250 nm silicon.

5.1 Thin Si Circuits

This chip, which was fabricated on a 100 nm Si wafer by SiPhotonIC, had a multitude of goals. We wanted to investigate the viability of thin Si circuits, get practical experience with the design of CSBGs, test our own CBBGs and carry out wavelength conversion experiments using FWM with a CBBG as an on chip power filter with the overarching theme of testing these devices in thin Si. Let us first turn to the performance of the CSBGs.

5.1.1 Chirped Spiral Bragg Gratings

An important aspect to to investigate is how the performance of linear CBGs and otherwise identical spiral CBGs compared in performance. In fig. 5.1, comparisons between two sets of gratings with parameters listed in table 5.1 are shown along with results obtained from simulation for these gratings, with the only difference between the two sets being Δw, which also makes it useful for comparing the effect of varying this parameter. One thing is common for the four grating

Figure	L [µm]	w [nm]	Δw [nm]	$\lambda_{B,0}$ [nm]	$\Delta\lambda$ [nm]	α	β
fig. 5.1a	2800	680	20	1540	20	3	1.5
fig. 5.1b	2800	680	50	1540	20	3	1.5

Table 5.1: Grating parameters for the CBGs and SCBGs shown in fig. 5.1.

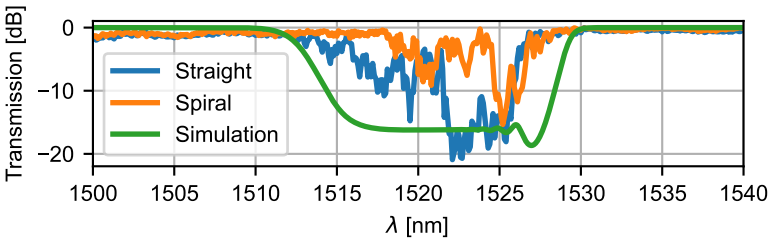

(a)

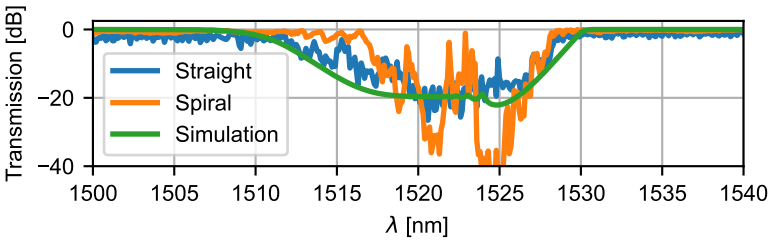

(b)

Figure 5.1: Measured and simulated response for straight and spiral CBGs for the grating design parameters in fig. 5.1. In both **(a)** and **(b)** the simulated response has been shifted to align with the observed responses. In **b**, the simulated response has been scaled to align better with the response of the straight CBG.

responses: the grating response is shifted relative to the design response by approximately 30 nm, the causes of which we will analyze further in section section 5.3.1, after presenting further experimental results. In fig. 5.1a the insertion loss (IL) was was 7.77 dB and 6.42 dB for the straight and spiral CBG respectively. For both the grating response is narrower than the simulated response. For the straight BG it is approximately 2 nm narrower and for the spiral BG it is approximately 7 nm narrower. This indicates that the corrugation depth of 20 nm is too small relative to the grating length of 2800 µm and that strong coupling where most of the light that enters is reflected is never achieved over the length of the grating. In fig. 5.1b the IL was 14.47 dB and 6.86 dB for the straight and spiral CBG respectively. We believe some fabrication imperfection in the waveguide for the straight grating lead to this much higher IL for waveguide and likely

also explains the lower rejection seen here. In this case the data for the straight BG matches the simulated response quite well. Here it should be noted that the simulated result has been scaled to align better with the result for the straight BG. Since the sidewall roughness is not considered in the simulation, the transmission can become much lower than realistically possible, so this is a way to account for this and be able to compare the overall shapes of the experimental and simulation result. The fact that these results align much better indicate that this choice of Δw is more appropriate for the given L. In both cases in the above, grating responses are narrower than the result obtained from simulation especially in the first case with the smaller Δw value. We believe that this is due to the fact that due to the apodization at the beginning and end of the grating, the size of the waveguide corrugations fall significantly below the minimum feature size in the fabrication process which in this case was 10 nm. This then impacts the waveguide with the smaller Δw more, since a larger portion of the grating is below this limit, effectively leading to a shorter grating, which leads to no coupling for some of the λ_B values within it.

In both fig. 5.1a and fig. 5.1b Neither of the spiral BG responses in fig. 5.1 map well with either the simulated results nor the result for the corresponding straight grating, although the wider corrugated one in **(b)** fits better with the straight version and simulation result. Both have a lower bandwidth than the straight versions which implies comparatively lower overall coupling. At the same time the spirals also have large variations in their rejection of light within the reflection bandwidth. This is also present for the less corrugated straight BG, but to a lesser degree and the straight BG with deeper corrugations has a relatively smooth transmission profile. We believe that this effect of large variations inside the reflection band is due to height variations in the Si layer. If we assume that the Si height in a region of the chip varies linearly with the x and y coordinates this would lead to a change in the chirp rate of a linear BG since the actual effective index of a waveguide would deviate from the expected effective index. For a spiral BG on the other hand, this would lead to the actual and expected effective index to fluctuate back and forth as the waveguide spirals. This can lead to cavity effects which will results in spikes in the transmission. As we see in fig. 5.1a this effect is also present in the linear BG, but the effect is less pronounced. That it is also present here could indicated that the height deviation increased until a point

Figure	L [µm]	w [nm]	Δw [nm]	$\lambda_{B,0}$ [nm]	$\Delta\lambda$ [nm]	α	β
fig. 5.2a	8000	600	30	1545	10	3	1.5
fig. 5.2b	8000	600	30	1530	40	3	1.5

Table 5.2: Grating parameters for the SCBGs shown in fig. 5.2.

inside the grating until it started to decrease again. This points to one major issue with a thin Si platform: the relative change in effective index for a waveguide with a high aspect ratio due to changes in width are small which leads to low linear loss but conversely, a small change in waveguide height leads to a large change in effective index, which amplifies effects like the one discussed here and in the end can lead to a large difference between linear and spiraled BGs on this platform.

Another aspect to compare is how the chirp rate $\Delta\lambda$ impacts the performance of SCBGs. The design parameters for a set of CSBGs where the only parameter that is varied is $\Delta\lambda$ is shown in table 5.2. The change in the initial Bragg wavelength $\lambda_{B,0}$ is such that the central wavelength remains the same. The measured and simulated response of these gratings is shown in fig. 5.2. In fig. 5.2a the IL was was 6.00 dB and in 6.42 fig. 5.2b the IL was 6.09 dB. For the case of $\Delta\lambda = 10$ nm in fig. 5.2a, the measured response aligns remarkably well with the simulated response, aside from the overall wavelength shift compared to the design wavelength. For the case of $\Delta\lambda = 40$ nm in fig. 5.2b on the other hand, the bandwidth of the measured response is significantly narrower than the simulated bandwidth. We believe that the reason that this is observed for a high chirp rate is that the Bragg condition is varied so fast that strong coupling never is achieved in the apodized regions due to this fast change in the Bragg condition and low coupling strength. Additionally, the response is shifted further down relative to the case where $\Delta\lambda$ = 10 nm, which is a result of a mistake in the definition of the Bragg wavelength in the script for creating the layout. In the transmission spectrum in fig. 5.2a, the large spikes inside the reflection bandwidth are almost absent, while they are quite pronounced for fig. 5.2b. Based on the hypothesis that these spikes are due to varying heights of the Si layer, the fact that its mostly absent in one of these cases is most likely due to a matter of luck where the spiral in fig. 5.2a was physically located in a location of the wafer where the Si height varied very little. An interesting point to note for both of these reflection spectra is that both

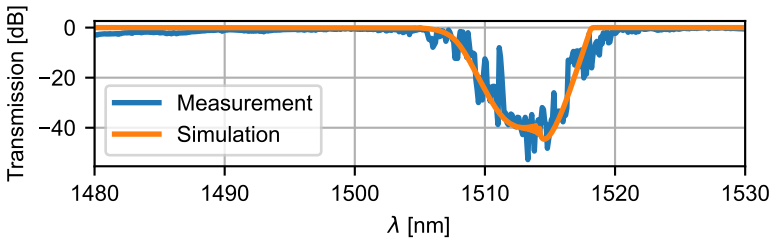

(a)

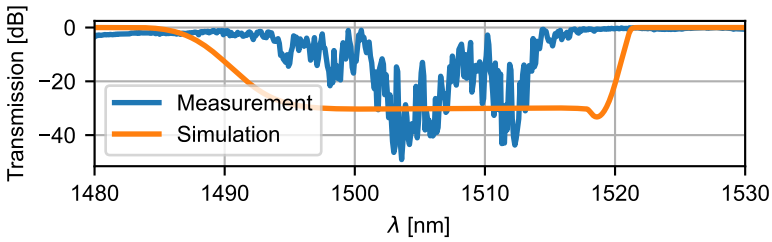

(b)

Figure 5.2: Measured and simulated response for straight and spiral CBGs for the grating design parameters in table 5.2. In both **(a)** and **(b)** the simulated response has been shifted and re-scaled to align with the observed responses.

of them reach a rejection ratio of 40 dB. As mentioned in section 2.2, reaching a large rejection ratio with an ABG is a difficult task as the reflection of light from a BG is a distributed process which requires that the light stays coherent over the length of the grating. The fact that light is rejected with a 40 dB ratio shows that fabrication tolerances in the fabrication process are very good, which is to the credit of SiPhotonIC.

In fig. 5.3, the response of two SCBGs with the design parameters listed in table 5.3 are shown These gratings have the same chirp pa-

Figure	L [µm]	w [nm]	Δw [nm]	$\lambda_{B,0}$ [nm]	$\Delta\lambda$ [nm]	α	β
fig. 5.2a	8000	700	35	1545	10	3	1.5
fig. 5.2b	8000	700	35	1530	40	3	1.5

Table 5.3: Grating parameters for the SCBGs shown in fig. 5.3.

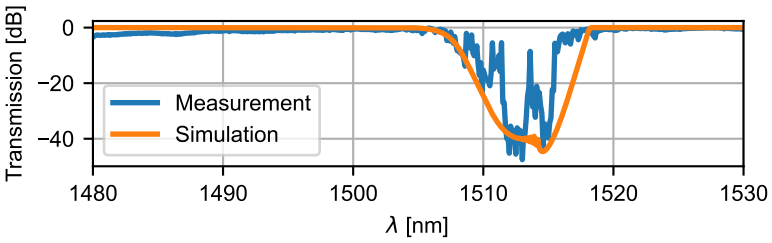

(a)

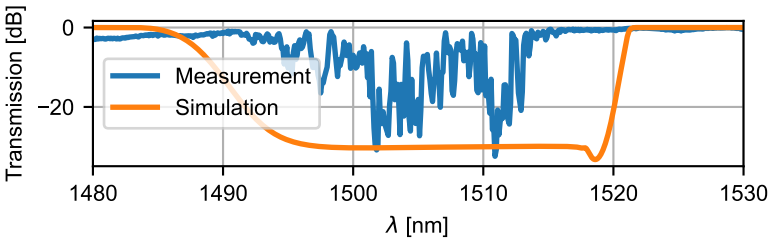

(b)

Figure 5.3: Measured and simulated response for straight and spiral CBGs for the grating design parameters in table 5.3. In both **(a)** and **(b)** the simulated response has been shifted and re-scaled to align with the observed responses.

rameters relating to the Bragg wavelength as in fig. 5.2, but are based on 700 nm wide waveguides with 35 nm corrugations. In fig. 5.3a, the IL was 5.33 dB and in fig. 5.3b it was 5.71 dB. As can be seen, the responses are very close to the ones shown in fig. 5.2. The measured response in fig. 5.3a does not fit as well with the simulated response as the example shown in fig. 5.2a, which is likely due this grating having slightly lower coupling. An interesting feature that can be seen in figs. 5.2b and 5.3a and fig. 5.3b is that the transmission decreases when going from short to long wavelengths until it starts to increase again. After this, it decreases before increasing again until the end of the reflection band. We believe that this again is due to a slope in the Si height along the x and y coordinates. The fact that this occurs for these gratings but not for the one shown in fig. 5.2a is remarkable and indicates that the placement of this grating was very lucky. Several more SCBGs were implemented on this chip in order to investigate

the effects of changing Δw and $\Delta\lambda$, but the conclusions that can be gathered from these are summed up in the findings detailed here. Gratings that varied the apodization parameters α and β were also implemented, but these were with a chirp rate of $\Delta\lambda = 20$ nm, which lead to low coupling and made it hard to draw concrete conclusions from the measured spectra.

We had intended to use the measured IL to gain information about the propagation loss experienced by the platform. Unfortunately, the cleaving of the chip left a one of the edges slightly jagged which impacts the performance of the inverse taper couplers. This jagged edge was only present for the waveguides with a length of 2800 µm shown in fig. 5.1, which in the end have a higher IL than the significantly longer waveguides shown in fig. 5.2 and fig. 5.3, making us unable to make any concrete statements about the loss experienced in the different waveguides.

As we have seen for all gratings here, the response is shifted to shorter wavelengths by approximately 35 nm and as noted this can be explained by deviations in the height of the Si layer compared to the design parameters. We were after production of the chip informed by the fabricator that the average Si height of the wafer was 98.7 ± 2.83 nm, based on 10 data points taken across the full wafer. In fig. 5.4, the change in λ_B as a result of a difference in the design and actual height is shown along with expected distribution of heights. As can be seen, a difference in height that would result in a shift -35 nm in λ_B is slightly outside one standard variation, but we believe it to be entirely likely that this could be the cause of the wavelength shifts as the wafer is large compared to the size of the chip and since we only have a few points of measurement to base the distribution of heights on.

5.1.2 Coherency Broken Bragg Gratings

A wide array of CBBGs were implemented on this chip in order to investigate the effects of changing the both length and number of subgratings and the corrugation depth of the subgratings. Unfortunately a mistake in the early version of the simulation framework used for the calculation of the effective indices of TE_1 modes which is used in the calculation of the grating period, led to the response of these gratings being shifted to significantly longer wavelengths and outside of the region we are able to measure. The way the the period of the ABGs was calculated in the design of this chip was based on the waveguide

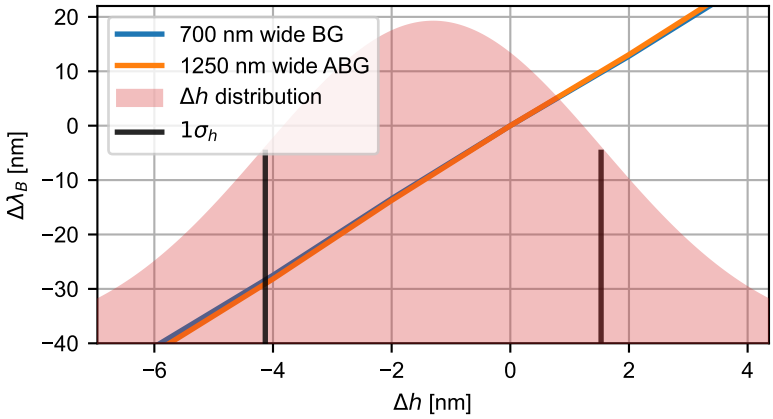

Figure 5.4: Deviation in Bragg wavelength for two different gratings as a function of the change in Si height relative to design height.

width w and the corrugation depth Δw. The effective indices in the range w to $w + \Delta w$, was calculated and the average effective index was used to calculate Λ. This would be correct for a SBG, since this has a varying width, but for an ABG defined in the way it was on this chip, the actual waveguide width is just $w + \Delta w$. The error in the simulations were that the step size in the simulation was too large. This resulted in an abrupt change in the effective index of the TE_1 mode as the waveguide width decreases, significantly before the mode cutoff. An illustration of these two effects for a waveguide with $w = 900$ nm and $\Delta w = 500$ µm (which means that the actual width is 1400 nm) is shown in fig. 5.5. For the low resolution case, which is the data that was used in designing the chip, the average index over the considered width is considerably lower than the actual average effective index. Coupled with the fact that Λ should have been calculated using only the effective index at $w = 1400$ nm in this example and the result is that the actual λ_B of this ABG is 106 nm longer than intended. This effect is only amplified for waveguide with smaller Δw. Most CBBGs on this chip had $\Delta w =$ between 150 nm and 200 nm, which leads to a shift in λ_B of over 200 nm, putting it well outside of the range of wavelengths that we have the ability to measure with our equipment.

Fortunately, in this case there is both the shift in wavelength due to the change in Si height and another effect that we do not understand properly at the time of writing. This is the fact that the response of CB-

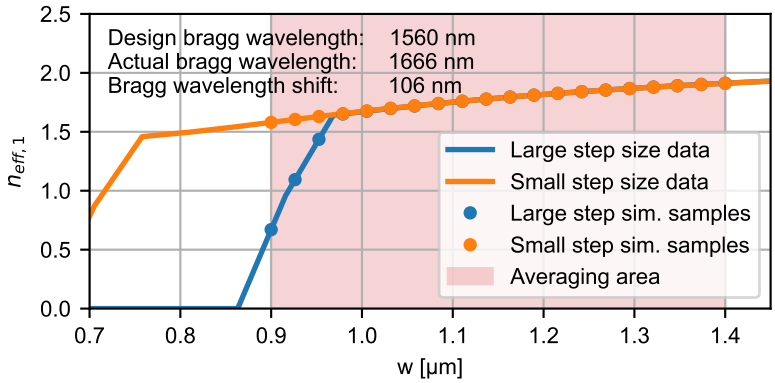

Figure 5.5: The effective index of the TE_1 mode in a 100 nm Si waveguide for a low and high simulation resolution. The data found from simulation is shown as lines and the samples taken are shown as dots.

BGs with large Δw shift down in wavelength relative to the expected. Since we could not measure most CBBGs on this chip, it was only significantly later that we realized that this effect was present and a proper explanation for it is still lacking. In the end, this effect had the result that a set of CBBGs were shifted far enough down that their response could be measured. These were the $w = 1400$ nm gratings with $\Delta w = 500$ nm, which means that the shift due to the design and simulation error impacted these less. The expected shift due to the design and simulation error is 106 nm, while the shift due to the height change is approximately 35 nm. This still leaves them around 70 nm above the design wavelength, but the shift due to the large Δw brings them very close to where they were designed to be in wavelength, as shown in fig. 5.6 where the response of three CBBGs with L =150 μm, L =200 μm and L =250 μm is shown. The shared parameters for these CBBGs are listed in table 5.4 Due to the apodization profile

w [nm]	Δw [nm]	w_1 [nm]	λ_B [nm]	α	β	r_{bend} [μm]	l_{tp}[μm]
1400	500	680	1560	3	1.5	25	15

Table 5.4: Grating parameters for the CBBGs shown in fig. 5.6

used here, side-lobes in the spectrum are present on the short wavelength side of the of the rejection band, but the long wavelength side has a very sharp roll off for all CBBGs. The filter with the sharpest

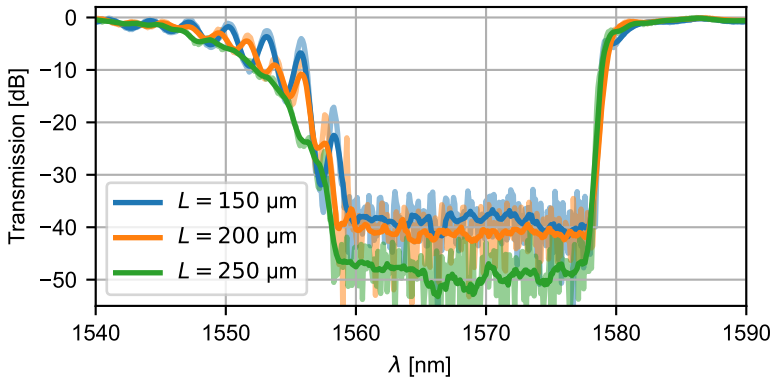

Figure 5.6: Transmission comparison of three CBBGs each consisting of 6 ABGs with lengths shown in the legend, w =1400 nm and Δw = 500 nm. The spectral data has been smoothed to show average transmission inside the rejection band more clearly, with the smoothed version shown in full color and the original data in the same color but transparent.

roll off is the one with $L = 250$ µm, where it is 44 dB/nm. This is very useful for the intended use case as pump filter after FWM as this makes it possible to do FWM with very low detuning. But changing the apodization profile, we expect to be able to get this type of roll off on both sides of the stop band. As can be seen, and as would be expected, the rejection ratio for the CBBGs increase as the length of the ABGs increases, from a rejection that just exceeds 40 dB for the case with $L = 150$ µm to more than 50 dB for the case where $L = 250$ µm, which is impressive for filters with a total length of 1500 µm.

5.1.3 Filtered Four-Wave Mixing

In somewhat of a stroke of luck the CBBGs where the wavelength shifts due to fabrication imperfections and simulation errors almost perfectly cancelled each other out were parts of the circuits intended for testing how well we could filter out the pump and signal in a FWM process. These three circuits consisted of a 6 mm long waveguide for FWM appended by a CBBG. It is not possible to reach the zero dispersion with simple 100 nm tall rectangular waveguides, so the conversion efficiency and bandwidth was limited by this. Since zero dispersion was not achievable, the waveguides were instead optimized to minimize the mode area, which happens at a waveguide width of 700 nm, as this will increase the intensity of the field, thereby

increasing the strength of the nonlinear interaction. Each circuit had CBBGs comprising six filters with the individual length of the ABGs being 150 µm, 200 µm and 250 µm for the first, second and third circuit respectively. The ABGs had an average width of 1250 nm and a corrugation depth of 500 nm. A microscope image of the three circuits is shown in figure fig. 5.7. The spirals are the 6 mm long FWM waveg-

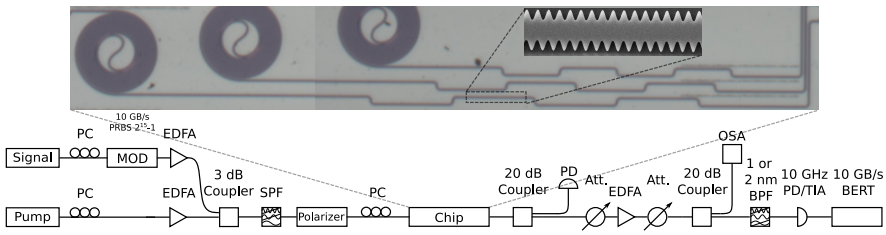

Figure 5.7: Sketch of the experimental setup for wavelength converting a 10 Gb/s signal using the on-chip FWM waveguide and CBBG. The image shows a microscope image of the circuit used in the experiment along with a SEM image of one of the ABGs.

uides and the waveguides alternating up and down are the CBBGs. In order to demonstrate the utility of the circuit, wavelength conversion of a 10 Gb/s OOK signal was demonstrated using circuit 4.0.3 and the setup also illustrated in fig. 5.7. In the setup, the signal laser is a Santec TSL-550 tuneable laser, which modulated the OOK pattern using an intensity modulator driven by an Anritsu MP1763C pulse pattern generator set to generate a PRBS signal of length $2^{15} - 1$. After modulation the data signal is amplified using an L-band EDFA. The pump is a CoBrite DX1 laser (also tunable) which is directly amplified using an EDFA. The signal and pump are then combined on a 3 dB coupler and short-pass filtered to remove as much ASE before FWM. The combined light is then coupled onto the circuit using lensed fibers and edge couplers. Here the FWM process takes place and the signal and pump is suppressed using the CBBG. The transmission spectrum for the filter used is the CBBG with $L = 250$ µm shown in fig. 5.6. This spectrum, shows a rejection ratio averaging 48 dB in the main reflection band and going below 50 dB in some areas. Since the sections need to have waveguide bends between them, this can also be used to fit the CBBG onto a chip in a variety of configurations, by for instance folding the filter back and forth. After FWM and filtering, the light is coupled off the chip using a lensed fiber. The light is passed through a 20 dB coupler, with the small por-

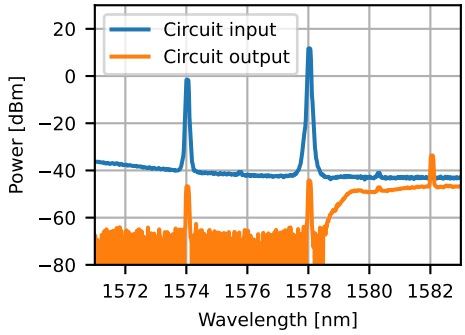

(a)

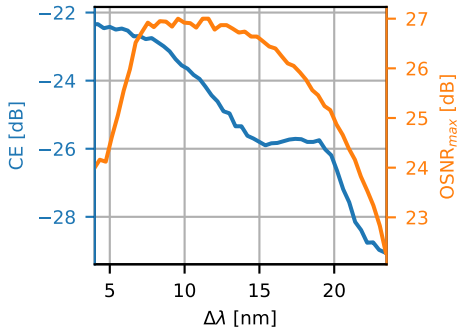

(b)

Figure 5.8: **(a)** A comparison of the spectra at the input and output of the chip. **(b)** FWM conversion efficiency (blue, left axis) and OSNR of the generated idler (orange, left axis).

tion of the light measured on a PD. The rest of the light passed on to an EDFA which is placed in between two variable attenuators, which makes it possible vary the OSNR of the received signal. Finally another 20 dB coupler passes a small portion of the light to an OSA for recording the generated spectra. The rest of the light is band-pass filtered, detected on a 10 GHz PD and a BERT is carried out using a Anritsu MP1764C Error Detector. An example of the input to the circuit and the output is shown in fig. 5.8a. This demonstrates the effectiveness of the CBBG in filtering the signal and pump after FWM as the resulting idler has more power than the inputs even though the conversion efficiency is not great. This figure also demonstrates that

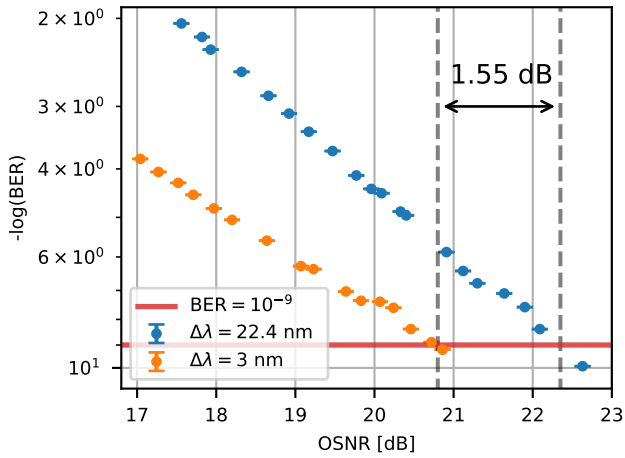

Figure 5.9: $-\log(\text{BER})$ as a function of OSNR for FWM detunings of 22.4 nm and 3 nm, showing a 1.55 dB better performance for the 22.4 nm case. The BER$= 10^{-9}$ line corresponds to error free transmission in this configuration.

the FWM process takes place in the PIC and not in the fiber leading to it. In figure fig. 5.8b the CE of the FWM process is shown together with the OSNR of the idler. The OSNR is recorded for $\lambda_{pump} = 1578$ nm while the CE is recorded for $\lambda_{pump} = 1595$ nm. This is due to the fact that CE cannot be recorded for λ_{pump} and $\Delta\lambda$ combinations that result in either the pump or signal lying inside the stop band of the CBBG, with the underlying assumption being that this does not seriously change the CE. We see that the OSNR roughly follows the CE except at $\Delta\lambda = 4{-}7.5$ nm where the OSNR increases and at $\Delta\lambda = 15{-}20$ nm where the CE has a shoulder that is not seen in the data for the OSNR. In the low detuning range this is due the idler starting to stop band of the CBBG. I have no good explanation for why the shoulder in the 15-20 nm range does not appear in the OSNR results, but it could be due to the actual CE being slightly different when the pump is placed at 1578 nm. Finally in fig. 5.9, $-\log(\text{BER})$ as a function of idler OSNR is plotted for $\Delta\lambda = 3$ nm and $\Delta\lambda = 22.4$ nm, with the error free transmission highlighted with a red line. We see that the high detuning case experiencing a 1.55 dB penalty in OSNR in order to reach error free transmission. I believe that the difference is simply due to generated idler being larger at $\Delta\lambda = 3$ nm compared to the $\Delta\lambda = 22.3$ nm case. These results were summarized in a ex-

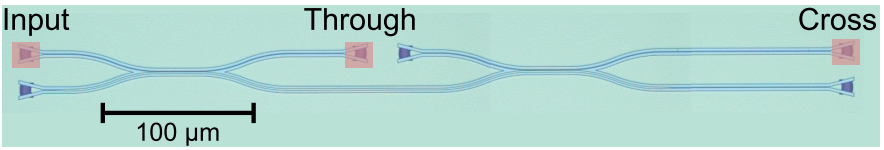

Figure 5.10: Microscope image of a circuit used for testing MMCs. Power can be coupled in a the GC labeled Input and measured at the GCs labeled Cross and Through to calculate the SR of the MMC

tended abstract and submitted to the CLEO 2022 conference where it was accepted and presented as a poster[77].

5.2 Silicon Nitride on Thin Film Lithium Niobate

This chip was designed and fabricated as a part of an exchange to InPAC at RMIT. This group works with their own SiN on LNOI platform and due to this, the chip was fabricated on this platform. The platform consists of a 300 nm LNOI layer and a 300 nm SiN layer on top. On this chip, we investigated the performance of MMCs by themselves and how MMCs performed when coupling light reflected from ABGs to an output port.

5.2.1 Multi Moded Couplers

In fig. 5.10 a microscope image of a circuit used for evaluating the performance of MMCs is imaged. It consists of two MMCs placed back to back with the input port being on the single moded part of the MMC and can be used to measure the amount of power that passes straight through the coupler without converting to the TE_1 mode by measuring the power at the through port or to measure the amount of power that is converted to the TE_1 mode and back by measuring at the cross port. The SR will then be the difference between the power measured at the two ports (with the fact that the power at the cross port has passed through two couplers accounted for), with this measured power normalized relative to the performance of the GCs. Figure 5.11 shows measurements of the SR of a MMC in the fabricated SiN on LNOI chip changes as a series of parameters is changed. such that power could be coupled from to the single mode waveguide of one MMC, couple to the multi mode waveguide and then couple back to the single mode waveguide of the next MMC coupler. GCs were placed such that the power coupled Here the SR is defined as $P_{\text{cross}} - P_{\text{through}}$, and a no power coupled to the through port is the ideal case, a larger SR value is better. The parameters found for the base design of the MMC is

listed in table 5.5. In fig. 5.11a, both w_1 and w_2 are changed by the

w_1 [nm]	w_2 [nm]	w_{gap} [nm]	L_{cpl} [µm]	λ [nm]
1200	2870	200	54	1500

Table 5.5: Base parameters for MMCs shown in fig. 5.11 (see fig. 3.4.

same amount, Δw, but the gap between the waveguides are kept the same. We see that both a too large change results in a worse splitting ratio, but that a value slightly smaller than the design value is better. In fig. 5.11b, we see the opposite trend: here w_{gap} and w_2 are both kept constant while w_1 changes and we see that a larger w_1 results in a larger SR. For both fig. 5.11c and fig. 5.11d where w_2 and w_{gap} are varied the the behavior is the same, with the SR having a reverse proportionality with the varied parameter. This behavior is then repeated in fig. 5.11e, where a reduction in the coupling length leads to an increase in SR, although it reaches a maximum at $\Delta L = -4$ µm. It is hard to draw a single conclusion from these plots but several points can be made. From the sweeps of w_1 and w_2 by them selves, it seems that the phase matching was not completely ideal since both waveguides need to have their width changed in opposite directions in order to achieve better coupling. The sweep of w_{gap} seems to indicated the coupling strength is too small compared to the length of the coupler since a narrower gap leads to stronger coupling. The fact that the sweep of L_{cpl} shows that a slightly shorter length than the original design leads to a better coupling indicates the opposite of the sweep of w_{gap}, since this indicates that all power has been coupled to the multi mode waveguide and is starting to couple back for $\Delta L = 0$. The fact that a slightly reduced coupling length results in a better coupling ratio is not a surprise since the bending region of the couplers where the waveguides are removed from each other has not been taken into account during the design, and there will be a part of this area where coupling still occurs. Regarding the fact that the results for the sweep of L_{cpl} and w_{gap} seem to contradict each other, we have no satisfying explanation at this point. Overall, these sweeps contain valuable data that can be used in further optimizing the performance of the MMCs on this platform. The fact that the SR in the sweeps of w_1, w_2 and w_{gap} does not reach a maximum suggest that the if future experiments are carried out, it would be valuable to increase the range of these sweeps further in the direction of a maximum, to achieve greater SRs. The best performing of the MMCs shown in this

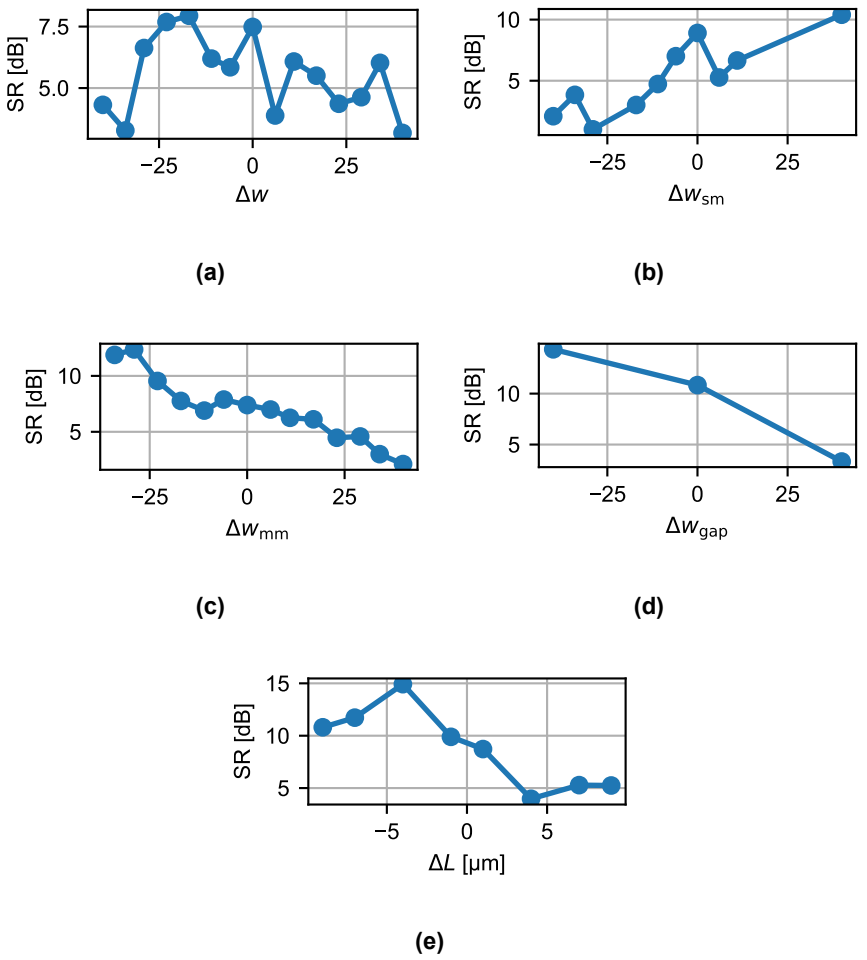

Figure 5.11: The measured splitting ratio of a series of different MMCs where different parameters are swept, with the base parameters listed in table 5.5. for MMCs as different design parameters are varied. **(a)** Sweep of both w_1 and w_2 at the same time. **(b)** Sweep of w_1. **(c)** Sweep of w_2. **(d)** Sweep of w_{gap}. **(e)** Sweep of L_{cpl}.

set of sweeps is the one that is unchanged from the base parameters, except that L_{cpl} is changed by -4 µm and also happens to be the best performing MMC of the ones implemented on the chip. The spectral response of this MMC is shown infig. 5.12 The center wavelength in the design was 1550 nm, but the GCs all had a transmission profile approximately centered on 1510 nm, so the range from 1500 nm –

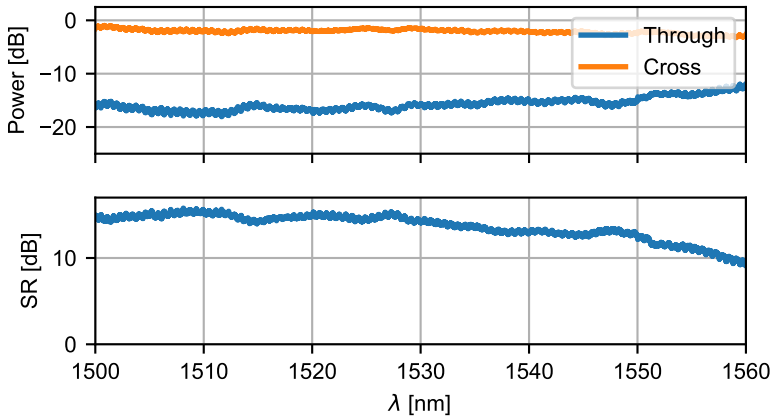

Figure 5.12: Transmission to the through and cross port, normalized to the GC loss, of a MMC with parameters as listed in table 5.5 and length changed by -4 µm.

1600 nm is shown, since very low amounts of power is coupled above this, which makes the spectra very noisy. The SR stays above 10 dB almost the full range, and above 15 dB in the range from 1500 nm – 1600 nm, which we consider quite a good result, which demonstrates the broadbanded nature of the MMC when optimized to as large a splitting ratio as possible.

5.2.2 Multi Moded Couplers and Asymmetric Bragg Gratings

The MMCs were also implemented in conjunction with ABGs to demonstrate their utility in collecting the light reflected from ABGs. Before investigating this specifically, let us look at the transmission of a four CABGs with varying Δws, based on the parameters listed in table 5.6. The transmission spectra of these are shown in fig. 5.13. We see that

w [µm]	L [µm]	$\Delta\lambda$ [nm]	α	β
3	1000	7.5	3	1.5

Table 5.6: Base parameters

the grating with $\Delta w = 375$ nm never achieves full coupling judging from the fact that the transmission never reaches the same floor as for the other gratings. As expected the bandwidth of the gratings increases with Δw, but also that the long wavelength side of the grat-

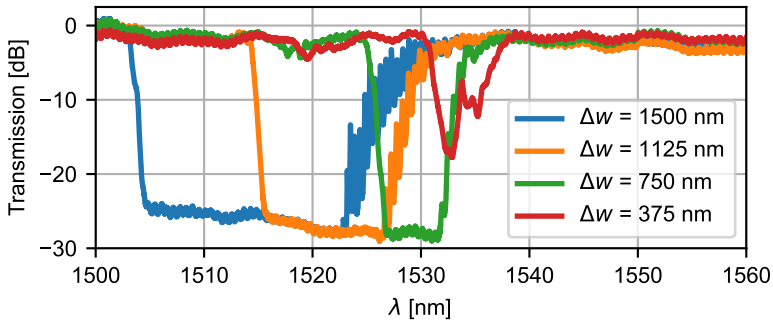

Figure 5.13: The transmission spectra of four CABGs with varying Δw's and other parameters listed in table 5.6.

ings gain ripples that also increase with Δw and that the overall response of the gratings are shifted down in wavelength. The increase in ripples is due to the fact that the gratings are sinusoidally corrugated and that fabrication resolution is 100 nm. As the corrugations start to grow as they are turned on by the apodization profile, this means that the sharp edges of the corrugations are dulled, which does not happen evenly for the peaks and troughs of the corrugation with the result that the width of the waveguide is changed slightly along its length. The fact that the ripples are on the long wavelength side of the response indicates that the width is slightly decreased and that the effective indices are correspondingly increased. This on the other hand does not account for the magnitude of the overall wavelength shift of the response. This is the same effect that was mentioned in section 5.1, which we currently do not have a good understanding of.

In fig. 5.14 the transmission and reflection of an ABG where the reflection is collected with an MMC is shown. The grating parameters are the same as in table 5.6 and $\Delta w = 1125$. The MMC parameters are the same as in table 5.5 with the length 3 µm shorter than in the table. Both the transmission and reflection has been adjusted to account for the GC losses and have been normalized to the maximum transmission in the observed range. As we see, the light is efficiently coupled over the full reflection band, with the extra loss incurred from coupling in the MMC being 1 dB on the short wavelength side and 3 dB on the long wavelength side. The difference is most likely due to

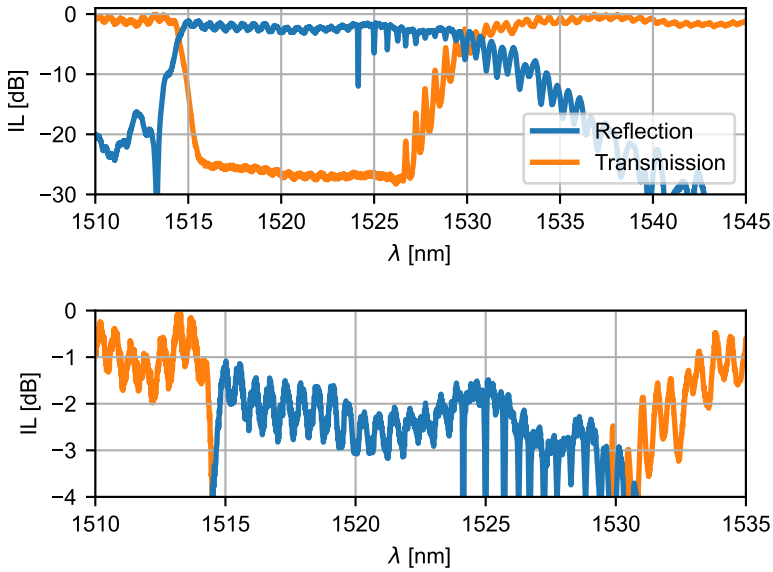

Figure 5.14: Plot of best performing ABG + MMC combination

extra propagation losses incurred due to the chirp of the ABG along with the MMCs generally performing a little worse further away from 1550 nm. Additionally, there is some noise involved in the process of factoring in the GC transmission profile, as is visible from the sudden jump in transmission just before 1515 nm. Nonetheless, we are not comfortable claiming a extra loss of less than 1 dB as a result of the coupling using the MMC based on these data. Importantly, between 1 and 3 dB of extra loss is a significant improvement relative to the 6 dB that would be incurred when using traditional methods of collection of reflected light. More than that, based on the analysis of the MMCs we have strong reason to believe that this result can be improved with more optimization.

5.3 250 nm SOI

This chip was designed mainly to investigate two things: The behavior of CBBGs as different parameters are changed, since we did not learn what we wished to from the chip discussed in section 5.1. Additionally, we wished to attempt to create an integrated time-lens with the dispersion generating CBGs/CABGs, FWM waveguide and CBBG contained in the same circuit. Due to the need for two inputs

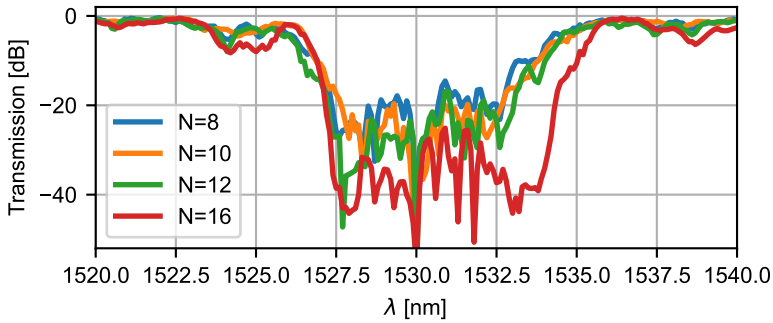

Figure 5.15: Response of several CBBGs with differing lengths, with other grating parameters listed in table 5.7

to these time-lens circuits, the inverse taper couplers were not angled on this chip as we needed to be able bring a fiber array with two lensed fibers in a position where both lensed fibers coupled optimally to the two input waveguides, and we could not procure angled lensed fiber arrays.

5.3.1 CBBGs

The first set of parameters we swept for the CBBGs were the number of ABGs they consisted of. The shared parameters of these CBBGs are listed in table 5.7, and their transmission is shown in fig. 5.15.

L [µm]	w [nm]	Δw [nm]	λ_B [nm]	α	β	w_{sm} [nm]	L_{tp} [µm]
100	1200	400	1550	3	1.5	450	20

Table 5.7: Shared parameters of the CBBGs with responses shown in fig. 5.15.

As is expected, the rejection ratio of the CBBGs increases with the number of ABGs, going from 20 dB with 8 ABGs to 40 dB with 16 ABGs. One unexpected feature is that the transmission has a sudden decrease for all CBBGs at 1530 nm. This is the wavelength at which the input polarization was optimized to achieve the greatest reduction of the output. We would expect the optimal polarization to remain unchanged over the bandwidth of the grating. For the results shown in fig. 5.6, the polarization was also optimized in the same way at the central wavelength, and this did not lead to the same behavior, so the result here is surprising. We believe this effect could be a re-

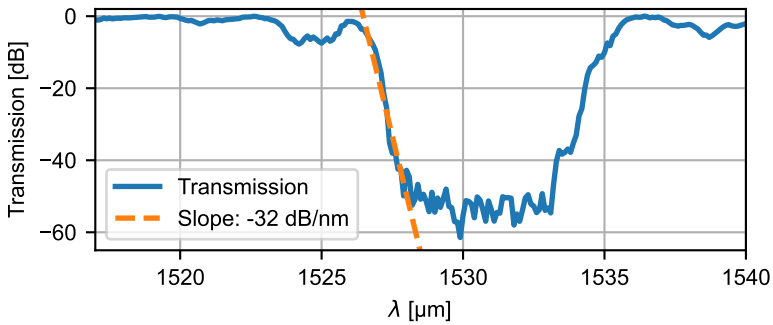

Figure 5.16: Plot of the transmission of a CBBG where the polarization has been optimized at each measurement step inside the rejection band

sult of the non-angled inverse taper couplers resulting in interference. As a comparison we did a measurement of the grating with $N = 16$, where the polarization was optimized to maximize the rejection ratio at each wavelength step inside the rejection band. The result of this is shown in fig. 5.16, where a much more consistent transmission profile is achieved. A rejection ratio of 60 dB is reached at the center and the average rejection ratio is 54 dB. This outperforms both the highest and average rejection ratio achieved by the best CBBG shown in fig. 5.6, which had an average rejection ratio of 48 dB and a peak rejection ratio of just above 50 dB. The roll off of the previous CBBG was 44 dB/nm, which still outperforms this one which has a roll off of 33 dB/nm. Nonetheless, this performance is also achieved by step wise optimization of the polarization. A future task will be to investigate if the variations inside the stop band can be reduced by improving the polarization stability of the setup used to measure the performance of the circuits, or by other means.

The second sweep we carried out, was of the corrugation depth of the ABGs. The shared parameters of this sweep are shown in table 5.8. and their transmission is shown in fig. 5.17. We see that

L [µm]	w [nm]	N	λ_B [nm]	α	β	w_{sm} [nm]	L_{tp} [µm]
200	1200	10	1550	3	1.5	450	20

Table 5.8: Shared parameters of the CBBGs with responses shown in fig. 5.17.

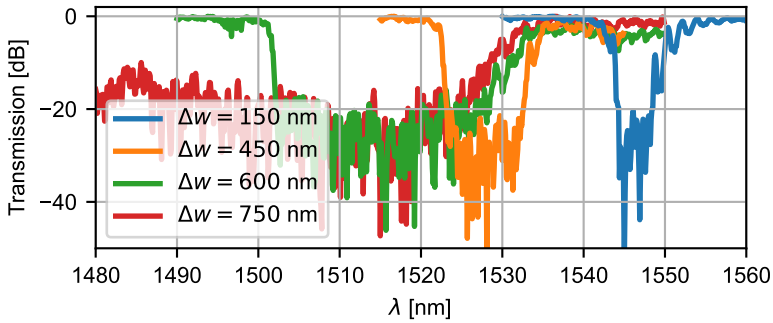

Figure 5.17: Response of several CBBGs with differing numbers of ABGs, with other grating parameters listed in table 5.8.

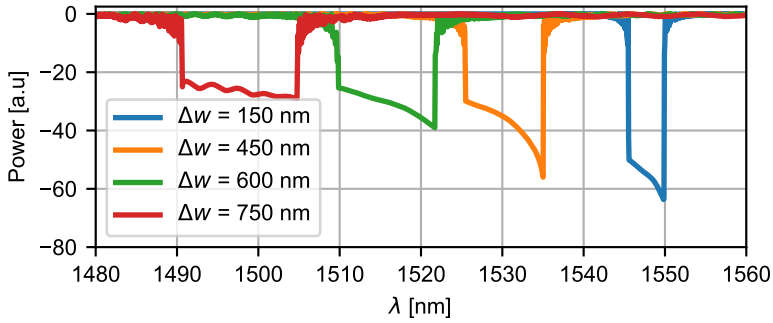

Figure 5.18: EME simulation of ABGs with $L = 2000$ µm and varying Δw, with the other grating parameters listed in table 5.8.

the bandwidth of the gratings increase and and that the response of the gratings are shifted down as Δw increases. That the bandwidth increases is to be expected, but surprisingly enough, the rejection ratio starts to decrease after Δw exceeds 450 nm. We have of course mentioned the fact the the ABG response is shifted down as Δw increases, but have never elaborated on this. In order to gain some deeper understanding, we have run a set of EME simulations of unapodized ABGs with a $L = 2000$ µm which is the combined length of the ABGs the CBBGs in the above correspond to. Otherwise the ABGs are equivalent to the ones shown in fig. 5.17. The simulation results are shown in fig. 5.18. The larger Δw is in these simulations, the less they correspond to our experimental results, but the shift in the

response corresponds very well with our experimental results. That the bandwidth does not match seems, at least partly, to be a matter of the resolution used in the simulation, as larger resolution (that is, worse), led to the gratings with large Δw to have a narrower bandwidth than what is shown here. Our initial hypothesis of what causes this wavelength shift, was that since the gratings are sinusoidally corrugated, the radius of curvature of the waveguides is changing with the phase of the corrugation. This would lead to a change in the effective index and thus λ_B. Presently, we are not sure if this is the correct theory as some aspects speaks against it. Firstly, it would only be a small region of each period that has a high radius of curvature, so large parts of the ABG should still couple to the λ_B dictated by the design. Secondly, we are not sure that EME simulations would be able to capture effects that result from the curvature of the waveguide, as this type of simulation cannot simulate waveguides with a varying radius of curvature. In the simulation, the waveguide is divided into many short sections, with each section treated as a completely straight waveguide. Presumably, this means that the shift in λ_B is a result of some different effect. We must admit that we do not have a good answer presently, and will instead design ABGs with a relatively low Δw or account for the shift in λ_B using simulations like the one shown here until we have a better answer.

5.3.2 Time-Lens Circuits

The main goal of this chip was to implement a time-lens circuit for carrying out an OFT. For this we designed several different types of circuits, based on a standard layout which is shown in fig. 5.19. Light

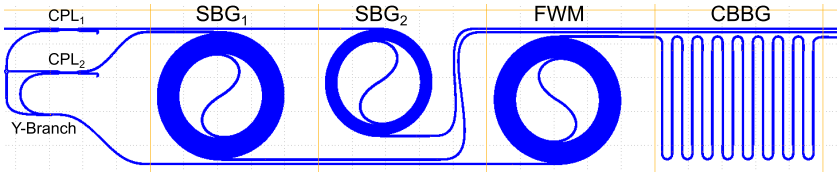

Figure 5.19: A time-lens circuit consisting of two SCBGs, $SCBG_1$ and $SCBG_2$ that are each coupled to a FWM waveguide using the couplers CPL_1 and CPL_2 and the Y-Branch and filtered by a CBBG after the FWM waveguide.

is coupled into the circuit using two inverse taper couplers (not shown) and passes through the couplers CPL_1 and CPL_2 to the two SCBGs. The dispersion of $SBG_1 = D_2$ and the dispersion of $SBG_2 = -D_2/2$.

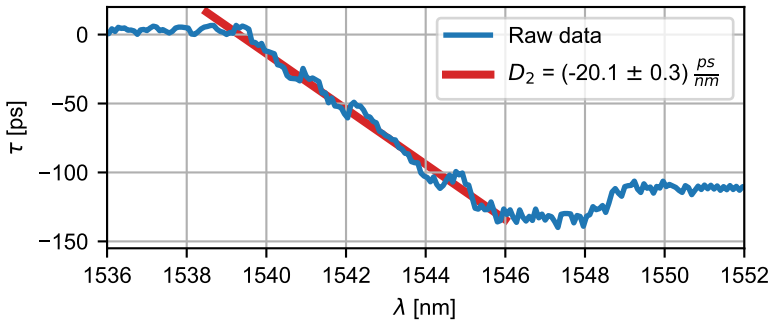

Figure 5.20: Measured group delay, τ of the grating with parameters shown in table 5.9 and a fit to τ in the region of dispersion showing a dispersion of (-20.1 $\pm$ 0.3) ps/nm

The reflected light from each of the SBGs is then combined on a Y-Branch and propagates to the FWM spiral. After this, the light passes through a CBBG which filters the pump away. Two main variations were implemented. In one, the SBGs are based on CABGs and the couplers are MMCs. In the other the SBGs are based on CBGs and coupling is done using two Y-branches. This should allow us to test if the expected reduction in loss due to using MMCs and ABGs would happen. Each of these two main types had a variation where the CBBG was removed such that we could record FWM spectra where no filtering had taken place. Additionally, the circuits based on CBGs, had a variation where the CBGs were based on wider waveguides that were multi moded. As discussed in section 5.1, this should also lead to a reduction in loss, since wider waveguides have lower loss.

One important parameter to measure for these circuits was the group delay, and the dispersion that can be derived from this, since this is crucial for achieving the desired TDM to WDM mapping. We based our measurements of this on the work of K. R. H. Bottrill et al.[78], which uses spectral interference to measure the dispersion of a single-pass device. The first example of a measurement is shown in fig. 5.20. Here a CBG based on a single mode waveguide with the design parameters listed in table 5.9 is shown. As this had a desired dispersion of $D_2 =$ -18 ps/nm the acquired dispersion of $D_2 =$ -20 ps/nm is acceptable and range over which the dispersion occurs fits exactly with the designed range of 1538.5 nm to 1546 nm. Its counterpart with

L [µm]	w [nm]	Δw	$\lambda_{B,0}$ [nm]	$\Delta\lambda$ [nm]	D_2 [ps/nm]
4695	450	150	1546	-7.5	-18
α	β	R_0 [µm]	ΔR [µm]	α	
3	1.5	120	6	0.61	

Table 5.9: Grating parameters of the waveguide shown in fig. 5.20

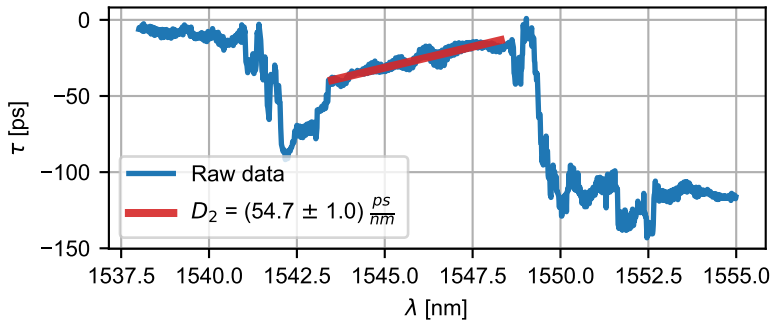

Figure 5.21: Measured group delay, τ of the grating with parameters shown in table 5.10 and a fit to τ in the region of dispersion showing a dispersion of (57.7 $\pm$ 1) ps/nm

the design parameters shown in table 5.10 on the other hand is another matter. The measured group delay of this waveguide is shown

L [µm]	w [nm]	Δw	$\lambda_{B,0}$ [nm]	$\Delta\lambda$ [nm]	D_2 [ps/nm]
10500	450	150	1550	7.5	36
α	β	R_0 [µm]	ΔR [µm]	α	
3	1.5	120	6	0.61	

Table 5.10: Grating parameters of the waveguide shown in fig. 5.20

in fig. 5.21. The group delay is approximately linear in a range around 1545 nm, but the slope here is $D_2 = 54.7$ ps/nm which is far from the goal of 36 ps/nm. In the end this is besides the point, since the design range is 1550 nm to 1557.5 nm, and this range overlaps with that of the previous grating. Generally we had great difficulty achieving consistent results with this method of measurement, as it seems to be highly sensitive to noise and thus requires a strong input signal. In measuring an integrated circuit, we are limited in power by what we can input both by the threshold at which the waveguide itself

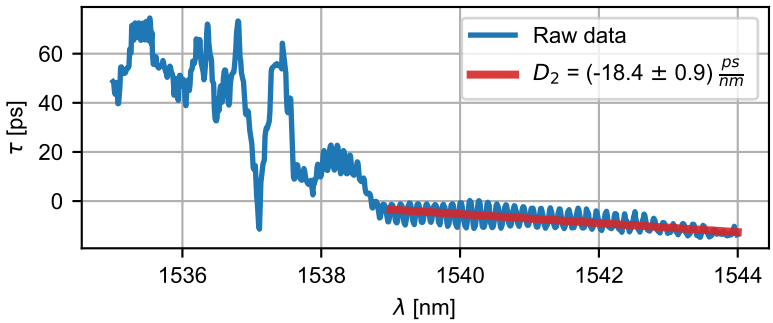

Figure 5.22: Measured group delay, τ of the grating with parameters shown in table 5.11 and a fit to τ in the region of dispersion showing a dispersion of (-18.4 $\pm$ 0.9) ps/nm

burns and the same for all the components that come before coupling into the chip. Since we are measuring the phase accumulated by propagation through the circuit and deriving the group delay from this, if the noise is so large that it leads to a measured phase difference larger than 2π between consecutive points, information is lost and we cannot calculate the group delay correctly. This also means that the larger the dispersion is, the harder it becomes to measure it, since the phase is evolving faster. We believe that this is the main factor that hampers our measurements and we have not been able to verify that we have sets of SBGs with properly matched dispersion. We have one more successful measurement for a SBG based on a multi moded CBG, with design parameters listed in table 5.11. The

L [µm]	w [nm]	Δw	$\lambda_{B,0}$ [nm]	$\Delta\lambda$ [nm]	D_2 [ps/nm]
5248	1000	150	1546	-7.5	-18
α	β	R_0 [µm]	ΔR [µm]	α	
3	1.5	120	6	0.61	

Table 5.11: Grating parameters of the waveguide shown in fig. 5.22

measured group delay of this grating is shown in fig. 5.22. Again, this aligns very well with the design parameters, with the dispersion occurring in the correct wavelength range and it matching the desired dispersion of -18 ps/nm within the uncertainty of the measurement.

Regardless of our trouble with verifying the dispersion of the SBGs,

we carried out FWM experiments to attempt and create a time-lens. Unfortunately, the CE was very low, most likely due to high losses in the circuits. We were only able to achieve measurable FWM using a Continuous Wave (CW) laser on time-lens circuits based on CABGs and on those based on multimoded CBGs. The generated signal, pump and generated idler for a CABG and MMC based circuit is shown in fig. 5.23a and the CE is shown in fig. 5.23b. In the

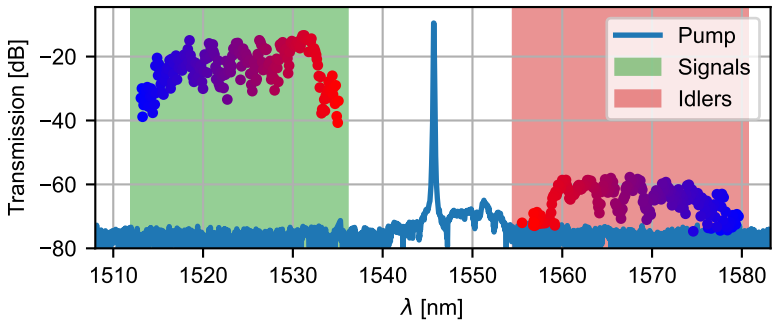

(a)

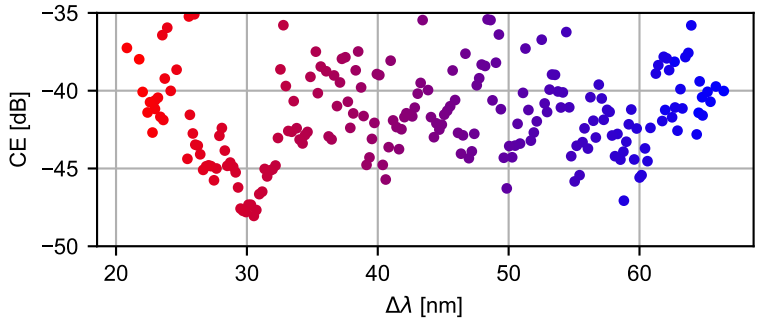

(b)

Figure 5.23: Data for a FWM process in a time-lens circuit based on SABGs with no pump filtering. λ_{pump} is 1545.7 nm. **(a)** Sweep of the signal detuning, with the signal and idler at each wavelength shown in matching colors. **(b)** CE for the data shown in **(a)**.

figures, the corresponding signal/idler pairs are matching in color. As we see, the CE is very low — between -48 and -35 dB —, which is unfortunate. We believe that this is mostly due to both pump and signal

experiencing high losses due to a large propagation distance before reaching the FWM waveguide. Another example of this is shown in fig. 5.24. In these figures, the circuit was based on multimoded CBGs

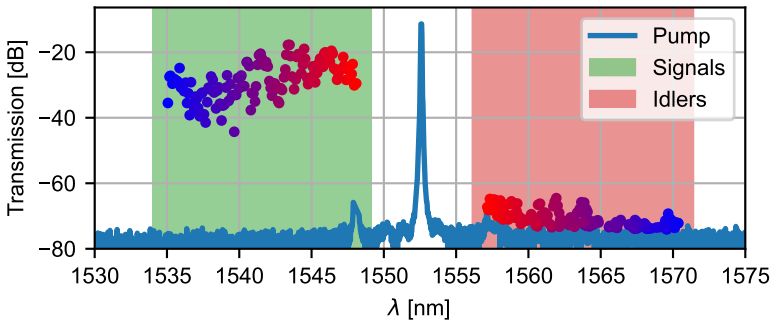

(a)

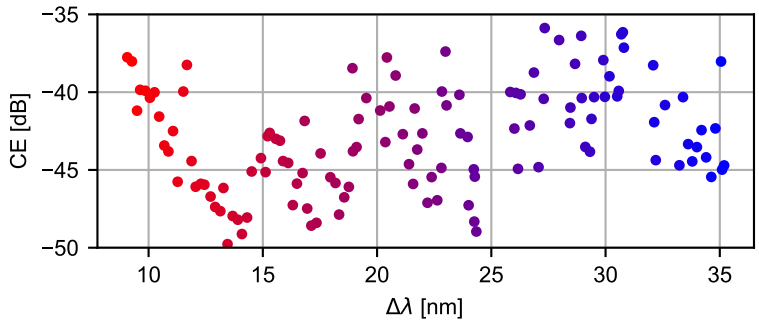

(b)

Figure 5.24: Data for a FWM process in a time-lens circuit based on SBGs with no pump filtering. λ_{pump} is 1552.6 nm. **(a)** Sweep of the signal detuning, with the signal and idler at each wavelength shown in matching colors. **(b)** CE for the data shown in **(a)**.

with coupling carried out using Y-branches. The CE in this case is comparable, but magnitude of the generated idler is 5 to 10 dB lower, which we believe is due to the extra losses incurred due to this way of implementing the time-lens circuit. In fact, the average power of the generated idlers for the CABG based circuit is 6.1 dB higher than the average power of the generated idlers of the multi mode CBG based circuit, which leads us to believe that the main source of additional

loss in the multi mode CBG based circuit is that the reflection is accessed using Y-branches and that the total propagation losses for the two circuits are similar. Inspecting the figures, it is also seen that the measured signal powers are lower for the second case, but it must be remembered that the signal is measured after propagation through the full circuit. Reiterating, we were never able to achieve measurable FWM using circuits based on single mode CBGs although several have been implemented and were tested. Although it is a shame that we have not been able to implement a time lens based on any of these circuits, we believe that the fact that the generated idler was significantly larger in the circuit using ABGs and MMCs, demonstrates the utility of this approach. The fact that we were not able to generate and idler when using a single moded CBG also demonstrates that the losses are indeed lower in a multi moded CBG and fig. 5.22 shows that the required dispersion is generated by the multi moded CBG.

5.4 Discussion

The first chip we tested was designed to test the performance of thin Si waveguides and experimentally verify the performance of CBBGs. The small variations in height on a thin Si circuit was not investigated during the simulation phase and resulted in large shifts in the Bragg wavelength of the included BGs. If one had access to the Si height in the area of the wafer, this problem could be overcome in the design phase, but an additional issue stemming from this fact was that it led to the introduction of distortions to the response of the SBGs, which is a problem that is harder to overcome, since it depends on the local height variations. We also could not directly measure the loss of the platform, but the waveguides generally had low insertion loss, going as low as 5.33 dB for a 1 cm long device including the coupling loss. We were able to verify the utility of CBBGs as pump filters with a circuit that reached an extinction loss of 50 dB.

On our second chip, we tested MMCs and access to the reflection from ABGs using MMCs, which was a success. An MMC that performed in accordance with results gained from simulation was demonstrated here and we also demonstrated its utility in accessing the reflection from an ABG.

On our third chip, we tested more CBBGs. When varying the number of individual ABGs in the CBBG, they performed as we would expect, but when changing the corrugation depth of the gratings, we saw a

wavelength shift that increased with the corrugation depth. We do not understand the mechanism that results in this effect yet, but we were able to recreate the magnitude of the wavelength shift using simulations and until we have a better understanding of this shift, we can compensate for the shift using these simulations. We have also designed circuits for implementing a time-lens. Unfortunately the linear losses were too large to achieve more than FWM with a CW laser. FWM experiments on two circuits, one based on CABGs and MMCs and the other based on CBGs in multi moded waveguides did serve as a demonstration of the reduced losses experienced in the former, most likely due to using MMCs as couplers.

A fourth chip was designed for the LioniX ADS platform and was intended to test this platform for dispersion generation using very long CBGs and to further demonstrate CBBGs in a platform with ultra low losses. The longest CBG on this chip will be 63 cm long and have a chirp bandwidth of 10 nm, which will lead to a dispersion of $D_2 = 1000$ ps/nm, which would be record breaking both in terms of the magnitude of D_2 and the maximal group delay created. Due to the length of this grating, we expect band edge effects due to the apodization to be almost completely removed. Due to the low losses of the platform we also hope to get a better signal to noise ratio when measuring the group delay and get more consistent results in these measurements.

As an overall conclusion on the experimental part, we have seen the utility of CBBGs as filters and the reduction in loss that can be achieved by using MMCs to access reflection from CABGs. We must also conclude that SOI simply has too high losses to implement even a demonstration version of an integrated time-lens. On the other hand, local fabrication of SOI circuits have a short turnaround time, allowing us to develop more chips and do more testing than would have otherwise been possible. Depending on the results from the SiN chip, we will be investigating the possibility of heterogeneous integration with SiN as the passive layer and AlGaAs as the active layer. This will most likely be done using micro transfer printing, which introduces a new set of challenges. One challenge will be achieving efficient coupling between layers and another will be access to the expertise needed to carry out the micro transfer printing itself.

6 Conclusion

The motivation for this project, as stated in chapter 1, is to reduce the energy consumption of the widely used TDM-PON, which is an optical communication network for transmitting data from a single CO to many ONUs. Due to the way power is split in a TDM-PON, losses that scale with the number of ONUs is introduced in this type of network. A different approach based on WDM signals exists which removes this splitting loss, but currently a WDM-PON requires a laser for each ONU, each of which has a power consumption overhead which removes the gains achieved by removing the splitting loss. We instead propose using a Lens-PON. Here a TDM transmitter is used at the CO and the TDM signal is converted to a WDM signal using an OFT based on a time lens. That this method works has been demonstrated by researchers in our group, but this has always been fully or mostly fiber based. If an OFT could be photonically integrated, Lens-PONs would become significantly more feasible due to reduced size and energy consumption. The goal of this project then, was to investigate how to integrate an OFT in a photonic circuit. In chapter 2, we introduced the elements that can be used to integrate the necessary components: namely dispersion generators based on CBGs, FWM waveguides and high performance BSFs. Since the magnitude of the generated dispersion controls the frequency spacing of the WDM signal generated from a TDM signal by an OFT, the achievable frequency spacing depends on the loss of the platform used. This means that only platforms with exceedingly low loss such as SiN are viable platforms for creating an integrated Lens-PON that can function with existing optical networks, but the SOI platform remains useful for conceptual demonstrations, with larger WDM frequency spacing. Correspondingly, the effectiveness of FWM waveguides is mostly a matter of choice of platform. Finally we saw that CBBGs can be used as flexible and powerful BSFs. In chapter 3, we expanded this by introducing novel ideas for how to reduce the loss of these components and for how to more efficiently access the dispersed light generated by CBGs, by using CABGs in conjunction with MMCs instead. This can potentially lead to a loss reduction of 6 dB compared to a more conventional approach, which is a significant improvement, that would lead to a corresponding 6 dB increase in the generated idler.

Another avenue for reducing loss explored here, was to base waveguides on waveguides with a high aspect ratio and potentially allowing the waveguides to be multimoded, to let the waveguide mode interface less with the sidewall corrugations. The loss reduction from this should also be significant, but the specific gain expected cannot be numerically ascribed as with the improvement in reflection access. Chapter 4 concerned the framework that was created for simulating and implementing the different elements developed during the project. This framework makes it simple to simulate and design PICs for different platforms with minimal inconvenience. Finally, in chapter 5, we presented the results gained from the different chips that were designed, fabricated and tested over the course of this project. The first chip we designed was based on a thin Si platform, to achieve waveguides with high aspect ratio and reduce losses. Unfortunately, we cannot directly conclude on how much this reduced loss and in the end, the high aspect ratio led to the BG response of the waveguides in this chip to become extremely sensitive to changes in Si height. On this chip, we also tested CBBGs and showed one CBBG with a rejection ratio exceeding 50 dB and a very sharp filter edge with a roll-off of 44 dB/nm. This CBBG was integrated along with a waveguide for FWM and we successfully demonstrated how this can be used to efficiently filter the FWM pump out. The second chip we was on a SiN on LNOI platform. Here we demonstrated a MMC with a SR of 15 dB and additionally showed how it could be used to access the light reflected from an ABG with losses as low as 1 dB. In the final chip we tested, we further investigated CBBGs and showed a filter with a rejection ratio of 60 dB. We also designed circuits for time-lensing. Unfortunately, the losses of the circuits were too large to implement a time lens, but through FWM we were able to demonstrate that the use of multi moded CBGs reduces the waveguide loss and that the use of CABGs where the reflection access was done with MMCs leads to the expected increase in performance.

Going forwards, we intend to further investigate different platforms for integration. If the chip that has been designed in SiN performs as expected, with very low losses, the next step would be to integrate a time-lens circuit in a SiN platform. Although the nonlinear parameter of this is lower than both SOI and AlGaAs, the lower losses might balance this out if the pump power is very high, e.g. above 1 W, and still allow for demonstration of a fully integrated OFT. Further ahead, we want to investigate the possibility of heterogeneous integration. Ide-

ally, this would be a chip where the linear components (the dispersion generators and BSFs) are fabricated in SiN and a FWM waveguide is fabricated in AlGaAs, as this would allow for generating large dispersion and achieving high conversion efficiency in the FWM process.

A Maxwells equations in dielectric media

This appendix is dedicated to outlining the basics of the theoretical foundation used througout the thesis. The reader is assumed to already have a deep understanding of all this, so this is not so much about educating the reader, but to introduce the notation and terminology that will be used in order to avoid confusion[1]. This whole thesis is of course based on Maxwell's Equations[79] are:

$$\nabla \times \mathbf{E} + \frac{\partial \mathbf{B}}{\partial t} = 0, \tag{A.1}$$

$$\nabla \times \mathbf{H} - \frac{\partial \mathbf{D}}{\partial t} = \mathbf{J}, \tag{A.2}$$

$$\nabla \cdot \mathbf{D} = \rho, \tag{A.3}$$

$$\nabla \cdot \mathbf{B} = 0, \tag{A.4}$$

with bold script denoting a vectorial quantity. As we know these four equations describe how electric and magnetic field vectors, **E** and **H**, are generated through free charges, ρ, currents, **J**, and from changes in the fields themselves. The field vectors **D** and **B** are the electric displacement and magnetic induction, respectively, and describe how the electric and magnetic fields are modified by the presence of matter. These are related to the electric and magnetic fields by the constitutive relations[10]:

$$\mathbf{D} = \epsilon_0 \mathbf{E} + \mathbf{P} \tag{A.5}$$

$$\mathbf{B} = \mu_0 \mathbf{H} + \mathbf{M}, \tag{A.6}$$

where ϵ_0 and μ_0 is the vacuum permittivity and permeability and **P** and **M** are the induced electric and magnetic polarization. Equations (A.1) to (A.4) can be decoupled such that we can directly relate the electric field and the induced polarization to each other:

$$\nabla \times \nabla \times \mathbf{E} = -\frac{1}{c^2}\frac{\partial^2 \mathbf{E}}{\partial t^2} - \mu_0 \frac{\partial^2 \mathbf{P}}{\partial t^2}, \tag{A.7}$$

[1] Additionally: it also just feels *right* to include Maxwell's equations in a PhD Thesis on photonics.

where $c^2 = 1/\mu_0\epsilon_0$ is the speed of light in vacuum. If we assume that no free charges are present, which is most often the case in the situations we will cover, we can use the definition:

$$\nabla \times \nabla \times \mathbf{E} \equiv \nabla(\nabla \cdot \mathbf{E}) - \nabla^2\mathbf{E} = -\nabla^2\mathbf{E}, \tag{A.8}$$

since $\nabla \cdot \mathbf{E} = 0$ when no free charges are present. This gives us:

$$\nabla^2\mathbf{E} = \frac{1}{c^2}\frac{\partial^2\mathbf{E}}{\partial t^2} + \mu_0\frac{\partial^2\mathbf{P}}{\partial t^2} \tag{A.9}$$

Equation (A.9) describes the propagation of electro-magnetic waves in a given medium, but in order to use this, we need a way to describe how the electrical polarization, **P**, is related to the electric field, **E**. A full description for a given medium is not an easy task since this depends on how electrons are bound in the atoms of the medium and would require a full quantum mechanical treatment. This is generally not feasible so instead the relationship is typically expressed as a power series in **E**[80]:

$$\mathbf{P} = \epsilon_0\left(\chi^{(1)} \cdot \mathbf{E} + \chi^{(2)} : \mathbf{EE} + \chi^{(3)} \vdots \mathbf{EEE} + \cdots\right) \tag{A.10}$$

$$= \mathbf{P}^{(1)} + \mathbf{P}^{(2)} + \mathbf{P}^{(3)} + \cdots \tag{A.11}$$

Here the susceptibilities $\chi^{(i)}$ are tensors of i^{th} order and describes interactions between the electric field and the medium of different orders and $\mathbf{P}^{(i)}$ is the i^{th} order polarization. Since this eq. (A.10) is a power series in **E** we can see that the nonlinear terms will be negligible for small field field strengths and only become important as the field strength is increased, with the threshold determined by the relevant susceptibility. The $\chi^{(1)}$ term describes the usual linear interaction between the field and the material where no new frequencies can be created as the electrons are bound to the atoms of the material as a harmonic oscillator to a good approximation. For the linear term we have:

$$\epsilon = \left(1 + \chi^{(1)}\right)\epsilon_0, \tag{A.12}$$

which can also be related to the refractive index of a medium (in the case of non-magnetic media) as:

$$n^2 = \frac{\epsilon}{\epsilon_0}. \tag{A.13}$$

Returning to the polarization, if we use eq. (A.12), we can write it as:

$$\mathbf{P} = (\epsilon - \epsilon_0)\,\mathbf{E}, \tag{A.14}$$

in the linear regime. Inserting this into eq. (A.9), we arrive at the wave equation for propagation in a linear medium:

$$\nabla^2 \mathbf{E} = \epsilon\mu_0 \frac{\partial^2 \mathbf{E}}{\partial t^2} \tag{A.15}$$

As we leave the linear medium with increasing field strengths, the higher terms in eq. (A.10) starts to matter more, but all effects are not always present. Second order effects that are described by $\chi^{(2)}$ require the material to be non-centrosymmetric which is only the case for certain materials such as specific crystals like Lithium niobate ($LiNbO_3$) or otherwise centrosymmetric materials under strain. Second order effects include the electro-optic (or Pockels) effect where a change in the refractive index of a material becomes proportional to the applied electric field, which is used to make electro-optic modulators (EOMs), and second-harmonic generation which leads to the creation of an electric field at double the frequency of the input field.

Third order effects are not dependent on the specific symmetries of the material and are present in any material to varying degrees with the strength of the effect described by its $\chi^{(3)}$. One third order effect is that the refractive index of the material will depend on the intensity of the field. This means that if a field propagating through the medium has a large enough intensity it will change the refractive index as it is propagating which leads to a modulation of its own phase - self phase modulation (SPM) - and to phase modulation of any co-propagating field - cross phase modulation (XPM). Of special important to us is the case of four-wave mixing (FWM). As the name indicates, the $\chi^{(3)}$ nonlinearity allows four fields oscillating at the frequencies $\omega_1, \omega_2, \omega_3$ and ω_4 to interact. If we assume that the four fields are co-polarized, we can write the electric field as:

$$\mathbf{E} = \frac{1}{2}\sum_{j=1}^{N} E_j e^{i(\omega_j t - \beta_j z)}. \tag{A.16}$$

If we insert this into eq. (A.10), we can see that we will get a large amount of terms due to the triple product of the field with itself, with full polarization on the form:

$$\mathbf{P}^{(3)} = \frac{1}{2}\sum_{j=1}^{N} P_j e^{i(\omega_j t - \beta_j z)}. \tag{A.17}$$

Following Agrawal[10], we see that P_4 is:

$$\begin{aligned} P_4 =& \frac{3\epsilon_0}{4}\chi^{(3)}\left[|E_4|^2E_4 + 2\left(|E_1|^2 + |E_2|^2 + |E_3|^2\right)E_4\right. \\ &\left. + 2E_1E_2E_3e^{i\theta_+} + 2E_1E_2E_3^*e^{i\theta_-} + \cdots\right], \end{aligned} \tag{A.18}$$

with

$$\theta_+ = (\beta_1 + \beta_2 + \beta_3 - \beta_4)\,z - (\omega_1 + \omega_2 + \omega_3 - \omega_4)\,t \tag{A.19}$$

$$\theta_- = (\beta_1 + \beta_2 - \beta_3 - \beta_4)\,z - (\omega_1 + \omega_2 - \omega_3 - \omega_4)\,t. \tag{A.20}$$

In eq. (A.18), on the first line the first term corresponds to SPM and the next three terms correspond to XPM between E_4 and the other input fields. The following terms are all oscillating at frequencies that are the possible sums and differences between the input fields and are the terms describing FWM and other effects like third harmonic generation. Significant effects of these types will only occur for a term if the phase mismatch between E_4 and P_4 is close to zero, which is governed by the different θ terms. For FWM these phase terms are of the form θ_-, which corresponds to the case where:

$$\omega_3 + \omega_4 = \omega_1 + \omega_2. \tag{A.21}$$

Specifically, we will be interested in the case of degenerate FWM, where:

$$\omega_1 = \omega_2 = \omega_p. \tag{A.22}$$

Here what will one of the input fields in a FWM process has been indexed p for "pump". The other two fields in the process are traditionally called the signal (s) and idler (i) field, where the the phase matching condition in this case amounts to:

$$\Delta k = 0 \quad \text{or} \tag{A.23}$$

$$\Delta\beta = 2\beta_p - \beta_i - \beta_s = 0, \tag{A.24}$$

which in the case where the input is the pump and signal results in the creation of a field oscillating at the frequency:

$$\omega_i = \omega_p + \Delta\omega, \tag{A.25}$$

where $\Delta\omega = \omega_p - \omega_s$. In this degenerate case, the idler field can be expressed as:

$$E_i(\omega_i, t) = \eta E_p^2(\omega_p, t)E_s^*(\omega_s, t), \tag{A.26}$$

where η is the conversion efficiency. The conversion efficiency is proportional to the nonlinear parameter:

$$\gamma_i = \frac{n_2 \omega}{c A_{\text{eff}}} \tag{A.27}$$

Here n_2 is the Kerr nonlinear index, which modifies the refractive index of a material through:

$$\tilde{n} = n + n_2 |E|^2, \tag{A.28}$$

and is defined as:

$$n_2 = \frac{3}{8n} \text{Re}\left\{\chi^{(3)}\right\}. \tag{A.29}$$

A_{eff} is the effective area of a mode:

$$\frac{1}{A_{\text{eff}}} = \frac{\int_{-\infty}^{\infty} \int_{-\infty}^{\infty} |F(x,y)|^4 dxdy}{\left(\int_{-\infty}^{\infty} \int_{-\infty}^{\infty} |F(x,y)|^2 dxdy)\right)^2}. \tag{A.30}$$

So in short, the conversion efficiency is determined by the nonlinearity of the material and the effective area of the mode as might be expected.

B Coupling between counter propagating modes

Coupling between the forward propagating mode with the envelope A and backward propagating mode with the envelope B, as described in section 2.1.1, have their envelopes related by the differential equations:

$$\frac{dA}{dz} = \kappa_{ab} B e^{-i\Delta z} \tag{B.1a}$$

$$\frac{dB}{dz} = \kappa_{ba} A e^{i\Delta z}. \tag{B.1b}$$

In order to find expressions for $A(z)$ and $B(z)$, we start by differentiating both equations:

$$\frac{d^2A}{dz^2} = \kappa \frac{dB}{dz} e^{-i\Delta z} - i\Delta\kappa B e^{-i\Delta z} \tag{B.2a}$$

$$\frac{d^2A}{dz^2} = \kappa \frac{dA}{dz} e^{i\Delta z} + i\Delta\kappa A e^{i\Delta z}. \tag{B.2b}$$

Now we can isolate B in eq. (B.1a) and insert this in eq. (B.2a) along with eq. (B.1b) and rearrange:

$$\frac{d^2A}{dz^2} + i\delta\frac{dA}{dz} - \kappa^2 A = 0. \tag{B.3}$$

The characteristic polynomium of eq. (B.3) has roots:

$$\lambda = -\frac{i\Delta}{2} \pm \frac{S}{2}, \tag{B.4}$$

which gives us a solution for A:

$$A(z) = e^{Sz/2}\left[c_1 e^{i\Delta z/2} + c_2 e^{-i\Delta z/2}\right], \tag{B.5}$$

where

$$S = \sqrt{4\kappa^2 - \Delta}. \tag{B.6}$$

We assume that the incident field at $z = 0$ has an amplitude of $B(0) = B_0$ and since the perturbation of the waveguide ends at $z = L$, the

amplitude of A will be $A(L) = 0$. Using the second of these boundary conditions we get:

$$A(L) = e^{SL/2}\left[c_1 e^{i\Delta L/2} + c_2 e^{-i\Delta L/2}\right] = 0 \tag{B.7}$$

$$\Rightarrow c_1 = -c_2 e^{-i\Delta L}, \tag{B.8}$$

which gives us:

$$A(z) = -2c_2 e^{-i\Delta z/2} e^{-SL/2} \sinh\left[\frac{S}{2}(z-L)\right], \tag{B.9}$$

which has the derivative:

$$\begin{aligned}\frac{dA}{dz} =& -c_2 i e^{-SL/2} e^{i\Delta z/2} \\ &\cdot \left\{iS\cosh\left[\frac{S}{2}(z-L)\right] - \Delta \sinh\left[\frac{S}{2}(z-L)\right]\right\}.\end{aligned} \tag{B.10}$$

Along with the first boundary condition, this can be inserted into eq. (B.1a):

$$\left.\frac{dA}{dz}\right|_{z=0} = \kappa B_0, \tag{B.11}$$

from which we can isolate c_2:

$$c_2 = e^{SL/2} \frac{\kappa B_0}{i\Delta \sinh\left[\frac{SL}{2}\right] - S\cosh\left[\frac{SL}{2}\right]}, \tag{B.12}$$

and arrive at a result for A:

$$A(z) = 2\kappa B_0 e^{-i\Delta z/2} \frac{\sinh\left[\frac{S}{2}(z-L)\right]}{i\Delta \sinh\left[\frac{SL}{2}\right] - S\cosh\left[\frac{SL}{2}\right]}. \tag{B.13}$$

Inserting the result for c_2 into eq. (B.10), we get:

$$\frac{dA}{dz} = \kappa B_0 e^{i\Delta z/2} \frac{\Delta \sinh\left[\frac{S}{2}(z-L)\right] - iS\cosh\left[\frac{S}{2}(z-L)\right]}{i\Delta \sinh\left[\frac{SL}{2}\right] - S\cosh\left[\frac{SL}{2}\right]}. \tag{B.14}$$

Inserting eq. (B.14) into eq. (B.1a) and isolating for B, we get:

$$B(z) = iB_0 e^{i\Delta z/2} \frac{\Delta \sinh\left[\frac{S}{2}(z-L)\right] - iS\cosh\left[\frac{S}{2}(z-L)\right]}{i\Delta \sinh\left[\frac{SL}{2}\right] - S\cosh\left[\frac{SL}{2}\right]}, \tag{B.15}$$

which along with eq. (B.13) fully describes the exchange of power between the two modes.

Acronyms

ABG	Asymmetric Bragg Grating.
ADS	Asymmetric Double Stripe.
AlGaAs	$Al_xGa_{1-x}As$.
AlGaAs-OI	AlGaAs-On-Isolator.
AWG	Arrayed Waveguide Grating.
BG	Bragg Grating.
BMMC	Broadband Multi-Mode Coupler.
BSF	Band Stop Filter.
c-Si	crystalline Silicon.
CABG	Chirped Asymmetric Bragg Grating.
CBBG	Coherency Broken Bragg Grating.
CBG	Chirped Bragg Grating.
CE	Conversion Efficiency.
CMOS	Complimentary Metal–Oxide–Semiconductor.
CMT	Coupled-Mode Theory.
CO	Central Office.
CW	Continuous Wave.
DCF	Dispersion Compensation Fiber.
EMA	Effective Mode Area.
EME	Eigenmode Expansion Method.
EOM	Electro-Optic Modulator.
FDE	Finite Difference Eigenmode.
FDTD	Finite Difference Time Domain.
FOM	Figure Of Merit.
FWM	Four-Wave Mixing.
GDD	Group Delay Dispersion.
GVD	Group Velocity Dispersion.
ICT	Internet and Communications Technology.

Lens-PONs	Time-Lens Passive Optical Network.
LN	Lithium Niobate.
LNOI	Lithium Niobate On Isolator.
MMC	Multi-Mode Coupler.
MMI	Multi-Mode Interferometer.
OFT	Optical Fourier Transform.
ONU	Optical Network Unit.
PIC	Photonic Integrated Circuits.
PON	Passive Optical Networks.
SABG	Spiral Asymmetric Bragg Grating.
SBG	Spiral Bragg Grating.
SCABG	Spiral Chirped Asymmetric Bragg Grating.
SCBG	Spiral Chirped Bragg Grating.
SiN	Si_3N_4.
SMF	Single Mode Fiber.
SOI	Silicon-On-Insulator.
SR	Splitting Ratio.
TDM	Time Division Multiplexing.
TMM	Transfer Matrix Modelling.
TOD	Third Order Dispersion.
TPA	Two Photon Absorption.
WDM	Wavelength Division Multiplexing.
XPM	Cross Phase Modulation.

Bibliography

[1] Cisco. “Cisco Annual Internet Report - Cisco Annual Internet Report (2018–2023) White Paper”. In: (). URL: https://www.cisco.com/c/en/us/solutions/collateral/executive-perspectives/annual-internet-report/white-paper-c11-741490.html.

[2] Thomas Barnett et al. “Cisco Visual Networking Index (VNI) Complete Forecast Update, 2017–2022 Americas/EMEAR Cisco Knowledge Network (CKN) Presentation”. In: *Americas/EMEAR Cisco Knowledge Network (CKN) Presentation* (2018). URL: https://get.drivenets.com/hubfs/1211_BUSINESS_SERVICES_CKN_PDF.pdf.

[3] Ognjen Jovanovic et al. “End-to-End Learning of a Constellation Shape Robust to Channel Condition Uncertainties”. In: *Journal of Lightwave Technology* 40.10 (May 2022). Conference Name: Journal of Lightwave Technology, pp. 3316–3324. ISSN: 1558-2213. DOI: 10.1109/JLT.2022.3169993.

[4] D. Kong et al. “Single Dark-Pulse Kerr Comb Supporting 1.84 Pbit/s Transmission over 37-Core Fiber”. In: *Conference on Lasers and Electro-Optics (2020), paper JTh4A.7*. CLEO: QELS_Fundamental Science. Optica Publishing Group, May 10, 2020, JTh4A.7. DOI: 10.1364/CLEO_AT.2020.JTh4A.7. URL: https://opg.optica.org/abstract.cfm?uri=CLEO_QELS-2020-JTh4A.7.

[5] Anders S. G. Andrae and Tomas Edler. “On Global Electricity Usage of Communication Technology: Trends to 2030”. In: *Challenges* 6.1 (June 2015). Number: 1 Publisher: Multidisciplinary Digital Publishing Institute, pp. 117–157. ISSN: 2078-1547. DOI: 10.3390/challe6010117. URL: https://www.mdpi.com/2078-1547/6/1/117.

[6] Ivica Cale, Aida Salihovic, and Matija Ivekovic. “Gigabit Passive Optical Network - GPON”. In: *2007 29th International Conference on Information Technology Interfaces*. 2007 29th International Conference on Information Technology Interfaces. ISSN: 1330-1012. June 2007, pp. 679–684. DOI: 10.1109/ITI.2007.4283853.

[7] B.H. Kolner. “Space-time duality and the theory of temporal imaging”. In: *IEEE Journal of Quantum Electronics* 30.8 (Aug. 1994). Conference Name: IEEE Journal of Quantum Electronics, pp. 1951–1963. ISSN: 1558-1713. DOI: 10.1109/3.301659.

[8] Reza Salem, Mark A. Foster, and Alexander L. Gaeta. “Application of space–time duality to ultrahigh-speed optical signal processing”. In: *Advances in Optics and Photonics* 5.3 (Sept. 30, 2013), p. 274. ISSN: 1943-8206. DOI: 10.1364/AOP.5.000274. URL: https://opg.optica.org/aop/abstract.cfm?uri=aop-5-3-274.

[9] J. Azana and M.A. Muriel. “Real-time optical spectrum analysis based on the time-space duality in chirped fiber gratings”. In: *IEEE Journal of Quantum Electronics* 36.5 (May 2000). Conference Name: IEEE Journal of Quantum Electronics, pp. 517–526. ISSN: 1558-1713. DOI: 10.1109/3.842092.

[10] G. P. Agrawal. *Nonlinear fiber optics*. Fifth edition. Amsterdam: Elsevier/Academic Press, 2013. 629 pp. ISBN: 978-0-12-397023-7.

[11] Evarist Palushani et al. “OTDM-to-WDM Conversion Based on Time-to-Frequency Mapping by Time-Domain Optical Fourier Transformation”. In: *IEEE Journal of Selected Topics in Quantum Electronics* 18.2 (Mar. 2012). Conference Name: IEEE Journal of Selected Topics in Quantum Electronics, pp. 681–688. ISSN: 1558-4542. DOI: 10.1109/JSTQE.2011.2131121.

[12] “Chapter 2”. In: Amnon Yariv, Pochi Yeh, and Amnon Yariv. *Photonics: optical electronics in modern communications*. 6th ed. The Oxford series in electrical and computer engineering. OCLC: ocm58648003. New York: Oxford University Press, 2007, pp. 66–109. ISBN: 978-0-19-517946-0.

[13] X. Xu et al. “The Impact of Higher Order Dispersion in a Time Lens based WDM Transmitter”. In: *Conference on Lasers and Electro-Optics*. CLEO: Science and Innovations. Washington, DC: Optica Publishing Group, 2020, STh3L.4. ISBN: 978-1-943580-76-7. DOI: 10.1364/CLEO_SI.2020.STh3L.4. URL: https://opg.optica.org/abstract.cfm?URI=CLEO_SI-2020-STh3L.4.

[14] Brian H. Kolner and Moshe Nazarathy. “Temporal imaging with a time lens”. In: *Optics Letters* 14.12 (June 15, 1989), p. 630. ISSN: 0146-9592, 1539-4794. DOI: 10.1364/OL.14.000630. URL: https://opg.optica.org/abstract.cfm?URI=ol-14-12-630.

[15] Mengjie Yu et al. “Integrated femtosecond pulse generator on thin-film lithium niobate”. In: *Nature* 612.7939 (Dec. 2022). Number: 7939 Publisher: Nature Publishing Group, pp. 252–258. ISSN: 1476-4687. DOI: 10.1038/s41586-022-05345-1. URL: https://www.nature.com/articles/s41586-022-05345-1.

[16] Mark A. Foster et al. “Silicon-chip-based ultrafast optical oscilloscope”. In: *Nature* 456.7218 (Nov. 2008). Number: 7218 Publisher: Nature Publishing Group, pp. 81–84. ISSN: 1476-4687. DOI: 10.1038/nature07430. URL: https://www.nature.com/articles/nature07430.

[17] Evarist Palushani et al. “Flat-Top Pulse Generation by the Optical Fourier Transform Technique for Ultrahigh Speed Signal Processing”. In: *IEEE Journal of Quantum Electronics* 45.11 (Nov. 2009). Conference Name: IEEE Journal of Quantum Electronics, pp. 1317–1324. ISSN: 1558-1713. DOI: 10.1109/JQE.2009.2028586.

[18] P. Guan et al. “Highly Flexible WDM PON System with a Single TDM Time Lens Source Enabling Record 150 km Downstream Reach”. In: *Optical Fiber Communication Conference*. Optical Fiber Communication Conference. San Diego, California: OSA, 2018, Th2A.54. ISBN:

978-1-943580-38-5. DOI: 10.1364/OFC.2018.Th2A.54. URL: https://opg.optica.org/abstract.cfm?URI=OFC-2018-Th2A.54.

[19] Pengyu Guan et al. “Simultaneous 256 WDM Channel Generation using a Single AlGaAsOI Waveguide based Time Lens Source”. In: *45th European Conference on Optical Communication (ECOC 2019)*. 45th European Conference on Optical Communication (ECOC 2019). Dublin, Ireland: Institution of Engineering and Technology, 2019, 6 (4 pp.)–6 (4 pp.) ISBN: 978-1-83953-185-9. DOI: 10.1049/cp.2019.0740. URL: https://digital-library.theiet.org/content/conferences/10.1049/cp.2019.0740.

[20] X. Xu et al. “28 Channel PAM4 WDM Transmitter based on a Single Time Lens Source”. In: *Asia Communications and Photonics Conference/International Conference on Information Photonics and Optical Communications 2020 (ACP/IPOC)*. Asia Communications and Photonics Conference. Beijing: Optica Publishing Group, 2020, T2B.4. ISBN: 978-1-943580-82-8. DOI: 10.1364/ACPC.2020.T2B.4. URL: https://opg.optica.org/abstract.cfm?URI=ACPC-2020-T2B.4.

[21] Xiaoyu Xu et al. “Simultaneous Generation of 16×10 Gb/s WDM Channels Using a Single a-Si Waveguide based Time Lens Source”. In: *Optical Fiber Communication Conference (OFC) 2021*. Optical Fiber Communication Conference. Washington, DC: Optica Publishing Group, 2021, F2E.7. ISBN: 978-1-943580-86-6. DOI: 10.1364/OFC.2021.F2E.7. URL: https://opg.optica.org/abstract.cfm?URI=OFC-2021-F2E.7.

[22] “Chapter 5”. In: K. Thyagarajan and A. K. Ghatak. *The fiber optic essentials*. Wiley survival guides in engineering and science. [Piscataway, N.J.] : Hoboken, N.J: IEEE Press ; Wiley-Interscience, 2007, pp. 55–69. ISBN: 978-0-470-09742-7.

[23] Tak-Keung Liang and Hon-Ki Tsang. “Nonlinear absorption and Raman scattering in silicon-on-insulator optical waveguides”. In: *IEEE Journal of Selected Topics in Quantum Electronics* 10.5 (Sept. 2004). Conference Name: IEEE Journal of Selected Topics in Quantum Electronics, pp. 1149–1153. ISSN: 1558-4542. DOI: 10.1109/JSTQE.2004.835290.

[24] David J. Moss et al. “New CMOS-compatible platforms based on silicon nitride and Hydex for nonlinear optics”. In: *Nature Photonics* 7.8 (Aug. 2013). Number: 8 Publisher: Nature Publishing Group, pp. 597–607. ISSN: 1749-4893. DOI: 10.1038/nphoton.2013.183. URL: https://www.nature.com/articles/nphoton.2013.183.

[25] D Melati, F Morichetti, and A Melloni. “A unified approach for radiative losses and backscattering in optical waveguides”. In: *Journal of Optics* 16.5 (May 1, 2014), p. 055502. ISSN: 2040-8978, 2040-8986. DOI: 10.1088/2040-8978/16/5/055502. URL: https://iopscience.iop.org/article/10.1088/2040-8978/16/5/055502.

[26] T. K. Liang and H. K. Tsang. “Role of free carriers from two-photon absorption in Raman amplification in silicon-on-insulator waveguides”. In: *Applied Physics Letters* 84.15 (Apr. 12, 2004), pp. 2745–2747.

ISSN: 0003-6951, 1077-3118. DOI: 10.1063/1.1702133. URL: http://aip.scitation.org/doi/10.1063/1.1702133.

[27] Alan D. Bristow, Nir Rotenberg, and Henry M. van Driel. "Two-photon absorption and Kerr coefficients of silicon for 850–2200nm". In: *Applied Physics Letters* 90.19 (May 7, 2007). Publisher: American Institute of Physics, p. 191104. ISSN: 0003-6951. DOI: 10.1063/1.2737359. URL: https://aip.scitation.org/doi/full/10.1063/1.2737359.

[28] C. Grillet et al. "Amorphous silicon nanowires combining high nonlinearity, FOM and optical stability". In: *Optics Express* 20.20 (Sept. 24, 2012). Publisher: Optica Publishing Group, pp. 22609–22615. ISSN: 1094-4087. DOI: 10.1364/OE.20.022609. URL: https://opg.optica.org/oe/abstract.cfm?uri=oe-20-20-22609.

[29] J. Leuthold, C. Koos, and W. Freude. "Nonlinear silicon photonics". In: *Nature Photonics* 4.8 (Aug. 2010). Number: 8 Publisher: Nature Publishing Group, pp. 535–544. ISSN: 1749-4893. DOI: 10.1038/nphoton.2010.185. URL: https://www.nature.com/articles/nphoton.2010.185.

[30] Xia Chen et al. "The Emergence of Silicon Photonics as a Flexible Technology Platform". In: *Proceedings of the IEEE* 106.12 (Dec. 2018). Conference Name: Proceedings of the IEEE, pp. 2101–2116. ISSN: 1558-2256. DOI: 10.1109/JPROC.2018.2854372.

[31] R. Halir et al. "Ultrabroadband supercontinuum generation in a CMOS-compatible platform". In: *Optics Letters* 37.10 (May 15, 2012). Publisher: Optica Publishing Group, pp. 1685–1687. ISSN: 1539-4794. DOI: 10.1364/OL.37.001685. URL: https://opg.optica.org/ol/abstract.cfm?uri=ol-37-10-1685.

[32] Chris G. H. Roeloffzen et al. "Low-Loss Si3N4 TriPleX Optical Waveguides: Technology and Applications Overview". In: *IEEE Journal of Selected Topics in Quantum Electronics* 24.4 (July 2018), pp. 1–21. ISSN: 1077-260X, 1558-4542. DOI: 10.1109/JSTQE.2018.2793945. URL: http://ieeexplore.ieee.org/document/8259277/.

[33] Minhao Pu et al. "Ultra-Efficient and Broadband Nonlinear AlGaAs-on-Insulator Chip for Low-Power Optical Signal Processing". In: *Laser & Photonics Reviews* 12.12 (2018). _eprint: https://onlinelibrary.wiley.com/doi/pdf/10.1002/lpor.201800111, p. 1800111. ISSN: 1863-8899. DOI: 10.1002/lpor.201800111. URL: https://onlinelibrary.wiley.com/doi/abs/10.1002/lpor.201800111.

[34] Jacob S. Levy et al. "CMOS-compatible multiple-wavelength oscillator for on-chip optical interconnects". In: *Nature Photonics* 4.1 (Jan. 2010). Number: 1 Publisher: Nature Publishing Group, pp. 37–40. ISSN: 1749-4893. DOI: 10.1038/nphoton.2009.259. URL: https://www.nature.com/articles/nphoton.2009.259.

[35] Mingxiao Li et al. "Lithium niobate photonic-crystal electro-optic modulator". In: *Nature Communications* 11.1 (Aug. 17, 2020). Number: 1 Publisher: Nature Publishing Group, p. 4123. ISSN: 2041-1723. DOI: 10.1038/s41467-020-17950-7. URL: https://www.nature.com/articles/s41467-020-17950-7.

[36] Di Zhu et al. “Integrated photonics on thin-film lithium niobate”. In: *Advances in Optics and Photonics* 13.2 (June 30, 2021). Publisher: Optica Publishing Group, pp. 242–352. ISSN: 1943-8206. DOI: 10.1364/AOP.411024. URL: https://opg.optica.org/aop/abstract.cfm?uri=aop-13-2-242.

[37] Andreas Boes et al. “Status and Potential of Lithium Niobate on Insulator (LNOI) for Photonic Integrated Circuits”. In: *Laser & Photonics Reviews* 12.4 (2018). _eprint: https://onlinelibrary.wiley.com/doi/pdf/10.1002/lpor.201700256, p. 1700256. ISSN: 1863-8899. DOI: 10.1002/lpor.201700256. URL: https://onlinelibrary.wiley.com/doi/abs/10.1002/lpor.201700256.

[38] Pu Zhang et al. “High-speed electro-optic modulator based on silicon nitride loaded lithium niobate on an insulator platform”. In: *Optics Letters* 46.23 (Dec. 1, 2021), p. 5986. ISSN: 0146-9592, 1539-4794. DOI: 10.1364/OL.446222. URL: https://opg.optica.org/abstract.cfm?URI=ol-46-23-5986.

[39] Xu Han et al. “Single-step etched grating couplers for silicon nitride loaded lithium niobate on insulator platform”. In: *APL Photonics* 6.8 (Aug. 9, 2021), p. 086108. ISSN: 2378-0967. DOI: 10.1063/5.0055213. URL: https://doi.org/10.1063/5.0055213.

[40] Xu Han et al. “Mode and Polarization-Division Multiplexing Based on Silicon Nitride Loaded Lithium Niobate on Insulator Platform”. In: *Laser & Photonics Reviews* 16.1 (2022). _eprint: https://onlinelibrary.wiley.com/doi/pdf/10.1002/lpor.202100529, p. 2100529. ISSN: 1863-8899. DOI: 10.1002/lpor.202100529. URL: https://onlinelibrary.wiley.com/doi/abs/10.1002/lpor.202100529.

[41] Yongheng Jiang et al. “Monolithic Photonic Integrated Circuit Based on Silicon Nitride and Lithium Niobate on Insulator Hybrid Platform”. In: *Advanced Photonics Research* 3.10 (2022). _eprint: https://onlinelibrary.wiley.com/doi/pdf/10.1002/adpr.202200121, p. 2200121. ISSN: 2699-9293. DOI: 10.1002/adpr.202200121. URL: https://onlinelibrary.wiley.com/doi/abs/10.1002/adpr.202200121.

[42] Cheng Wang et al. “Monolithic lithium niobate photonic circuits for Kerr frequency comb generation and modulation”. In: *Nature Communications* 10.1 (Feb. 28, 2019). Number: 1 Publisher: Nature Publishing Group, p. 978. ISSN: 2041-1723. DOI: 10.1038/s41467-019-08969-6. URL: https://www.nature.com/articles/s41467-019-08969-6.

[43] Luisa Ottaviano et al. “Low-loss high-confinement waveguides and microring resonators in AlGaAs-on-insulator”. In: *Optics Letters* 41.17 (Sept. 1, 2016). Publisher: Optica Publishing Group, pp. 3996–3999. ISSN: 1539-4794. DOI: 10.1364/OL.41.003996. URL: https://opg.optica.org/ol/abstract.cfm?uri=ol-41-17-3996.

[44] M. Savanier et al. “Large second-harmonic generation at 1.55 µmin oxidized AlGaAs waveguides”. In: *Optics Letters* 36.15 (Aug. 1, 2011). Publisher: Optica Publishing Group, pp. 2955–2957. ISSN: 1539-4794.

DOI: 10.1364/OL.36.002955. URL: https://opg.optica.org/ol/abstract.cfm?uri=ol-36-15-2955.

[45] Ksenia Dolgaleva et al. “Compact highly-nonlinear AlGaAs waveguides for efficient wavelength conversion”. In: *Optics Express* 19.13 (June 20, 2011). Publisher: Optica Publishing Group, pp. 12440–12455. ISSN: 1094-4087. DOI: 10.1364/OE.19.012440. URL: https://opg.optica.org/oe/abstract.cfm?uri=oe-19-13-12440.

[46] Ehsan Mobini et al. “AlGaAs Nonlinear Integrated Photonics”. In: *Micromachines* 13.7 (July 2022). Number: 7 Publisher: Multidisciplinary Digital Publishing Institute, p. 991. ISSN: 2072-666X. DOI: 10.3390/mi13070991. URL: https://www.mdpi.com/2072-666X/13/7/991.

[47] Stuart May, Matteo Clerici, and Marc Sorel. “Supercontinuum generation in dispersion engineered AlGaAs-on-insulator waveguides”. In: *Scientific Reports* 11.1 (Jan. 21, 2021). Number: 1 Publisher: Nature Publishing Group, p. 2052. ISSN: 2045-2322. DOI: 10.1038/s41598-021-81555-3. URL: https://www.nature.com/articles/s41598-021-81555-3.

[48] Pengyu Guan et al. “Time Lens-Based Optical Fourier Transformation for All-Optical Signal Processing of Spectrally-Efficient Data”. In: *Journal of Lightwave Technology* 35.4 (Feb. 15, 2017), pp. 799–806. ISSN: 0733-8724, 1558-2213. DOI: 10.1109/JLT.2016.2614186. URL: http://ieeexplore.ieee.org/document/7579624/.

[49] Zhenmin Du et al. “Silicon nitride chirped spiral Bragg grating with large group delay”. In: *APL Photonics* 5.10 (Oct. 1, 2020), p. 101302. ISSN: 2378-0967. DOI: 10.1063/5.0022963. URL: http://aip.scitation.org/doi/10.1063/5.0022963.

[50] K. Y. K. Ong et al. “Dispersion compensation of high-speed data using an integrated silicon nitride ring resonator”. In: *Optics Express* 30.9 (Apr. 25, 2022). Publisher: Optica Publishing Group, pp. 13959–13967. ISSN: 1094-4087. DOI: 10.1364/OE.451951. URL: https://opg.optica.org/oe/abstract.cfm?uri=oe-30-9-13959.

[51] Toshihiko Baba. “Slow light in photonic crystals”. In: *Nature Photonics* 2.8 (Aug. 2008). Number: 8 Publisher: Nature Publishing Group, pp. 465–473. ISSN: 1749-4893. DOI: 10.1038/nphoton.2008.146. URL: https://www.nature.com/articles/nphoton.2008.146.

[52] François Ouellette. “Dispersion cancellation using linearly chirped Bragg grating filters in optical waveguides”. In: *Optics Letters* 12.10 (Oct. 1, 1987), p. 847. ISSN: 0146-9592, 1539-4794. DOI: 10.1364/OL.12.000847. URL: https://opg.optica.org/abstract.cfm?URI=ol-12-10-847.

[53] Ivano Giuntoni et al. “Continuously tunable delay line based on SOI tapered Bragg gratings”. In: *Optics Express* 20.10 (May 7, 2012), p. 11241. ISSN: 1094-4087. DOI: 10.1364/OE.20.011241. URL: https://opg.optica.org/oe/abstract.cfm?uri=oe-20-10-11241.

[54] A. Yariv. “Coupled-mode theory for guided-wave optics”. In: *IEEE Journal of Quantum Electronics* 9.9 (Sept. 1973), pp. 919–933. ISSN:

0018-9197. DOI: 10.1109/JQE.1973.1077767. URL: http://ieeexplore.ieee.org/document/1077767/.

[55] Dorian Oser et al. “Coherency□Broken Bragg Filters: Overcoming On□Chip Rejection Limitations”. In: *Laser & Photonics Reviews* 13.8 (Aug. 2019), p. 1800226. ISSN: 1863-8880, 1863-8899. DOI: 10.1002/lpor.201800226. URL: https://onlinelibrary.wiley.com/doi/10.1002/lpor.201800226.

[56] Radek Helan. “Comparison of Methods for Fiber Bragg Gratings Simulation”. In: *2006 29th International Spring Seminar on Electronics Technology*. 2006 29th International Spring Seminar on Electronics Technology. St. Marienthal, Germany: IEEE, May 2006, pp. 161–166. ISBN: 978-1-4244-0550-3 978-1-4244-0551-0. DOI: 10.1109/ISSE.2006.365378. URL: http://ieeexplore.ieee.org/document/4216018/.

[57] I. Ashry et al. “Investigating the performance of apodized Fiber Bragg gratings for sensing applications”. In: *Proceedings of the 2014 Zone 1 Conference of the American Society for Engineering Education*. Proceedings of the 2014 Zone 1 Conference of the American Society for Engineering Education. Apr. 2014, pp. 1–5. DOI: 10.1109/ASEEZone1.2014.6820640.

[58] Huiye Qiu et al. “Silicon band-rejection and band-pass filter based on asymmetric Bragg sidewall gratings in a multimode waveguide”. In: *Optics Letters* 41.11 (June 1, 2016), p. 2450. ISSN: 0146-9592, 1539-4794. DOI: 10.1364/OL.41.002450. URL: https://opg.optica.org/abstract.cfm?URI=ol-41-11-2450.

[59] J.M. Castro, A. Sato, and D.F. Geraghty. “Waveguide mode conversion using anti-symmetric gratings”. In: *OFC/NFOEC Technical Digest. Optical Fiber Communication Conference, 2005.* 2005 Optical Fiber Communications Conference Technical Digest. Anaheim, CA, USA: IEEE, 2005, 3 pp. Vol. 1. ISBN: 978-1-55752-783-7. DOI: 10.1109/OFC.2005.192522. URL: http://ieeexplore.ieee.org/document/1497602/.

[60] Xu Wang. “Silicon Photonic Waveguide Bragg Gratings”. In: (), p. 182.

[61] Fengnian Xia et al. “Ultra-compact high order ring resonator filters using submicron silicon photonic wires for on-chip optical interconnects”. In: *Optics Express* 15.19 (2007), p. 11934. ISSN: 1094-4087. DOI: 10.1364/OE.15.011934. URL: https://opg.optica.org/oe/abstract.cfm?uri=oe-15-19-11934.

[62] K. Inoue. “Four-wave mixing in an optical fiber in the zero-dispersion wavelength region”. In: *Journal of Lightwave Technology* 10.11 (Nov. 1992). Conference Name: Journal of Lightwave Technology, pp. 1553–1561. ISSN: 1558-2213. DOI: 10.1109/50.184893.

[63] F. P. Payne and J. P. R. Lacey. “A theoretical analysis of scattering loss from planar optical waveguides”. In: *Optical and Quantum Electronics* 26.10 (Oct. 1, 1994), pp. 977–986. ISSN: 1572-817X. DOI: 10.1007/BF00708339. URL: https://doi.org/10.1007/BF00708339.

[64] Tetsuya Mizumoto, Roel Baets, and John E. Bowers. “Optical nonreciprocal devices for silicon photonics using wafer-bonded magneto-optical garnet materials”. In: *MRS Bulletin* 43.6 (June 2018). Publisher: Cambridge University Press, pp. 419–424. ISSN: 0883-7694, 1938-1425. DOI: 10.1557/mrs.2018.125. URL: https://www.cambridge.org/core/journals/mrs-bulletin/article/optical-nonreciprocal-devices-for-silicon-photonics-using-waferbonded-magnetooptical-garnet-materials/8B2B2554F12AC31A5052AFD1F6FEB674.

[65] Yuya Shoji and Tetsuya Mizumoto. “Magneto-optical non-reciprocal devices in silicon photonics”. In: *Science and Technology of Advanced Materials* 15.1 (Feb. 1, 2014). Publisher: Taylor & Francis _eprint: https://doi.org/10.1088/1468-6996/15/1/014602, p. 014602. ISSN: 1468-6996. DOI: 10.1088/1468-6996/15/1/014602. URL: https://doi.org/10.1088/1468-6996/15/1/014602.

[66] Rui Ma et al. “Demonstration of an On-Chip TE-Mode Optical Circulator”. In: *IEEE Journal of Quantum Electronics* 59.3 (June 2023), pp. 1–7. ISSN: 0018-9197, 1558-1713. DOI: 10.1109/JQE.2023.3238739. URL: https://ieeexplore.ieee.org/document/10025737/.

[67] Omid Jafari et al. “Mode-conversion-based silicon photonic modulator using asymmetric Bragg grating and Y-branch”. In: *45th European Conference on Optical Communication (ECOC 2019)*. 45th European Conference on Optical Communication (ECOC 2019). Sept. 2019, pp. 1–3. DOI: 10.1049/cp.2019.0767.

[68] Fujin Huang et al. “Circulator-free Thin-film Lithium Niobate Dispersion Compensator Using Chirped Bragg Grating”. In: (2023).

[69] Rulei Xiao et al. “Integrated Bragg Grating Filter With Reflection Light Dropped via Two Mode Conversions”. In: *Journal of Lightwave Technology* 37.9 (May 1, 2019), pp. 1946–1953. ISSN: 0733-8724, 1558-2213. DOI: 10.1109/JLT.2019.2896094. URL: https://ieeexplore.ieee.org/document/8629929/.

[70] Amnon Yariv, Pochi Yeh, and Amnon Yariv. *Photonics: optical electronics in modern communications*. 6th ed. The Oxford series in electrical and computer engineering. OCLC: ocm58648003. New York: Oxford University Press, 2007. 836 pp. ISBN: 978-0-19-517946-0.

[71] Zeqin Lu et al. “Broadband silicon photonic directional coupler using asymmetric-waveguide based phase control”. In: *Optics Express* 23.3 (Feb. 9, 2015), p. 3795. ISSN: 1094-4087. DOI: 10.1364/OE.23.003795. URL: https://opg.optica.org/abstract.cfm?URI=oe-23-3-3795.

[72] *Ansys Lumerical Photonics Simulation & Design Software*. Sept. 27, 2022. URL: https://www.ansys.com/products/photonics/.

[73] Ronald Broeke and Xaveer Leijtens. *Nazca Design*. URL: https://nazca-design.org/.

[74] Dominic F. G. Gallagher and Thomas P. Felici. “Eigenmode expansion methods for simulation of optical propagation in photonics: pros and cons”. In: *Integrated Optics: Devices, Materials, and Technologies VII*. Integrated Optics: Devices, Materials, and Technologies VII.

Vol. 4987. SPIE, June 19, 2003, pp. 69–82. DOI: 10.1117/12.473173. URL: https://www.spiedigitallibrary.org/conference-proceedings-of-spie/4987/0000/Eigenmode-expansion-methods-for-simulation-of-optical-propagation-in-photonics/10.1117/12.473173.full.

[75] Min Qiu. "Analysis of guided modes in photonic crystal fibers using the finite-difference time-domain method". In: *Microwave and Optical Technology Letters* 30.5 (2001). _eprint: https://onlinelibrary.wiley.com/doi/pdf/10.1002/mop.1304, pp. 327–330. ISSN: 1098-2760. DOI: 10.1002/mop.1304. URL: https://onlinelibrary.wiley.com/doi/abs/10.1002/mop.1304.

[76] Alexandre D. Simard, Yves Painchaud, and Sophie LaRochelle. "Integrated Bragg gratings in spiral waveguides". In: *Optics Express* 21.7 (Apr. 8, 2013), p. 8953. ISSN: 1094-4087. DOI: 10.1364/OE.21.008953. URL: https://opg.optica.org/oe/abstract.cfm?uri=oe-21-7-8953.

[77] Lars Emil Gutt et al. "Wavelength Conversion Based on Four-Wave Mixing and Coherency Broken Bragg Gratings". In: *Conference on Lasers and Electro-Optics*. CLEO. Optica Publishing Group, 2022, p. 2. DOI: 10.1364/CLEO_AT.2022.JTh3A.54.

[78] Kyle R. H. Bottrill et al. "Spectral Difference Interferometry for the Characterization of Optical Media". In: *Laser & Photonics Reviews* 13.10 (2019). _eprint: https://onlinelibrary.wiley.com/doi/pdf/10.1002/lpor.201900007, p. 1900007. ISSN: 1863-8899. DOI: 10.1002/lpor.201900007. URL: https://onlinelibrary.wiley.com/doi/abs/10.1002/lpor.201900007.

[79] James Clerk Maxwell. *A Treatise on Electricity and Magnetism*. Vol. 1. Clarendon Press, 1873.

[80] Robert W. Boyd. *Nonlinear Optics*. Second Edition. Academic Press, 2003. ISBN: 978-0-12-121682-5.

As more and more consumers gain access to high-speed internet and as each of these consumers require larger bandwidths, the energy consumption of the internet is rising exponentially. This rise in energy consumption in turn corresponds to the internet being a driver of ever increasing-emissions of greenhouse gases. Passive optical networks (PONs) are an integral part of the physical infrastructure of the internet, where they act as last mile networks. Unfortunately, this type of network is inherently energy inefficient due to how the data signals are divided to the respective receivers in the network. Based on a type of device called an optical time lens, a new type of network called a Lens-PON can be created, which potentially allows for much more efficient transmission of data. At its present stage, Lens-PONs require bulky and inefficient devices constructed using large amounts of optical fiber. Our goal is to integrate the main parts of a Lens-PON on photonic integrated chips, which would massively reduce its size and improve its efficiency to a point where it becomes a viable alternative to traditional PONs. This PhD thesis details the advanced that have been made towards realizing a fully integrated Lens-PON, mainly focusing on methods of lowering the optical losses of the circuit needed for this.

Technical
University of
Denmark

Ørsteds Plads, Bygning 343
2800 Kgs. Lyngby
Tlf. 4525 1700

www.electro.dtu.dk